



HAL
open science

Slabification: Mechanisms controlling subduction development and viscous coupling

Philippe Agard, Cécile Prigent, Mathieu Soret, Benoît Dubacq, Stéphane Guillot, Damien Deldicque

► **To cite this version:**

Philippe Agard, Cécile Prigent, Mathieu Soret, Benoît Dubacq, Stéphane Guillot, et al.. Slabification: Mechanisms controlling subduction development and viscous coupling. *Earth-Science Reviews*, 2020, 208, pp.103259. 10.1016/j.earscirev.2020.103259 . insu-02943055

HAL Id: insu-02943055

<https://insu.hal.science/insu-02943055>

Submitted on 18 Sep 2020

HAL is a multi-disciplinary open access archive for the deposit and dissemination of scientific research documents, whether they are published or not. The documents may come from teaching and research institutions in France or abroad, or from public or private research centers.

L'archive ouverte pluridisciplinaire **HAL**, est destinée au dépôt et à la diffusion de documents scientifiques de niveau recherche, publiés ou non, émanant des établissements d'enseignement et de recherche français ou étrangers, des laboratoires publics ou privés.

Journal Pre-proof

Slabification: Mechanisms controlling subduction development and viscous coupling

P. Agard, C. Prigent, M. Soret, B. Dubacq, S. Guillot, D. Deldicque



PII: S0012-8252(20)30305-6

DOI: <https://doi.org/10.1016/j.earscirev.2020.103259>

Reference: EARTH 103259

To appear in: *Earth-Science Reviews*

Received date: 10 April 2020

Revised date: 21 June 2020

Accepted date: 21 June 2020

Please cite this article as: P. Agard, C. Prigent, M. Soret, et al., Slabification: Mechanisms controlling subduction development and viscous coupling, *Earth-Science Reviews* (2020), <https://doi.org/10.1016/j.earscirev.2020.103259>

This is a PDF file of an article that has undergone enhancements after acceptance, such as the addition of a cover page and metadata, and formatting for readability, but it is not yet the definitive version of record. This version will undergo additional copyediting, typesetting and review before it is published in its final form, but we are providing this version to give early visibility of the article. Please note that, during the production process, errors may be discovered which could affect the content, and all legal disclaimers that apply to the journal pertain.

© 2020 Published by Elsevier.

Slabification: mechanisms controlling subduction development and viscous coupling
Agard P.^{1,*}, Prigent C.^{1,2}, Soret M.¹, Dubacq B.¹, Guillot S.², Deldicque D.³

¹Sorbonne Université, CNRS-INSU, Institut des Sciences de la Terre Paris, ISTeP UMR 7193, F-75005 Paris, France; ²Univ. Grenoble Alpes, Univ. Savoie Mont Blanc, CNRS, IRD, IFSTTAR, ISTERre, 38000 Grenoble, France; ³Laboratoire de Géologie, Ecole Normale Supérieure, UMR CNRS 8538, 24 rue Lhomond, 75005, Paris, France

Keywords: subduction initiation; geodynamics; rheology; viscous coupling; mineral reactions; deformation mechanisms; fluids; plate interface; lithosphere; ophiolite; metamorphic sole.

Highlights:

- metamorphic sole \ banded peridotite pairs constrain plate interface rheology from subduction infancy to mature subduction
- systematic time and space changes in structures, mineralogy, deformation mechanisms and coupling depth
- deep viscous coupling is triggered by suppression of fluids and dissolution-precipitation creep in both nascent and mature subduction zones
- the competition between coupling, and strain localization drives subduction dynamics
- implications for early slab dynamics, coupling and suprasubduction ophiolite genesis

*corresponding author: philippe.agard@sorbonne-universite.fr

Abstract

This contribution investigates mechanisms controlling subduction development and stabilization over time (coined as 'slabitization'), from a nascent slab to a mature slab viscously coupled to mantle convection, from grain scale to plate tectonics scale. Frozen-in, deep and warm portions of the subduction plate interface with both sides still preserved are found at the base of ophiolites in almost pristine state. Both sides record changes in the mineralogy, structure, fluid content and rheology due to devolatilization of subducting metamorphic rocks. They allow characterizing the evolution, shortly after subduction initiation (~1-10 Ma), of interplate coupling, mantle resistance to slab penetration or incipient mantle wedge metasomatism, as well as transformations occurring at depth in warm or cold subduction zones today.

This study combines structural field work, mineralogical and crystallographic data, detailed petrology, thermodynamic modelling and geochemistry from/on both sides of the plate interface, i.e. the base of the mantle wedge (basal ophiolitic peridotites) and crustal fragments from the slab (metamorphic soles). Data collected across the entire Semail ophiolite (Oman, UAE territory) and other similar settings worldwide (e.g., Canada, Turkey, New Caledonia) show a continuous evolution of the subduction plate interface from 1.2-0.9 GPa 900-750°C to 0.7-0.5 GPa 750-600°C, with progressive localization of strain and fluid transfer. Crystallization of neo-formed minerals, enrichment in fluid-mobile elements and their isotopic signature (e.g., for carbon) indicate that metasomatism of the mantle base results from interaction with subduction fluids derived from the dehydrating metamorphic sole and slab tip, migrating at velocities ~1-10 m/a. Coeval deformation and metamorphic reactions in metabasalts of the downgoing slab reveal the importance of mineral changes (e.g., amphibole content) and deformation modes in controlling fluid delivery, stepwise detachment and accretion of successive slices from the downgoing slab (HTa, HTb and then LT soles) to the mylonitized mantle.

This study demonstrates how the interplay between metamorphic reactions, fluid/melt transfer and deformation mechanisms, in particular dissolution-precipitation creep (DPC), controls the mechanical coupling state of the plate interface: (i) suppression of fluid transfer and DPC at depth triggers the onset of viscous coupling. This occurs near ~30 km depth during subduction infancy and HTa sole formation; (ii) with increased cooling and fluid availability, strain localization progressively develops downwards and unzips the subduction interface. The downward migration of viscous coupling triggers localized mantle wedge upwelling, potentially leading to short-lived suprasubduction ophiolite or forearc lithosphere formation; (iii) the locus of viscous coupling stabilizes near ~80-100 km in mature (and cold) subduction zones, and sets mantle counterflow. This is where and when plates get reattached and slabs become part of the mantle convection system.

Recent geochronological data suggest that the duration from subduction nucleation to ophiolite formation is probably slower than suspected (~5-10 Ma), and that another 5-10 Ma may be needed to reach mature subduction and profuse arc magmatism. These results refine our view of the subduction factory and have important implications for how, how much, and which sort of fluid is being fluxed into the mantle wedge at depths where serpentine is no longer stable.

1. From subduction infancy to mature subduction

Mechanisms controlling how subduction initiates and develops over time remain debated (e.g., Regenauer et al., 2001; Stern, 2002; Gerya et al., 2015; Guilmette et al., 2018). Subduction initiation may be viewed as a two-step process: 1) nucleation, triggered by dynamic instabilities at some rheological/geological discontinuity (Casey and Dewey, 1984; Toth and Gurnis, 1998; Stern and Gerya, 2018); 2) infancy, once the incipient slab is progressing down into the mantle (Agard et al., 2016), before it becomes mature and part of the mantle convection ballet (Davies, 1977; Bercovici, 2003).

The successful development of any new intraoceanic subduction zone entails two major requirements (Fig. 1a):

(i) slab penetration, which leads to the differentiation between a lower and an upper tectonic plate and to plate boundary formation (or transformation, if occurring on a preexisting transform fault). In order to become a 'slab', the downflexed oceanic lithosphere needs to overcome the resistance to plate bending, deformation of the lithospheric/asthenospheric mantle (and of the downgoing crust), and buoyancy.

(ii) strain localization, ultimately into a lithospheric scale but thin (< ~km-scale) shear zone or fault, i.e. the plate interface (e.g., Rowe et al., 2013).

During subduction infancy, mechanical and fluid interactions near the tip of the slab (Fig. 1b) can be anticipated to be critical for subduction progress (Agard et al., 2016) and for controlling how, when and where plate tectonics (i.e., the nascent slab) ultimately links up with mantle convection (e.g., Coltice et al., 2019). How this happens in nature, how strain is accommodated, and what role weakening processes and/or fluids may play remain open questions. Whether subduction abortions may take place when these two requirements are not met and be found in the geological record is unknown. Debates exist on whether initiation is spontaneous or forced (Facenna et al., 1999; Stern, 2004; Agard et al., 2007; Guilmette et al., 2018) or on how subduction force balance and mature mantle counterflow develop (Conrad and Lithgow-Bertelloni, 2002; Gurnis et al., 2004; Lallemand et al., 2005; Whattam and Stern, 2011; Billen and Arrendondo, 2018).

Major gaps in knowledge also remain for mature subduction dynamics (Fig. 1c). Despite tremendous progress over the past twenty years (to cite but a few articles across disciplines: e.g., Peacock, 1996; Gerya et al., 2002; Rogers and Dragert, 2003; Abers et al., 2006; Fagereng et al., 2011; Bedford et al., 2013; Deschamps et al., 2013; Shillington et al., 2015; Panet et al., 2018), this is particularly true for (1) mechanical coupling/decoupling processes and (2) geochemical cycling along and across the plate interface:

1. Space and time fluctuations in 'coupling' exist for each subduction zone, either short-term, potentially seismogenic (e.g., Audet et al., 2009; Moreno et al., 2010; Métois et al., 2016) or long-term, related to rock recovery (Monié and Agard, 2009; Agard et al., 2018). Yet the fundamental coupling/decoupling dichotomy of subduction remains poorly constrained:

— mechanical decoupling down to lithospheric depths is needed to enable slab penetration into the mantle (Figs. 1b,c; Zhong and Gurnis, 1995; van Keken et al., 2011) and more generally plate dynamics (i.e., plate interfaces are weak compared to plates; Coltice et al., 2017 and references therein). However, numerical, analog and conceptual models, though increasingly sophisticated, still largely impose slab penetration and strain localization by placing ad hoc weakening mechanisms (i.e. entrained weak material, plastic yielding, strain rate softening or damage mechanisms) at the lithospheric (Gerya et al., 2002, 2015; Yamato et al., 2007a; Sandiford and Moresi, 2019) or convective scale (Zhong and Gurnis, 1995; Bercovici and Ricard, 2012, 2014).

— deeper down, mechanical coupling at the 'common depth of viscous coupling' (CDVC; Wada and Wang, 2009), is needed to explain the existence of a non-convecting 'cold corner' (Fig. 1c; Syracuse et al., 2010; Gao and Wang, 2017), and to physically bridge plate tectonics with mantle convection. However, viscous coupling is for now completely prescribed in thermo-kinematic models (e.g., Wada and Wang, 2009; Arcay, 2017) and inferred to lie at $\sim 80 \pm 30$ km depth as a best fit to forearc low heat fluxes (Wada et al., 2008; Wada and Wang, 2009; Syracuse et al., 2010). While mantle wedge serpentinisation likely contributes to decoupling (Hermann et al., 2000; Hyndmann et al., 2003; Hilairet et al., 2007; Agard et al., 2009, 2016; Reynard, 2013; Guillot et al., 2015), physical mechanisms driving deep (re)coupling are unknown.

Uncertainties on the coupling/decoupling transition prevent a correct understanding of active subduction zones, since this process controls subduction wedge temperature and dynamics (Fig. 1c; Peacock, 1996; Kelemen et al., 2003; England and Wilkins, 2004; Wada et al., 2008), hence mineral reactions, fluid release and element transfer. Furthermore, how this natural system sets up from nascent to mature subduction is unknown.

2. Global geochemical 'budgets' have been estimated based on the release of mineral-bound fluids by metamorphic reactions (Figs. 1d,e; Hacker et al., 2003; Rüpke et al., 2004; Hacker, 2008; van Keken et al., 2011; Kelemen and Manning, 2015), but their exact proportion and fate is unclear. Fluid distribution and migration processes across a subduction plate interface, and their feedbacks onto reactions and deformation, still await sufficient documentation and quantification (e.g., in terms of scale, strain rates, deformation mechanisms; Fagereng and Sibson, 2010; Rowe et al., 2013; Spandler and Pirard, 2013; Agard et al., 2018). This poor knowledge partly stems from the generally poor preservation of mature subduction interfaces: whenever reliably identified, the two sides are tectonically offset by later deformation (Fig. 1d; e.g., Angiboust et al., 2014, 2015; Bonnet et al., 2018). The mantle wedge is rarely returned, and even then peridotites appear very retrogressed (i.e., serpentinized), yielding information on late stages only. Finally, while metamorphic petrology gives precious information on depths (via pressure) and temperature, it does not, alone, constrain the exact location of rocks with respect to the plate interface (Fig. 1d).

Fortunately, relicts of the transient subduction initiation stages do exist, with the two sides of the (frozen-in) plate interface still attached to each other. This is testified by the welding of metamorphic soles, which represent portions stripped from the downgoing slab at ~30 km depth during subduction infancy (Figs. 1b, 2a,b), to banded peridotites lying at the base of ophiolites (e.g., Williams and Smyth, 1973; Dewey, 1976; Searle and Malpas, 1982; Spray, 1984; Jamieson, 1986; Hacker and Mosenfelder, 1996; Gnos, 1998; Wakabayashi and Dilek, 2000, 2003; Searle and Cox, 2002; Agard et al., 2016; Guilmette et al., 2018; Parlak et al., 2019). As shown below, they allow investigating the complex feedbacks between reactions, deformation and fluids at a warm subduction interface. They bear important consequences for mature subduction, since the warm interface migrates downdip as subduction zone matures and forearc cools (Agard et al., 2016, 2018), as well as for suprasubduction zone upwelling and ophiolite formation (Dewey and Casey, 2011; Whattam and Stern, 2011).

Our group has studied these tectonic environments across a variety of locations (Oman, Turkey, New Caledonia; Canada; e.g., respectively, Agard et al., 2016; Plunder et al., 2016; Soret et al., 2016; Dubacq et al., 2019). The present study combines information from both sides of the plate interface, focusing in part on the works of M. Soret and C. Prigent in Oman-UAE (Soret et al., 2017, 2019; Prigent et al., 2018a,b,c). Major results and new findings are used to refine the evolution of this complex system during its first few million years of existence (~1-10 Ma?) as well as our understanding of the subduction 'factory' (Hacker et al., 2003).

We first characterize and compare mineral transformations and deformation mechanisms occurring coevally on both sides of the plate interface (§ 3). We then discuss how they operate to produce coupling or strain localization, from mineral to plate scale (§ 4.1), how they control the evolution of mechanical coupling/decoupling from subduction infancy to mature subduction (§ 4.2), as well as large-scale implications for plate tectonics and mantle convection (§ 4.3).

2. Geological context and geodynamic significance of sole/peridotite pairs

2.1 A frozen-in intraoceanic subduction interface below ophiolites

2.1.1 Structural organization of sole/peridotite pairs

Ophiolites are commonly tens or hundreds of km long, 1-15 km thick fragments of oceanic lithosphere overlying continental lithosphere (Figs. 2,3; Coleman, 1971, 1981; Moores, 1982; Searle and Cox, 1999; Agard et al., 2007; Dilek and Polat, 2008). Their crustal section generally shows the typical succession of the Penrose type ophiolite interpreted as fast-spreading, i.e. rather thick with gabbros, sheeted dykes, basalts and sediments (Fig. 2b; e.g.,

Oman, Turkey, New Caledonia, Papua New Guinea, Bay of Island, Sistan ophiolites; Dilek and Furnes, 2014). In fewer cases it is represented by thinner crust and 'colored mélanges' made of heterogeneously distributed serpentinites, basalts, radiolarites and pelagic limestones (e.g., most Iranian ophiolites: Agard et al., 2011; Moghadam and Stern, 2015; Tibet: Hébert et al., 2012). Due to later erosion, the crustal section may be only partly preserved, and the ophiolite restricted to mantle \pm cross-cutting dykes and plagiogranites (as in the Lycian nappes of Turkey; Celik et al., 2011; Plunder et al., 2016 and references therein).

At the base of the mantle section of large-scale ophiolites worldwide (Coleman, 1981; Wakabayashi and Dilek, 2000, 2003), the mantle commonly exhibits a strong structural anisotropy and in particular pervasive banding ('banded peridotites'; Fig. 2c; e.g., Semail, Bay of Island, Pindos ophiolites: Boudier et al., 1988; Suhr and Cawood, 1993; Jones and Robertson, 1991). Directly below banded peridotites, one finds a ~hundred meter-thick unit made of metamorphosed oceanic crust (Figs. 2c,d) with MORB or E-MORB affinity (more rarely BABB affinity; e.g., Guilmette et al., 2009). This structurally lowermost unit, known as 'metamorphic sole', is dominantly made of metabasalts and metamorphosed pelagic sediments (sheeted dykes or gabbros are rare: Jamieson, 1981; Smart and Wakabayashi, 2009). It is interpreted as a piece of oceanic crust stripped from the downgoing slab and plastered/welded below the ophiolite when subduction is attempting to progress, after its nucleation (Figs. 1b,2a,3; Wakabayashi and Dilek 2000, 2003).

Metamorphic soles invariably show an inverted metamorphism, from granulite (~1 GPa and 800-850°C) to greenschist facies, downwards (~0.5 GPa, 600°C; Williams and Smyth, 1973; Gnos, 1998; Agard et al., 2016 and references therein; Figs. 2d,4). This apparent thermal gradient corresponds to the successive, diachronous stacking of tectonic slices (Jamieson, 1986; Soret et al., 2017; see below). Its significance is not only thermal (i.e. heat transfer by 'ironing': Hacker and Mosenfelder, 1996) but also mechanical (i.e. tectonic coupling; Agard et al., 2016). Near the contact with peridotites, the metamorphic sole is commonly a garnet-bearing amphibolite to granulite facies rock (Fig. 4b,c). The temperature and pressure, though more loosely constrained, experienced by the (usually spinel-bearing) banded peridotites compare well with those of the metamorphic sole, at ~1-0.5 GPa and 900-650°C (Jamieson, 1980; Prigent et al., 2018a). Consistently, banded peridotites share similar deformation patterns (banding, lineation) with the highest metamorphic sole units (Ceuleneer et al 1988; Fig. 2c), pointing to close genetic processes. Banded peridotites and metamorphic soles are therefore crucial witnesses of how subduction processes develop through mineral reactions, deformation and fluid migration along and across the nascent subduction interface.

2.1.2 Ophiolite types and subduction initiation

All pieces of evidence converge to oceanic origin for the banded peridotites and soles, and argue for their initial juxtaposition during the early stages of intraoceanic subduction (Figs. 1a,b,2a). Based on their relationship to continental lithosphere, two major types of ophiolites and soles were recognized (Wakabayashi and Dilek, 2003; Fig. 3a): Tethyan ophiolites emplaced, after intraoceanic subduction, by subsequent underthrusting of a continental margin; Cordilleran ophiolites accreted to the subduction forearc, be it continental (e.g., Western USA) or oceanic (e.g., Philippines sea plate for the Izu-Bonin, which may ultimately turn into an ophiolite; Stern et al., 2012). Tethyan examples include Oman or Turkey, while Cordilleran examples can be found in California or the Himalayas. Regardless of the initial setting, ophiolite emplacement onto the continental margin (i.e., obduction in a strict sense; Fig. 2b) always requires a first stage of intraoceanic subduction and then either short-lived continental subduction or only underthrusting below the future ophiolite (Wakabayashi and Dilek, 2003; Vaughan and Scarrow 2003, Agard et al 2007, 2014; Dewey and Casey, 2013; Jolivet et al., 2016; van Hinsbergen et al., 2015).

The detailed petrogenesis of ophiolites is beyond the scope of the present contribution. They show a large variability (Dilek and Furnes, 2014), from inverted MORB-type basins (Nicolas, 1989; Benoît et al., 1999; Hassig et al., 2016) to entirely suprasubduction lithosphere (Pearce et al., 1981; McLeod et al., 2013; Whattam and Stern, 2011). Around the world, however, most large-scale obducted ophiolites seem to bear some supra-subduction imprint to various degrees (Shervais, 2001; Dilek et al., 2007; Ishizuka et al., 2014).

Uncertainties remain as to the locus of subduction nucleation (i.e., dashed vertical line in Fig. 3a): at a transform fault (Hacker et al., 1996; Whattam and Stern, 2011; Zhou et al., 2018; van Hinsbergen et al., 2019), at a ridge (Nicolas and Le Pichon, 1980; Nicolas et al., 2000), in a back-arc basin (Guilmette et al., 2009, 2012) or a former oceanic detachment (Maffione et al., 2015; van Hinsbergen et al., 2015). Whether subduction is induced or spontaneous probably depends on the exact geodynamic configuration, and is a matter of debate (Fig. 3a; Stern et al., 2004; Guilmette et al., 2018). In the case of the Semail ophiolite (and others around Arabia, from Turkey to Oman; Ricou, 1971), intraoceanic subduction is most likely induced since it follows a major plate reorganization at 110 ± 5 Ma (Agard et al., 2007; Matthews et al., 2012).

Two end-member scenarios exist for the timing of subduction initiation with respect to ophiolite formation (Fig. 3b): either subduction initiates and triggers the formation of the ophiolite lithosphere by mantle upwelling (case A; e.g., Guilmette et al., 2018); or subduction initiates near a preexisting but buoyant, young or rejuvenated ophiolite lithosphere guiding strain localization (case B; Hassig et al., 2016).

Spray (1984) noted that most ophiolites and associated soles seem to form within less than 10 Ma. In the case of the Semail ophiolite, the age of magmatic rocks (95.5 ± 1 Ma) is to a first approximation similar to most age constraints for the HT metamorphism of the sole

(~96.5-94 Ma; Hacker, 1994; Rioux et al., 2016 and references therein), advocating for their cogenetic relationship (case A; Fig. 3b). The older ages obtained for the prograde path of Semail metamorphic soles using HT radiochronometers (~104-103 Ma; Guilmette et al., 2018) further support case A (rather than case B as first imagined by Nicolas and Le Pichon, 1980). This time lag between subduction initiation and (supra-subduction) ophiolite formation strengthens the view that intraoceanic subduction was induced in the Neotethys (Agard et al., 2007, 2014), and suggests that the first stages of subduction nucleation/infancy may last on the order of 5-10 Ma.

2.2 A specific snapshot in subduction history

As recalled in the introduction, the example of banded peridotites overlying metamorphic soles is the only one for which the two sides of the (frozen-in) plate interface are still attached to each other and not significantly offset by later tectonics.

The distribution of specific lithologies, P-T estimates and structural position shows that the formation of metamorphic soles too is non-random (Fig. 2d; Spray, 1984; Dewey and Casey, 2013; Agard et al., 2016): dominantly mafic sections always lie on top of metasedimentary (or mixed mafic-sedimentary) soles, and exhibit both higher T and P conditions (Fig. 4). This organization was refined by Soret et al. (2017, 2019; Fig. 5a).

At the base of the Semail ophiolite, Soret et al. (2017) identified three subunits, referred to as HTa, HTb then LT (Figs. 4a-g), the latter being essentially metasedimentary. Pressure and temperature conditions for the garnet, clinopyroxene, amphibole, plagioclase (Grt-Cpx-Amph-Plag) bearing HTa unit cluster around 850°C, 1.0-1.1 GPa (Fig. 5a; see also Gnos, 1998; Cowan et al., 2014; Agard et al., 2016). P-T conditions for the still dominantly mafic HTb are slightly lower, at 750°C, 0.8 GPa. The HTa and HTb sub-units are discontinuously separated by 5-50 cm thick garnet-bearing metasedimentary horizons. In contrast, the metasedimentary, dominantly metasiliceous LT unit shows greenschist to low-grade amphibolite facies, with quartz, white mica, chlorite ± biotite (± amph, plag) indicative of P-T conditions around 600°C and 0.5 GPa.

Banded unit peridotites have been affected by an intense mylonitic deformation (Figs. 4h-j; Ceuleneer et al., 1988; Prigent et al., 2018a). Lenses of peridotites with porphyroclastic textures and a distinct foliation orientation ('the protoliths' of mylonites) have been preserved in some massifs (Fig. 4j). The orientation of mylonitic shear zones is parallel to the foliation of metamorphic soles, advocating for their coeval deformation (Figs. 2c, 4b). Thermometric estimates indicate that deformation occurred under peridotite cooling and led to the formation of (proto)mylonitic (at ~850-750°C) then ultramylonitic (at ~750-650°C) shear zones (Fig. 5a;

Prigent et al., 2018a). Below 650°C, serpentinisation of banded peridotites was minor, in mesh texture or in shear zones cross-cutting mylonitic deformation features.

The base of the Semail ophiolite provides a snapshot on the P-T/subduction-welding-exhumation history during three main accretion stages (Fig. 5b):

(1a) HTa is welded to and jointly deformed with the mantle base. The >500-1000m thick zone of deformation in the banded peridotites (Ceuleneer et al., 1988) advocates for km-scale, distributed deformation at this stage (Fig. 2c; i.e., T_H unit on 1/250,000 scale maps of Buraymi, Sur or Nazwa); (1b) HTa and mantle peridotites are exhumed together and juxtaposed to HTb at shallower depths; (2) the exhuming HT soles and mantle are then underthrust by LT metasediments at ~0.5 GPa; the presence of only sediments, and lack of imbricated mafic crust at that stage, indicate a drastic reduction in plate interface thickness (Agard et al., 2018); (3) during ~5-15 Ma, i.e. between accretion of LT soles at ~95-93 Ma (Hacker, 1994) and peak burial of high pressure cover unit from the continental margin at 85-80 Ma (Warren et al., 2005; Warren et al., 2011), no accretion takes place along the subduction interface, advocating for efficient strain localization along a lubricated plate boundary shear zone.

The sole/peridotite pair therefore brings essential information on the progressive deformation, along and across the slab/mantle interface, of a nascent subduction undergoing cooling (Fig. 5b; see also § 2.3). It allows tracking strain localization through time, consistent with the development of a plate boundary shear zone, and provides an idea of the thickness/width of the subduction zone interface. Major questions include how these units are jointly deformed, how fluids are expelled, and where they are transferred during welding of the units.

Several important features of this well-preserved geological set-up need to be underlined (Fig. 6): (i) while the juxtaposition of HTa to the (proto)mylonitic peridotites (Prigent et al., 2018a) represents a genuine snapshot of what is happening at the exact subduction plate interface, their later deformation and early exhumation takes place somewhere along the interface and this overprint (e.g., mylonitic to ultramylonitic structures in banded peridotites; Prigent et al., 2018a; see below) must be disentangled from features formed at peak burial; early exhumation of HTa resulted in particular in the strong thinning of this unit, by a factor of 5-10 (as discussed in Soret et al., 2017, 2019); (ii) the peak metamorphic conditions experienced by HTb, and its accretion to the HTa-banded peridotite pair, represent another snapshot in time to study the mechanical behaviour at the plate interface; (iii) mineral transformations and deformation mechanisms witnessed by HTb may inform on the prograde evolution of HTa prior to its accretion, largely erased since.

2.3 Geodynamic significance: plate interface mechanical coupling

The welding of metamorphic soles to the mantle reveals pervasive joint deformation of the lower and upper plates shortly after subduction initiation (Figs. 2a,7a). This testifies to strong interplate mechanical coupling, which in turn implies similar effective viscosities (rheologies) on each side, at least transiently. The qualitative evolution of crustal and mantle resistance is illustrated in figure 7a.

Metamorphic sole accretion can be viewed as the transient period during which the newborn slab faces resistance of the upper plate mantle acting as a buttress (Agard et al., 2016; Soret et al., 2019; Figs. 1a,b). The comparison of experimental flow laws (Fig. 7b) shows that the slab crust is expected to be stronger than the (shallow) serpentinized mantle wedge until a given depth, where it reaches an effective viscosity similar to that of the deeper and drier mantle wedge (evolution 1 to 1"; Figs. 7a,b). Bulk viscosities inferred at the intersection, around 10^{20-21} Pa.s, match values used independently by numerical models (Regenauer-Lieb et al., 2001; Coltice et al., 2017 and references therein).

As (and if) the mantle wedge progressively cools, its fluid storage capacity increases and the domain where serpentine is stable (<600-650°C; Fig. 7a) expands downward. This lubricates and unzips the subduction interface at least until depths where the contrast in viscosity between both sides of the plate interface remains large enough. Strong mechanical coupling is therefore shifted downwards (Agard et al., 2016). Estimates suggest that coupling in mature subduction zones occurs near 80-100 km depth (i.e. CDVC; Wada and Wang, 2009; Syracuse et al., 2010; Arcay et al., 2017) and that temperatures transition between ~550 and 800°C across a few km only (Fig. 1c; England and Wilkins, 2004; Abers et al., 2017).

The evolution of mechanical coupling with time therefore highlights the key importance of the nature of incoming materials, fluid release and hydration of mantle wedge peridotites.

Which deformation mechanisms physically govern the convergence of mantle and crust viscosities at mineral scale and over which distances they remain similar, is however unknown. This evolution in both strain localization and slab penetration is such an intricate yet generic geodynamic process, as recalled in introduction, that deformation must be studied down to the grain scale (Bercovici et al., 2012; Bercovici and Ricard, 2014; Agard et al., 2016; Billen and Arredondo, 2018; Prigent et al., 2018c; Soret et al. 2019).

3. Progressive evolution of deformation, reactions, and fluids along the plate interface in mafic and ultramafic rocks

3.1 Mineralogical evolution in metamorphic soles and banded peridotites

3.1.1 Metamorphic sole

Pressure-temperature paths for HTa, HTb and LT summarize the evolution of the metamorphic sole (Fig 8a; see Soret et al., 2017 for details). In order to address the pristine stages of mechanical coupling responsible for km-scale distribution of deformation across the subduction interface shear zone (§ 2.3), only the evolution of mafic protoliths is tracked here (i.e., HTa and HTb; Fig. 8).

Emphasis is placed on HTa, which represents the first and deepest/hottest body of rocks accreted and exhumed during incipient subduction: past the coupling point, by definition, any potential rock witness is subducted (Figs. 1,6b). HTa shows upper amphibolite to granulite facies conditions, while HTb only reached upper amphibolite conditions (Fig. 8a). HTa shows evidence of retrogression into the conditions of HTb. This retrogression can be tracked through the decreasing Ti content of amphibole (Fig. 8b) in shear bands, pressure shadows or fractures, and by thermodynamic modelling (Fig. 8c; Soret et al., 2017, 2019).

— HTa is composed of variably preserved garnet-clinopyroxene bearing amphibolites. The highest T foliation (termed peak HTa for the sake of clarity) comprises an association of intergrown garnet and clinopyroxene (Fig. 8d,g), together with minor plagioclase and amphibole. Garnet and/or clinopyroxene can be porphyroblastic (Fig. 8d). Garnet commonly contains rounded, amoeboidal clinopyroxene inclusions, together with titanite and/or rutile. This assemblage is commonly overprinted by fine-grained aggregates of brown amphibole and plagioclase ± clinopyroxene (Fig. 8e). In all samples, plagioclase is pervasively altered so that changes in plagioclase composition are difficult to track. Samples are also cut across by late veins of epidote ± prehnite ± albite (Fig. 8e).

Close to the contact with banded peridotites (< 20m), plagioclase-rich amphibolites coexist with relicts of granulite facies garnet-clinopyroxene-rich ones that exhibit small grain sizes (<300 µm, but for rare mm-scale garnet porphyroblasts) and, in places, a mylonitic foliation (Fig. 8e). Peak P-T conditions are estimated at 850°C, 1-1.1 GPa (Fig. 8c). This HTa unit exhibits only local and limited melting (Fig. 4d; Searle and Malpas, 1982), mostly as cm-scale plagioclase-rich trondjemitic veinlets (± quartz, amphibole; Gnos, 1998; Warren et al., 2005). There is no sign of melt extraction, consistent with the ~5% melting maximum inferred for the peak of HTa from thermodynamic modelling (Fig. 8c; Soret et al., 2017). In line with this macroscopic observation, extremely rare melt inclusions are found in HTa garnet (Guilmette et al., 2018), whereas some exist in garnet from the metasedimentary veneer between HTa and HTb. How much amphibole and plagioclase coexist with garnet and clinopyroxene at peak conditions (particularly in the peak HTa foliation), depends on changes in bulk chemistry and hydration (for 1wt% H₂O, ~ 20 vol% each at 850°C, and ~10 vol% at 900°C for a MORB-type composition; for 0.4 wt% H₂O, amphibole modal amounts drop to <10 vol%).

— HTb is dominantly composed of amphibole and plagioclase aligned in the foliation, with or without clinopyroxene (Fig. 8f), and more rarely garnet or epidote. Biotite is found in places as <mm-thick coatings on the foliation. There is no evidence of large-scale melting in the mafic protolith in Oman-UAE. In contrast, several granitic bodies cutting across the Semail ophiolite have been assigned to melting of slab sediments (Rollinson, 2015; Haase et al., 2015; Spencer et al., 2017), consistent with temperatures of HT soles above the solidus of pelitic metasediments (>700-750°C).

3.1.2 Banded peridotites

The mineralogy of the banded peridotites reveals progressive deformation and cooling of the mantle (Fig. 9). The 'protoliths', i.e. porphyroclastic peridotites deformed at ~1200°C, are transformed to protomylonites, mylonites and locally ultramylonites (Fig. 9a-c; Linckens et al., 2011; Ambrose et al., 2018; Prigent et al., 2018a).

Banded peridotites are spinel-bearing lherzolites or Cpx-harzburgites dominated by olivine, orthopyroxene and variable modal amounts of clinopyroxene (Takazawa et al., 2003; Khedr et al., 2013; Yoshikawa et al., 2015; Prigent et al., 2018a). Grain size decreases for all minerals with increasing deformation and nearer to the contact (Fig. 9f). Decimeter to meter-thick horizons of dunite are also widespread: their alternation with lherzolite/Cpx-harzburgite horizons results in the conspicuous m- to km-scale banding (Fig. 2c).

Several systematic observations may be outlined (see Prigent et al., 2018a,b for details): (i) commonly dissected orthopyroxene porphyroclasts (Fig. 9a) and dissolved primary minerals (Fig. 9e); (ii) secondary, fine-grained (~100-200 µm) polymineralic domains (Figs. 9b-e); (iii) small amphibole (a magnesian-hornblende to pargasite) in deformed areas (Fig. 9d); (iv) absence of chlorite or serpentine as part of the deformed zones. Serpentinisation is indeed irregularly distributed, making up to ~15 vol %, and is less extensive in more ductilely deformed samples (i.e. mylonites and ultramylonites).

The more strongly deformed rocks show more abundant polymineralic domains. These domains contain both recrystallized and neofomed grains with mineral nature and compositions differing from those of the primary Ol-Opx-Cpx-Spl assemblage (Fig. 9e,g; as an example, unlike for porphyroclasts, secondary Opx shows no Cpx exsolution). In mylonite shear zones, magnesian-hornblende to pargasitic amphibole appears in equilibrium with these secondary minerals, whereas amphibole replaces them in porphyroclastic peridotites. This supports interaction of banded peridotites with fluids during their mylonitic deformation. Modal amounts of amphibole increase with increasing intensity of mylonitization (Fig. 9h), consistent with increasing addition of water (i.e., fluid ingression) during deformation and cooling. Thermodynamic modelling using bulk rock compositions suggests that the amphibole content of some mylonites and ultramylonites corresponds to that predicted with water-saturated conditions (Prigent et al., 2018a).

The composition of amphibole and coexisting pyroxenes in major and trace elements indicates that formation of protomylonites to mylonites occurred across a temperature range from 900-850 to 750°C (Prigent et al., 2018a), while transformations affecting ultramylonites reflect temperatures in the range 750-650°C.

3.2 Deformation mechanisms at ~850°C (peak burial of HTa, coupling and detachment)

3.2.1 Metamorphic sole

Granulite facies domains preserved in HTa (i.e. peak HTa; or stage A1 in Soret et al., 2019) are composed of two-phase Grt-Cpx mixtures, with minor and variable amounts of amphibole and/or plagioclase. They show approximately equal volume proportions of garnet and clinopyroxene (Fig. 10a). The best-preserved domains show an evolution from an equigranular texture to strain localization (e.g., shear band formation; Fig. 8e) accompanied by grain size reduction as a result of brittle fracturing (Fig. 8e, 10b).

Clinopyroxene is statistically oriented along the [001] axis and contributes to a weak shape-preferred orientation (SPO). Grain size is commonly on the order of 500 µm, as attested by relictual Cpx porphyroblasts. Minor undulose extinction is visible in the larger grains.

EBSD data shows that clinopyroxene deforms only partly by dislocation creep along the preferential (100)[001] slip system (SM1). Garnet, in contrast, shows no hint of intracrystalline deformation other than fracturing. The highest T amphibole, aligned parallel to Cpx and probably stable with Grt and Cpx (and contributing to the SPO), also evidences fracturing. The composition of Ti-rich amphibole found in fracture filling pleads for the existence of brittle deformation already at ~800°C (Figs. 10b,c,d). Fracturing nevertheless continues during cooling as shown by low T infilling minerals (Soret et al., 2019).

Fracturing is visible in clinopyroxene too. The presence of some garnet ribbons indicates that garnet is somewhat stronger than clinopyroxene.

3.2.2 Banded peridotites

A marked decrease in grain size is evidenced in (proto)mylonites deformed at ~900-750°C, with grains <200 µm on average (Fig. 9f). Noteworthy, grain size reduction is not associated with an increase in minor phase proportion, so that initial olivine grain size reduction (hence peridotite weakening) does not directly result from initial differences in minor phase abundance.

Large, mm-size pyroxene and olivine porphyroclasts deform by dislocation creep, as shown by the presence of undulose extinction, subgrains and triple junctions between grains (e.g., Mehl et al., 2003; Michibayashi et al., 2009; Prigent et al., 2018c). However, the very

irregular shape of porphyroclast grain boundaries and the polymineralic nature of embaying, amphibole-bearing fine-grained zones can hardly be explained by dynamic recrystallization of porphyroclasts only.

These observations indicate instead a contribution of dissolution-precipitation processes induced by fluid-peridotite interaction. Coarse-grained orthopyroxene also show episodic fracturing with mineral infills similar in nature and composition to grains located in deformed areas (Fig. 10e). In fine-grained zones, dislocation creep dominates in olivine, and to a lesser extent in orthopyroxene and clinopyroxene (SM1). Olivine CPO geometry and movement of its intracrystalline low angle misorientations is consistent with the dominant activation of the (010)[100] and (001)[100] slip systems (Prigent et al., 2018c). Activation of olivine (001)[100] dislocation slip systems in (proto)mylonitic shear bands advocates for its deformation under hydrous conditions (e.g., Jung et al., 2006; Cao et al., 2015; Precigout et al., 2017).

3.3 Deformation mechanisms at ~750°C (peak burial of HTb, early exhumation for HTa-peridotite pair)

These deformation features develop during peak burial of HTb, when the pair of banded peridotites and HTa metamorphic sole is partly exhuming and cooling. This is when mantle (proto)mylonitic shear zones are fully developed and ultramylonites formation starts (Fig. 5). Accretion of HTb to the partly retrogressed HTa - banded peridotite pair indicates that their mechanical behavior is close. Deformation of HTb is therefore used to (i) document deformation mechanisms along the interface and (ii) as a proxy for deformation during progressive burial of HTa. Complementary information can be gained from deformation mechanisms observed in the peridotites and HTa at this temperature: they are responsible for the accommodation of a huge amount of strain and thinning (with $\gamma \geq 5-10$; Soret et al., 2019). Overall, this temperature range is marked by the presence of fluid-rock interactions in all lithologies causing the prominent activation of grain-size sensitive deformation mechanisms (see SM1, SM2).

3.3.1 Metamorphic sole: HTb and retrogressed HTa

— in HTb:

HTb most commonly shows roughly equivalent volume proportions of Amp and Plag (\pm Cpx \pm Grt, yet never reported together). In general there is extensive grain mixing and layering of either Amp or Plag is moderate at most (Fig. 11a), hinting to a rather weak rheological contrast between both minerals (see Seyler et al., 2015; Marti et al., 2017, 2018) and/or to the dominant role of phase mixing through nucleation (Precigout and Stunitz, 2016) or the grain-size sensitive (GSS) process of grain boundary sliding (Linckens et al., 2014).

A few almost monomineralic macroscopic (1-2 cm-thick) horizons of amphibole or plagioclase are nevertheless found in the middle of the HTb unit (Fig. 4h), but the boudinage of either amphibole in plagioclase or plagioclase in amphibole again supports a weak rheological contrast between the two phases.

Amphibole shows a relatively strong CPO (J index; SM1) produced by recrystallization overgrowths selectively oriented along (001). This feature points to (oriented) pressure-solution and activation of dissolution-precipitation creep (DPC) rather than dislocation creep (DC; SM1), consistent with the abundance of fluid inclusions.

Similarly, there is no evidence for any significant dislocation creep in plagioclase (see SM1). Some grain boundary migration is visible in plagioclase, however, hinting to some secondary grain growth and mineral recovery. Brittle fracturing of amphibole (and plagioclase) is observed, but less conspicuous than in peak HTa.

Whenever clinopyroxene is present and in equilibrium with amphibole and plagioclase, it shows no evidence of deformation by dislocation creep, but instead through oriented growth.

— In retrogressed granulite domains of HTa (stage A2 of Soret et al., 2019):

This deformation stage is marked by extensive dissolution of garnet and clinopyroxene in retrogressed HTa (as attested by irregular grain boundaries and embayment of finer grains; see also Cowan et al., 2014), both of which show boudinage along former fractures (Fig. 11b). Recrystallization of clinopyroxene is commonly observed, as well as reequilibration of clinopyroxene compositions on grain edges (Figs. 8h,i). No evidence of dislocation creep is observed, however, in the newly formed much finer grained clinopyroxene crystals.

Oriented growth of intermediate to low Ti-content amphibole dominates, and contributes to the observed CPO (as for HTb). Passive rotation and alignment of amphibole contributes to the overall SPO. Both processes accommodate an important fraction of deformation (Soret et al., 2019). Fracturing of amphibole is also common. As deformation progresses, the crystallization of successively lower T amphibole, and of different plagioclase composition (though rarely well-preserved), is observed.

This deformation stage results in an important grain size reduction in HTa, with fine scale aggregates of amphibole and plagioclase always smaller than in HTb (~100 μm versus ~300-400 μm). Dissolution-precipitation creep, phase mixing and grain boundary sliding, i.e. GSS processes, appear to be the dominant deformation mechanisms during this deformation event at ~750°C. The marked increase in amphibole content compared to the drier Grt-Cpx assemblage attests to the ingress of fluids during cooling. The presence of C'-type shear bands advocate for a component of simple shear (only rarely observed in peak HTa).

3.3.2 Banded peridotites

Mylonites and ultramylonites reveal further grain size reduction (Figs. 11c,d) and the randomization of olivine CPO (Prigent et al., 2018b). The observed correlation between the

decrease in olivine CPO strength and grain size indicates a decreasing contribution of dislocation creep to olivine deformation during shearing (see also Ambrose et al., 2018).

Nucleation of new grains and phase mixing is ubiquitous (Fig. 11c). Nucleation-induced phase mixing is visible through the irregular grain boundaries, embayment of finer grains around former porphyroclast and olivine matrix grains, precipitation of new mineral grains (among which amphibole) and subsequent growth at the expense of matrix minerals. This process induces grain boundary pinning, as shown by the Zener pinning grain size distribution (Prigent et al., 2018c), which prevents grain growth and textural recovery (Herwegh et al., 2011).

In contrast to olivine, the (weak) CPO strength of the small pyroxene grains is not randomized during ongoing deformation. Pyroxene CPO geometry is also incompatible with any known dislocation slip system, so that its CPO rather results from continuous syntectonic oriented precipitation and growth during deformation (Dijkstra et al., 2002; Hidas et al., 2016) than from the movement of intracrystalline dislocations.

Amphibole content reaches up to ~3 vol% in (ultra)mylonites, consistent with H₂O saturation (Prigent et al., 2018a; Fig. 9h). The crystallization of amphibole in equilibrium with other phases in the finer-grained polymineralic zones testifies to the presence of hydrous fluids during deformation and activation of dissolution-precipitation.

3.4 Tracking element transfer and fluid/melt fluxes

While pressure conditions are best constrained by thermodynamic modelling of amphibolites/granulites (Fig. 8), fluid migration is best tracked in banded peridotites (Fig. 9).

A significant enrichment in fluid-mobile elements and large lithophile elements (FME, LILE) with respect to the depleted MORB mantle (DMM) is observed for olivine, pyroxenes (Fig. 12a) and amphibole, notably B, Li, Cs, with concentrations up to 400 times those of the DMM (Prigent et al., 2018a). Olivine is also enriched in Pb and Sr compared to DMM olivine. Mineral concentrations in FME match those measured in mantle wedge serpentines (Deschamps et al., 2013; Prigent et al., 2018b). B concentrations in those minerals range between 0.1 and 30 µg/g, whereas whole rock B concentrations vary from 5 and 100 µg/g for both banded peridotites and metamorphic soles, suggesting an enrichment of peridotites in B during later serpentinisation (Prigent et al., 2018b).

Refertilization through fluids during peridotite mylonitization is further highlighted by boron isotopic analyses (¹¹B being preferentially mobilized in fluids relative to ¹⁰B; Marschall et al., 2018 and references therein). Grain size and fabric strength reduction from porphyroclastic tectonites to protomylonites and (ultra)mylonites are indeed associated with a progressive increase in sample δ¹¹B values (Figs. 12b,c) up to +25%. δ¹¹B decreases steadily away

from the contact to DMM values within ~400m (Fig. 12b), along with the decrease in the amount of amphibole (Fig. 12c). Banded peridotites have a $\delta^{11}\text{B}$ values closer to arc lavas (up to 50 $\mu\text{g/g}$ and +18‰) than to the DMM (0.08 and ~7‰, respectively). The highest grade HTa samples located within ~10 m from the banded peridotites, with granulite relicts, also have relatively high $\delta^{11}\text{B}$ values, between 6 and 11‰ (Prigent et al., 2018b).

These observations advocate for extensive metasomatism at the base of the mantle section. The metasomatizing agents for transformations <900°C are more likely enriched aqueous fluids than melts, as shown by the high FME/HFSE and FME/LREE ratios in primary minerals, the high $\delta^{11}\text{B}$ values of peridotites and the qualitative correlation with amphibole concentrations. These fluids likely derive from the subduction-related dehydration of the metamorphic sole (Prigent et al., 2018b), as further shown by the comparison of respective depletions/enrichments with respect to their low-grade equivalents (Ishikawa et al., 2005; see also Bebout et al., 1999 for warm subduction). The decrease in peridotite $\delta^{11}\text{B}$ with increasing distance to the contact (Figs. 12b,c) highlights its progressive modification of fluid composition, and loss of its initial high- $\delta^{11}\text{B}$ subduction signature, within the first km above the plate interface due to fluid-peridotite interaction.

HTa amphibolites located close to the contact (Ishikawa et al., 2005; Soret et al., 2017) show significant enrichments in FME (B, Li) and HLE (Rb, K, Ba) and enrichments of LREE over HREE (Ishikawa et al., 2005). Further away from the contact (>~50-80 m, i.e. equivalent to HTb samples) the metamorphic sole shows again the same type of enrichments with respect to MORB, but much less pronounced and lacks peaks in B and Li.

These results, though based on a limited number of amphibolite samples, indicate that peaks in B and Li observed in HTa and the banded peridotites may result from the dehydration of the slab tip and/or underthrust units such as HTb (including some minor sedimentary fraction; Soret et al., 2017). The increase in modal amounts of amphibole in HTa also requires the input of fluids liberated from downgoing (and possibly underplated) material, at P-T conditions equivalent to those of HTb. The presence of interstitial hydrous fluids likely enhanced mass transfer at grain boundaries and therefore dissolution/precipitation processes and grain size reduction during ongoing shearing.

Reactive transport diffusion modelling of upward reactive percolation of B through the (banded) peridotites (Bickle and McKenzie, 1987; De Paolo, 2006; assuming steady state dissolution/precipitation and neglecting B transport by diffusion compared to fluid advection), indicates fluid migration velocities on the order of 1-10 m/a at 900-750°C (for a fluid/peridotite ratio of 0.01 and an average dissolution rate for orthopyroxene: Fig. 12d; see Prigent et al., 2018b for details). Models satisfactorily reproduce the increase of $\delta^{11}\text{B}$ in the rock close to the contact and its gradual decrease away to near DMM values.

Further conclusions can be drawn from the spatial distribution of $\delta^{11}\text{B}$ patterns in banded peridotites: (i) in the first 50 m of the contact, the similarity in $\delta^{11}\text{B}$ of the protomylonites and

the ultramylonites (formed during retrogression and exhumation at temperatures ~750–650°C) suggests that some peridotites reached saturation, their isotopic composition remaining to a first approximation unchanged after further interaction with fluids; (ii) further upsection, the higher $\delta^{11}\text{B}$ values of ultramylonitic shear bands compared to protomylonites suggests that fluids became increasingly channelized with increasing deformation and strain localization; (iii) $\delta^{11}\text{B}$ close to the DMM in HT peridotites and some porphyroclastic tectonites implies that porous fluid flow was not pervasive but localized in active shear zones running parallel to the plate interface during the proto- to ultramylonitic deformation of the basal mantle. Noteworthy, later serpentinisation below 650°C increased the whole rock B concentration but did not impact $\delta^{11}\text{B}$ significantly (Prigent et al., 2018b).

3.5 Complementary observations from other examples worldwide

This section evaluates similarities and differences with other sole/peridotite pairs in comparable settings worldwide. So far, however, systematic documentation of both sides of the plate interface is only available for the Semail example (this study). Ophiolite localities with well-preserved sole/peridotite pairs are found in the Appalachians (e.g., Variscan ophiolites from north-east Canada; Bay of Islands and White Hills, Newfoundland; Mt Albert, Québec), Balkans and Greece (e.g., Mirdita, Pindos, Evia), California (Josephine, Feather River), Turkey (Lycian, Pozanti, Beysahir), Iran (Neyriz, Nain-Baft, Sistan) or the SW Pacific (e.g., N. Caledonia). Much less information exists worldwide on banded peridotites compared to soles, probably because of the lack of diagnostic 'metamorphic' minerals and difficult thermobarometry in peridotites (and/or emphasis on petrological processes within the ophiolite; e.g., Kelemen et al., 1995; Boudier et al., 1996; Le Mée et al., 2004). The interested reader may use the recent worldwide compilation of peak P-T conditions for HT and LT metamorphic soles as a guide to these locations (Agard et al., 2016; their Table 1 and figure 2a).

3.5.1 Mineralogy and P-T conditions for HT metamorphic sole and peridotite pairs

— Metamorphic soles:

They exhibit strong flattening, intense deformation and evidence for composite stacking of distinct slices (Jamieson and Strong, 1981). They commonly lack a well-defined lineation, however, despite some exceptions (see below; Suhr and Cawood, 1993). Peak P-T conditions for HT sole are on average $800 \pm 50^\circ\text{C}$ and 1 ± 0.2 GPa. Pressure-temperature estimates can probably be refined, as disparate methods have been used since the 1980s, but all metamorphic soles show an apparent inverted metamorphism, recognized for long (William and Smith, 1973; Malpas, 1979; Spray, 1984). They also show the same systematic

trends in mineralogy as for the Oman-UAE example. HT soles are characterized by Grt-Cpx±Amph±Plag-bearing soles near the contact with the mantle (e.g., MacGregor and Basu, 1979), with garnet-rich granulite facies amphibolites and banded Cpx-bearing amphibolites only found in the vicinity of the contact (Williams and Smyth, 1973; Savic, 1988). These overlie Amph-Plag±Ep-bearing soles, probably equivalent to HTb. LT soles consist of micaceous quartz-rich metasediments, locally kyanite-bearing, together with scarier carbonate horizons and Amph-Ep-Ab±Plag-bearing metabasalts. Metamorphic soles group along a typical gradient of $\sim 25 \pm 5^\circ\text{C}/\text{km}$ (Agard et al., 2016).

In Mt Albert, Grt-Cpx-bearing (HTa) metamorphic soles better preserve peak assemblages than in Semail (O'Beirne-Ryan et al 1990; Dubacq et al., 2019). Their texture resembles that of figure 8d (see also Guilmette et al., 2008 or Plunder et al., 2016, for similar textures from Tibet or Turkey). They show characteristic garnet-clinopyroxene intergrowths (i.e., symplectites; Fig. 13a-c) associated with hydrous minerals (HT epidote) that are consistent with the presence of melts in the mafic rocks. Locally, the presence of leucosomes, anorthite and nanogranites (Fig. 13d; Dubacq et al., 2019) attests to the melting of a subordinate fraction of sillimanite-bearing metasediments in HTa. In comparison, leucosomes and nanogranites are only found between HTa and HTb in the Semail example. Felsic, plagioclase-rich veinlets or cm- to m-scale pods are nevertheless found in most metamorphic soles (e.g., Guilmette et al., 2008). These 'plagiogranites' resemble but should not be confused with plagiogranites that represent strongly differentiated melts belonging to the ophiolite crustal section (Oman-UAE: Tilton, 1981; Rioux et al., 2012, 2013; Turkey: Parlak et al., 2019).

Despite later subduction cooling, as manifested by blueschists and eclogites in the underthrust continental rocks (Fig. 2b), metamorphic soles commonly lack a HP-LT overprint: this indicates exhumation of the sole/peridotite pairs early in the subduction history. One important exception, further demonstrating the existence of subduction gradient cooling, is the blueschist facies overprint found on some metamorphic soles of Turkey (Plunder et al., 2016).

— Basal (banded) peridotites:

The Newfoundland exposures are the best and most thoroughly studied so far. Fine-banded ultramafic rocks are found both in the north (White Hills: Williams and Smyth, 1973; Jamieson, 1981) and west of the island (Bay of Islands; e.g., Table Mountains: McCaig, 1983; Lewis Hill: Suhr, 1993; Suhr and Cawood, 1993). Banding develops across $\sim 100\text{m}$, but mylonitization appears to be a few meters thick on average ($\sim 5\text{-}10\text{ m}$; Williams and Smyth, 1973; McCaig 83). Banding is, in general, more spatially restricted in the Appalachians than in Oman-UAE. The presence of ultramafic ultramylonites is reported within the first 1-3 m of the contact with the metamorphic sole only. Banded peridotites have also been described in Greece, where microstructures range from coarse porphyroclastic to mylonitic at the base of

the Pindos ophiolite (Pelletier et al., 2008), or in Alaska (Harris, 1998). In Mt Albert, despite intense deformation (see below), banding is less developed, with only rough secondary LT foliation superimposed on the HT mantle layered fabric. This seems also true for the Josephine ophiolite (Harper et al., 1994 and references therein).

The mineralogy of basal peridotites generally comprises olivine, orthopyroxene, spinel and variable amounts of clinopyroxene, with an evolution towards more clinopyroxene and amphibole closer to the plate interface contact (Suhr and Batanova, 1998). Amphibole, as in Oman-UAE, is present in most ultramylonites, in places in bands replacing clinopyroxene (Suhr, 1993). Exsolution of plagioclase is observed in orthopyroxene (Jamieson, 1981). As in Oman-UAE (Fig. 9g), systematic changes in orthopyroxene composition accompany increasing deformation (i.e., decreasing Al content in White Hills; Jamieson, 1981). In Québec (MacGregor and Basu, 1979) and in Greece (Pelletier et al., 2008), the transition from porphyroclastic to protomylonitic peridotites shows the appearance of polymineralic domains, similar to those shown in figures 10 and 11, with fine-grained neoblasts of olivine, orthopyroxene, spinel and clinopyroxene. Secondary pyroxenes lack exsolution lamellae (Pelletier et al., 2008), as reported by Prigent et al. (2018a). P-T conditions for basal peridotites were rarely estimated, but are thought to be around 0.8-1.2 GPa at 850-900°C for Newfoundland (Jamieson 1980, 1981, 1986; McCaig, 1983), consistent with the presence of spinel and with estimates for Oman-UAE (Prigent et al., 2018a).

3.5.2 Deformation mechanisms and element transfer across sole/peridotites interfaces

Together with deformation patterns, the consistency of deformation temperatures experienced by basal peridotites and HT metamorphic soles, near 850-900°C, has been reported in most ophiolites (e.g., Jamieson, 1981; Spray, 1984; Boudier et al., 1988; Harper et al., 1994; Suhr and Cawood, 1993; Parlak et al., 2019). Deformation features relate to either coupling or strain localization.

— High temperature deformation testifying to viscous coupling:

At outcrop scale, a spectacular and exceptionally well-preserved example of joint HT deformation is found in Newfoundland (Lewis Hill, Suhr, 1993; Suhr and Cawood 1993): metamorphic sole amphibolites are interleaved with ultramafic rocks across a ~200 m thick zone. This contrasts with the thin banding of other regional exposures (Table mountains, White Hills) and with Semail, where no such intimate imbrication has been described. Amphibolites show a pronounced lineation and high L/S fabric. The interbanding is present even at thin section scale (Suhr, 1993). In addition, 100-200 m long mafic/ultramafic megalenses, or boudins, are found in the basal peridotites (Suhr and Cawood, 1993). These observations demonstrate (i) extreme shearing along the subduction interface during early

subduction and (ii) distribution of deformation on a scale of 500 m- 1 km at least across the interface.

At mineral scale, evidence must be looked for in the hottest and best-preserved granulite facies samples, since they were subtracted from the slab just before, i.e., as close as possible to the point of deep coupling. In Mt Albert, HTa samples exhibit a compact framework with nearly equant textures and relatively constant and coarse grain size (Dubacq et al., 2019; Fig. 13a). Systematic undulose extinction for clinopyroxene advocates for activation of dislocation creep. Compositional layering can be observed in some samples, but with only very limited strain localization. Fracturing of all minerals, i.e. garnet, clinopyroxene and amphibole is conspicuous (Figs. 13a-c), as for the Oman-UAE example. Dissolution-precipitation creep, in contrast, seems to have played a minor role.

— Evidence for progressive strain localization:

Grain size reduction is observed in all localities. In Newfoundland, grain sizes comprised between 20 and 100 μm for all phases are reported near the sole/peridotite contact (Suhr, 1993; see Fig. 9f for comparison). In Québec, grain sizes <50 μm are found in dunite ultramylonites ('equigranular mosaic texture'; MacGregor and Basu, 1979). Evidence of active dissolution-precipitation creep, as for the Semail example, is marked by the crystallization of synkinematic amphibole within cm and up to 1 m wide shear zones near the contact (Suhr, 1993), and of a secondary generation of peridotitic minerals within mylonitic shear bands (Pelletier et al., 2008).

— Element/fluid transfer:

In Newfoundland, mylonites located at the base of the mantle have been considered as metasomatized (Church 1972; Maipas 1979). They comprise fine-grained pargasitic amphibole and are characterized by enrichments in K, LREE Ti, a higher Fe/Mg ratio, and depletion in Mg, Cr, Ni (Jamieson, 1981; McCaig et al., 1983). In New Caledonia, protomylonitic peridotites interpreted as having formed in a nascent arc (Pirard et al., 2013) show similar specific enrichments in FME (Figs. 13e,f; Soret et al., 2016). There, mafic dikes emplaced in the mantle reveal the presence of talc and of a series of infiltration events by aqueous, metamorphic sole derived fluids, first Ca-Al- then K-Ba-rich, at temperatures between ~850 and 700°C (Soret et al., 2016; compare with figure 12a). In Pindos basal peridotites, crystallization of pargasite, hornblende and talc near 750°C is also accompanied by FME enrichment (Pelletier et al., 2008), predating later serpentinisation.

Late serpentinisation (<600-650°C) enhances the formation of discrete shear zones in basal peridotites or may locally rework former HT shear bands (Soret et al., 2016), but is commonly restricted spatially to fractures (see Jamieson, 1981; as in figure 11f). More intense serpentinisation is nevertheless reported in Alaska (Harris, 1998), Greece (Jones and Robertson, 1991) or in New Caledonia ('mur à silice'; e.g., Ulrich et al., 2014).

4. Discussion

4.1 Interplay between deformation, reactions and fluids/melts during subduction infancy: rheological changes through space and time, competition between viscous coupling and strain localization

Field observations, microstructural and geochemical data on the metamorphic sole \ banded peridotite frozen-in interface reveal systematic changes in structures, mineral frameworks and rheologies through time. Figure 14 encapsulates the main lessons from the Semail case study and similar settings around the world.

As shown in § 3, dissolution-precipitation processes, metamorphic reactions, grain size reduction, activation of GSS deformation mechanisms are processes common to both the top of the downgoing slab (metamorphic sole) and the incipient mantle wedge (banded peridotites). This unique geological configuration reveals how strain weakening/localization operates via mineral reactions, hydration and phase mixing and how increasing strain localization develops with decreasing temperature, allowing subduction to proceed. Ultimate localization as a sharp subduction interface occurs when the subduction plate boundary has cooled sufficiently, thereby extending serpentine stability to great depths (Fig. 5b), near the stable coupling depth (Fig. 1c).

(1) Several other important conclusions can be drawn, regarding progressive strain localization and decoupling accompanying slab descent (Fig. 14):

— At ~ 850°C, under granulite/amphibolite facies conditions, strain localization is triggered by transient events, in part brittle. Fractures observed in garnet, amphibole and clinopyroxene in peak HTa and HTa, and in orthopyroxene in banded peridotites (Fig. 14a) act as nucleation sites for fluid ingress, mineral crystallization and further deformation. At the large-scale, progressive strain localization leads to mechanical decoupling and unzipping of the plate interface. Embrittlement mechanisms at depths in mature subduction are the matter of considerable debate (Davies, 1999; Hacker et al., 2003). Current hypotheses include fluid release (dehydration embrittlement, e.g. from amphibole breakdown), mineral reactions and evolving mineral assemblages (Mansard et al., 2020), stress transfer (Ferrand et al., 2017), self-localizing thermal runaway (John et al., 2009). They could also arise from concentrations on hard phases, contrasts in strain rates, or variations in phase mixing/grain pinning (Herwegh et al., 2011; Platt, 2015).

— The role of dissolution-precipitation creep is essential in allowing mechanical decoupling, as seen from its increasing role during retrogression of HTa (Fig. 14b), prograde burial of HTb metamorphic soles (§ 3.3) and deformation of banded peridotites (and even during later serpentinisation). There is a strong positive feedback with fluid influx and as soon

(or as long as) fluids are present, deformation will tend to be focused near fluid migration pathways, and vice-versa. Dissolution-precipitation, in addition to (and rather than) dislocation creep, should be used to model subduction processes down to the coupling point at least. While existing flow laws for dislocation creep predict a range of viscosities seemingly in agreement with the requirements of plate tectonics (Fig. 7b; i.e., 10^{20-21} Pa.s; Regenauer-Lieb et al., 2001; Billen and Hirth, 2007) and with the switch in viscosities between the mantle and crust inherent to subduction infancy (Fig. 7b; Agard et al., 2016), such rheologies used in numerical models are intrinsically inappropriate. DPC, unfortunately, is not yet quantitatively constrained for (reacting) polymineralic rocks at these depths and temperatures (Gratier et al. 2013; Wassmann and Stöckhert, 2013).

— Amphibole plays a key role in the interaction between deformation, reactions and fluids/melts. In slab lithologies, amphibole accommodates a significant amount of deformation through progressive crystallization (Fig. 14c) and creates anisotropy. It contributes to either fluid delivery or storage. Through the onset of fracturation, amphibole may largely control the stepwise detachment and accretion of slices to the mantle (Soret et al., 2019). The respective role of amphibole and plagioclase in the thinning of the HTa metamorphic sole by a factor of 5 to 10 is however still to be clarified.

(2) Importantly, metamorphic sole \ banded peridotite pairs allow constraining the mechanisms controlling viscous coupling during subduction infancy (Fig. 14d): these rocks are the very last witnesses, since they were ultimately exhumed, before irreversible coupling and sinking into the mantle. Coupling fundamentally ensues from the complex set of mineral/rock changes occurring during burial (e.g., Figs. 14a-c). Understanding how coupling operates therefore requires determining which critical mechanical process(es) sharply reduce strain localization so that the slab and upper plate mantle become attached at given depths.

Our observations indicate that transformations opposite to those documented during retrogression of the HTa sole \ peridotite pair (i.e. fluid ingress, dissolution-precipitation processes, retrograde reactions, grain size reduction) take place during the prograde evolution, when amphibolites reach conditions of HTb and then transform into peak HTa granulites (Figs. 7a, 13a-c, 14a):

— The increase in temperature and partial breakdown of amphibole, as the tip of the newborn slab attempts to progress (Figs. 1a,b, 7a), result in the preferential crystallization of strong and dry minerals (garnet and clinopyroxene of peak HTa), grain coarsening, shortage of fluids, and therefore a marked decrease in the efficiency, or even disappearance of dissolution-precipitation creep on both sides of the interface.

— When the slab crust transforms at 900-850°C into a dominantly dry, Grt-Cpx-bearing granulite with similar effective viscosity to the dry porphyroclastic mantle tectonite (Figs. 7b, 14a,d), the plates become fully coupled.

Along with temperature increase, reaction-driven mineral changes and progressive dehydration, the onset of subduction zone viscous coupling appears driven by this fundamental transition in deformation mechanisms from dominant fluid-mediated, grain-size sensitive, dissolution-precipitation creep to dislocation creep (Fig. 14d).

4.2 Deep viscous coupling in mature subduction zones: mechanisms, significance and implications for sub-arc depths

Mature subduction is inherently modulated by deep mechanical coupling where the slab, and more generally plate tectonics, meets mantle convection (Fig. 15a). Where deep coupling is achieved (i) no mechanical plate interface exists anymore (Fig. 15b), but only a contrast in chemistry between the mantle and the crustal, mafic and sedimentary layer, and (ii) deformation gets distributed over a thick zone (\gg km; Fig. 15c).

As mentioned before, no physical-chemical explanation exists so far as to how, where exactly and why deep coupling operates, seemingly near $\sim 80 \pm 30$ km depth (Wada et al., 2008; Wada and Wang, 2009; see discussion in Arcay, 2017). This affects predictions for rock transformations with depth and temperature, fluid expulsion (Fig. 1d; Hacker, 2008; van Keken et al., 2011; Faccenda, 2013; Paulatto et al., 2017), mantle wedge serpentinisation (Fig. 15a; Hyndman et al., 2003; Arcay et al., 2005; Angiboust et al., 2012; Bouilhol et al., 2015; Abers et al., 2017), and the source and migration of melts (England and Katz, 2010; Behn et al., 2011; Wada and Behn, 2015; Nielsen and Marschall, 2017). It also impacts estimates of mantle viscosity, hence postseismic loading and SKS patterns (Fig. 15a; Schaeffer and Lebedev, 2013; Tommasi et al., 2006; Osei Tutu et al., 2018), short-term seismogenesis and seismic hazard (Moreno et al., 2011; Wang et al., 2012; Métois et al., 2016).

Based on frozen-in plate interfaces, we infer that the transition in deformation mechanisms, from dominant fluid-mediated grain-size sensitive creep (DPC) to dislocation creep (Fig. 14d), drives strain delocalization and viscous coupling at depth in mature subduction zones too. This explains how the sinking slab gets (re)coupled to the upper plate and becomes part of the system of mantle convection (Fig. 15a,c). In this interpretation, the along dip spatial evolution of mineralogy, deformation mechanisms and fluid release in present-day mature subduction zones is analogous to the onset of viscous coupling during the prograde stages of subduction infancy (Fig. 15c): successive mineral transformations lead to essentially dry rocks in the slab facing similarly dry rocks in the mantle wedge (Figs. 15b,c). The increased amount of melting predicted immediately downdip of this depth range further reduces DPC by dehydrating the rocks (Fig. 15c). Disappearance of a significant viscosity contrast provides a natural mechanism for the 'common' viscous coupling depth (Figs. 7a, 15a,b).

The entire process leading to progressive coupling through space in mature subduction zones (Fig. 15c) is therefore opposite to the progressive strain localization through time, at depths $\leq 80-100$ km, documented by metamorphic sole \ banded peridotite pairs during subduction infancy (Fig. 5b; 14d). In a broader perspective, deep coupling can also be viewed as the simple geodynamic consequence of the transition between a fluid-rich environment, i.e. the shallow lithosphere and slab material, and the fluid-starved deep earth. From nascent to mature subduction and with cooling, viscous coupling progressively deepens to reach $\sim 80-100$ km (Fig. 16a), with timescales discussed in the next section (§4.3).

Further supporting evidence comes from the similar transformations witnessed by LT eclogites in mature subduction zones (Figs. 1e,16). Sodic amphibole and/or lawsonite (or epidote for warmer subduction) indeed break down at $\sim 80-100$ km depth and approximately $550-600^{\circ}\text{C}$ to form dry garnet-clinopyroxene-bearing eclogite (Fig. 1e; Hacker et al., 2003; Van Keken et al., 2011; Locatelli et al., 2019; see Agard et al., 2009). A notable difference with subduction infancy is pressure (2.5-3 GPa instead of 1 GPa), but the temperature conditions for coupling similarly transition between 550 and 850°C across a narrow spatial domain (Fig. 1c; England and Wilkins, 2004; Abers et al., 2017) — and temperature has a larger effect on dehydration reactions.

The fossil rock record provides independent constraints on the P-T conditions of coupling (Fig. 16b). Since all recovered subducted fragments have remained above the coupling depth, the rock record (blue envelope in figure 16b) provides a minimum bound on coupling conditions through time. This information can be compared to the T-depth range across which mafic slab crust is predicted to dehydrate for a cold, intermediate or warm subduction gradient (white dots labelled c, i, w, respectively; Fig. 16b; Hernandez-Urbe and Palin, 2019). The match between these estimates and the envelope is impressive, further supporting the idea that fluid availability has a key role on viscous coupling.

We particularly stress, as shown by figure 16b, that no single reaction can explain the location (and evolution) of the coupling 'depth' in P-T space. This is why a more general mechanism is needed, such as the reduction of DPC in response to the decrease in fluid transfer (Fig. 15c), rather than simply deserpentinisation for example. Depending on subduction thermal regime (e.g., van Keken et al., 2011), viscous coupling will take place at somewhat different depths, ranging from slightly less than 2 GPa for warm subduction zones to 2.5-3 GPa for cold ones (~ 60 and 90 km respectively; Fig. 15b).

Self-consistent, mantle convection or lithospheric scale geodynamic models should therefore use rheologies incorporating DPC and mineral reactions, aside dislocation and solid diffusion creep laws (Kelemen et al., 2003; Bürgmann and Dresen, 2008; Arcay, 2017; Fagereng and den Hartog, 2017; Moresi and Sanders, 2019), in order to consider progressive chemical/structural changes as witnessed by rocks returned from deep

subduction (Agard et al., 2009, 2018; Billen and Arredondo, 2018). This is prerequisite to reliably estimating the thermal structure of the subduction wedge and dependent processes (e.g., intermediate-depth seismicity, mantle viscosity,...). This combined chemical and mechanical evolution has also important consequences for metasomatism and element/fluid transfer (Fig. 1d), only briefly mentioned here (§ 3.4; Fig. 14d).

As a final note, the possible existence of intermittent and/or double-sided rather than single-sided subduction during the Archean (Sizova et al., 2010; van Hunen and Moyen, 2012; Crameri et al., 2012) would mean that the coupling point remained shallow and that both lithospheres were dragged down together, when warmer geotherms prevailed. A possible interpretation is that insufficient cooling of the subduction system, hence insufficient lubrication by stabilization of serpentinite deep down, prevented the asymmetry of 'modern' subduction (< 1 Ga). Consistent with this interpretation, there are in fact only few ophiolites >1 Ga and none of them exhibits a metamorphic sole (Moore, 2002).

4.3 Timescales of slabitization: early slab dynamics, viscous coupling, mantle upwelling (and potential genesis of forearc lithosphere or supra-subduction ophiolite) and mantle counterflow

Slabitization entails successful strain localization and slab penetration to achieve decoupling down to the deep mechanical coupling zone (Fig. 15a; § 4.2). A key question is how long subduction stabilization lasts, from the moment the process is triggered (Agard et al., 2007, 2014; Qian et al., 2020) until it becomes self-sustainable and 'steady'.

Active sites of subduction nucleation can be found, for example, to the north of the Puysegur trench (New-Zealand; Gurnis et al., 2019; see also Martinez et al., 2018 for the southern Marianas), while subduction infancy is probably represented by the very young Matthews and Hunter subduction zone (South-West Pacific; Patriat et al., 2018). Being essentially transient, both processes are difficult to catch in action and still poorly documented, particularly in terms of duration.

Age constraints are available for two distinct, thoroughly studied geological settings which can provide complementary information on slab dynamics during subduction infancy (e.g., Stern et al., 2012):

— ophiolites and metamorphic soles, through their relative timing of formation (Fig. 3a,b). For the Semail example, ophiolite formation was short-lived at 96 ± 0.5 Ma (Rioux et al., 2016 and references therein). Recent Lu/Hf age constraints for garnet growth indicate burial of the HTa metamorphic sole $\sim 7-8$ Ma before ophiolite formation ($\sim 104-103$ Ma; Guilmette et al., 2018). A similar conclusion was drawn for the granulitic facies sole in Turkey (104-103 Ma; Pourteau et al., 2019), where a similarly tight age cluster exists for the large-scale

ophiolite above (93 ± 0.5 Ma; Celik et al., 2011). Most other radiometric ages for HTa and HTb are around 97-93 Ma (Rioux et al., 2013; Garber et al., 2020) and probably represent retrogression, exhumation-related ages, at least for HTa. Magmatic products of the Semail ophiolite include boninites, generally interpreted as melt products of a depleted mantle fluxed by subduction-derived fluids (Whattam and Stern, 2011). The compositional similarity between the Semail boninites and metamorphic sole-derived fluids was underlined by Ishikawa et al. (2005). Oceanic subduction was short-lived, between 110-105 and ~85-80 Ma, since continental subduction of the Arabian margin peaked at ~80 Ma (Warren et al., 2005). The calc-alkaline magmatic arc associated with subduction, if any, was not obducted. A 88-87 Ma intraoceanic arc remnant was nevertheless discovered outboard of the Oman margin (Bonnet et al., 2020).

— intraoceanic subduction, through the chronology of initial magmatic products. A classic example is the Western Pacific Izu-Bonin/Marianas (IBM) fore arc formed following early Eocene subduction initiation (e.g., Stern and Bloomer, 1992; Reagan et al., 2019 and references therein). Short-lived mantle upwelling, following subduction initiation, is documented at ~52-51 Ma by the eruption of forearc basalts (FAB; representing melting of undepleted but dry mantle), then boninites ~1 Ma later, and finally classical calc-alkaline volcanics at ~45-44 Ma (Reagan et al., 2010, 2019; Ishizuka et al., 2011, 2020). But no oceanic lithosphere was obducted nor metamorphic soles exhumed, so that the start of subduction cannot be firmly established. Recent datings of rutile in mm- to cm-scale blueschist facies fragments from serpentinite seamounts, at 48-47 Ma (Tamblyn et al., 2019) suggest a ~4 Ma time lag between subduction infancy and cooling of the subduction interface to ~600°C at ~50 km depth.

Based on observations from sole/peridotite pairs we propose a tectonic scenario for early slab dynamics (Fig. 17), which refines the one proposed for the IBM and later generalized to Tethyan ophiolites (Stern and Bloomer, 1992; Whattam and Stern, 2011). General dynamics may be more robust than timescales, which heavily rely on time constraints from the Semail and Izu-Bonin examples (in orange and blue, respectively in figure 17).

(a) Subduction nucleation (Fig. 17a) follows regional-scale plate reorganization. This happened at 110 ± 5 Ma for Neotethyan ophiolites (Agard et al., 2006, 2007; Matthews et al., 2012). Examples of truly spontaneous subduction nucleation are scarce in nature (possibly the IBM or some plume-induced setting such as in the Caribbean) and are mostly studied through numerical modelling (see Stern and Gerya, 2018).

(b) Initial mechanical coupling and resistance to slab penetration (Fig. 17b) make subduction infancy sluggish (reminiscent of the 'slow start' of Anczkiewicz et al., 2004). Prograde garnet growth is recorded at 104-103 Ma (Guilmette et al., 2018). This early stage ends with the peak burial and accretion of HTa to the peridotites. In the case of Semail,

available age constraints indicate that this occurs prior to 97-93 Ma (Rioux et al., 2013), so that this stage would last ~7-8 Ma.

(c) With cooling, strain localization develops and the locus of viscous coupling starts migrating downwards, unzipping the plate interface. Once this happens, the slab starts progressing down, slab penetration initiates local mantle upwelling (Fig. 17c; Pearce et al., 1984; Shervais, 2001), and potentially local slab retreat (Whattam and Stern, 2011). Mantle upwelling is probably most common, but not systematic, as shown by some obducted Tethyan ophiolites made of 'old' lithosphere (e.g., Iran, Armenia; Agard et al., 2011; Hassig et al., 2016). Melting of undepleted upwelling dry asthenosphere, and then of depleted but fluid-fluxed asthenosphere may give birth to the short-lived succession of MORB-type forearc basalts (FAB) then boninite products, as observed in Izu-Bonin ($\sim 51 \pm 1$ Ma) and in the Semail ophiolite (96 ± 0.5 Ma). Ophiolite formation impinges on older lithosphere (e.g., Neotethys, NT; Fig. 17d), either not preserved or limited to outermost mantle fragments, such as those found to the SW of the Semail ophiolite.

This stage coincides with the early exhumation and thinning of HTa metamorphic soles and adjacent banded peridotites (Fig. 17d). Uncertainties remain as to the engine driving their joint partial exhumation (Agard et al., 2016; Rioux et al., 2016; see also Dewey and Casey, 2013 for other locations worldwide), most likely some combination of buoyancy and/or shearing by the base of the upwelling dry mantle. In any case the mantle of the Semail ophiolite appears twofold, its lower part representing the fossil mantle sheared and exhumed with the HTa metamorphic sole while its shallow counterpart represents the base of the newly formed (and ultimately obducted) lithosphere. No major contact has been mapped between the two, consistent with the huge downward gradient in deformation and mineral chemistry within the base of the Semail mantle (Takazawa et al., 2003; Prigent et al., 2018a).

This stage also coincides with the accretion of the HTb sole. Tight age constraints are however lacking for now: available ages between 97 and 93 Ma could date accretion or mark later retrogression (e.g., Hacker, 1994; Warren et al., 2005; Rioux et al., 2016; Roberts et al., 2016).

(d) Slab stabilization ends with stabilization of deep viscous coupling near 80-100 km depth (Fig. 17d). Slab pull is then fully coupled to mantle convection, early asthenospheric upwelling is reversed to mature mantle counterflow (contrary to stage c), and the subduction zone has been extensively decoupled and 'refrigerated' (Ernst, 2001), leading to the formation of LT eclogites. Due to the onset of downward mantle counterflow this period is probably not propitious for significant melting, explaining the ~7 Ma delay between the short-lived emplacement of FAB and boninites and profuse calc-alkaline magmatism.

The last metamorphic sole accreted before final lubrication is the metasedimentary LT sole (Fig. 17e). During this period, when viscous coupling reaches depths >50-60 km, P-T conditions along the subduction interface are those of HT eclogites or high-grade blueschists

(Fig. 16a,b), which are occasionally exhumed as mafic blocks embedded in serpentinized mantle (Agard et al., 2018; their Fig. 10). The Izu-Bonin 'blueschists', which belong to this category, provide a landmark for this stage ~4 Ma after stage c. The warm blueschist overprint of metamorphic soles in Turkey is also consistent with a 5-10 Ma duration (Plünder et al., 2015, 2016; see Fig. 16a).

(e) From stage (d) onwards, subduction is mature/steady, with stable viscous coupling, formation of (rarely exhumed) LT eclogites, and melting of the hydrated mantle wedge at sub-arc depths marked by calc-alkaline magmatism. The Izu-Bonin example suggests that this may have happened ~7 Ma after ophiolitic lithosphere formation (Ishizuka et al., 2020). Calc-alkaline remnants in the Neotethys outboard of Oman, dated at 88-87 Ma (Bonnet et al., 2020a,b), point to a similar duration. Oceanic subduction lasted another 5-10 Ma in the case of the Arabian-Eurasia convergence (Agard et al., 2006) and was rapidly stalled by continental subduction of Arabia (case A; Fig. 3b). Metamorphic conditions experienced by the subducted continental slivers testify to cold subduction along a ~8-10°C/km gradient at >80 Ma (Goffé et al., 1988; Searle et al., 2004; Warren et al., 2005; Warren and Waters, 2006; Yamato et al., 2007; Agard et al., 2010; Massonne et al., 2013).

This overall tectonic evolution is consistent with numerical predictions of slow subduction initiation on the order of 10 Ma (Dymkova and Gerya, 2013).

5. Conclusions

Pairs of metamorphic soles and banded peridotites underlying ophiolites provide a unique opportunity to study the interactions between mineral reactions, deformation and fluid migration at the subduction interface, with two sides preserved and still attached to each other, shortly after subduction initiation (i.e. during subduction infancy).

This study documents how the interplay between dehydration/hydration reactions and rock deformation at the subduction interface, through processes of metamorphic reactions, dissolution-precipitation, grain size reduction, and phase mixing on each side of the interface controls strain localization and facilitates slab penetration. The role of dissolution-precipitation creep (DPC), in particular, promoted in fluid-rich conditions, appears paramount.

Importantly, mineral fracturation (e.g., of orthopyroxene in peridotites, of garnet, amphibole and to a lesser extent clinopyroxene in metamorphosed oceanic crust) is critical to trigger the first steps of this complex interplay ultimately leading to strain localization.

These pairs also constitute a window onto processes responsible for deep mechanical coupling (i.e., the 'common depth of viscous coupling'; Wada and Wang, 2008). Based on observations integrated across the interface, the depth range and P-T conditions where this happens correlate with the loss or drastic reduction of hydrous phases, mineral growth of

garnet-clinopyroxene assemblages in the slab (in granulites during early subduction, in LT eclogites in mature subduction zones) and the formation of a load-bearing framework deforming mostly by dislocation creep on both sides. We propose that suppression of efficient DPC is the mechanism that accounts for deep mechanical coupling. Companion processes, such as the onset of significant melting predicted immediately downdip of this depth range may contribute to additional dehydration, hence further reducing DPC.

From nascent to mature subduction, during 'slabification', the interplay between metamorphic reactions and dissolution-precipitation creep controls plate interface dynamics: (1) suppression of fluid transfer and DPC at depth during subduction infancy triggers viscous coupling near ~ 30 km depth; the period from subduction nucleation to effective accretion of HTa metamorphic soles may last ~5-8 Ma; (2) with increased cooling and fluid availability, strain localization develops downwards, unzipping the subduction interface; the onset of the downward migration of viscous coupling triggers localized mantle upwelling, which may lead to short-lived (~1-2 Ma) forearc lithosphere or suprasubduction ophiolite formation; (3) the locus of deep viscous coupling stabilizes near ~80-100 km in mature cold subduction zones, approximately after 7 Ma. This is where and when newborn slabs become part of the self-organizing plate tectonics / mantle convection system, paving the way for large-scale slab retreat, mantle upwelling and mature calc-alkaline magmatism. Intraoceanic subduction initiation, whose dead-end can be ophiolite emplacement through obduction (as for Semail and other examples worldwide), appears to be a rather sluggish process, on the order of 10 Ma at least.

This study provides a general description of strain localization/delocalization processes in lithospheric-scale subduction shear zones, with potential application to other plate boundaries dominated by oceanic crust and mantle rheologies (e.g., core-complexes). Sole/peridotite pairs also inform on element transfer in warm subduction settings active today, where slab material gets amphibolitized at depths of ~40 km (e.g., Cascadia, Nankai), or during early Earth (possibly >2 Ga), when warmer geotherms prevailed.

Acknowledgements

The authors wish to thank Bob Stern and Carl Guilmette for their reviews which helped improve this manuscript, and to many colleagues for fruitful and stimulating discussions, particularly L. Le Pourhiet, H. Stunitz, H. Raimbourg, M. Godard. This research was funded through the ANR project ONLAP (ANR-10-BLAN-0615) granted to P.A.

References

- Abers, G.A., Keken, P.E. van, Hacker, B.R., 2017. The cold and relatively dry nature of mantle forearcs in subduction zones. *Nature Geoscience* 10, 333–337. <https://doi.org/10.1038/ngeo2922>
- Abers, G.A., van Keken, P.E., Kneller, E.A., Ferris, A., Stachnik, J.C., 2006. The thermal structure of subduction zones constrained by seismic imaging: Implications for slab dehydration and wedge flow. *Earth and Planetary Science Letters* 241, 387–397.
- Agard, P., Jolivet, L., Vrielynck, B., Burov, E., Monie, P., 2007. Plate acceleration: the obduction trigger? *Earth and Planetary Science Letters* 258, 428–441.
- Agard, P., Monié, P., Gerber, W., Omrani, J., Molinaro, M., Meyer, B., Labrousse, L., Vrielynck, B., Jolivet, L., Yamato, P., 2006. Transient, synobduction exhumation of Zagros blueschists inferred from P-T, deformation, time, and kinematic constraints: Implications for Neotethyan wedge dynamics. *Journal of Geophysical Research: Solid Earth* 111.
- Agard, P., Omrani, J., Jolivet, L., Whitechurch, H., Vrielynck, B., Spakman, W., Monié, P., Meyer, B., Wortel, R., 2011. Zagros orogeny: a subduction-dominated process. *Geological Magazine* 148, 692–725.
- Agard, P., Plunder, A., Angiboust, S., Bonnet, G., Ruh, J., 2018. The subduction plate interface: rock record and mechanical coupling (from long to short timescales). *Lithos* 320–321, 537–566. <https://doi.org/10.1016/j.lithos.2018.09.029>
- Agard, P., Searle, M.P., Alsop, G.I., Dubacq, B., 2010. Crustal stacking and expulsion tectonics during continental subduction: P-T deformation constraints from Oman. *Tectonics* 29.
- Agard, P., Yamato, P., Jolivet, L., Burov, E., 2009. Exhumation of oceanic blueschists and eclogites in subduction zones: Timing and mechanisms. *Earth-Science Reviews* 92, 53–79. <https://doi.org/10.1016/j.earscirev.2008.11.002>
- Agard, P., Yamato, P., Soret, M., Prigent, C., Guillot, S., Funder, A., Dubacq, B., Chauvet, A., Monie, P., 2016. Plate interface rheological switches during subduction infancy: Control on slab penetration and metamorphic sole formation. *Earth Planet. Sci. Lett.* 451, 208–220. <https://doi.org/10.1016/j.epsl.2016.06.054>
- Agard, P., Zuo, X., Funicello, F., Bellahsen, N., Facca, C., Sawa, D., 2014. Obduction: Why, how and where. Clues from analog models. *Earth and Planetary Science Letters* 393, 132–145.
- Ambrose, T.K., Wallis, D., Hansen, L.N., Waters, D.J., Searle, M.P., 2018. Controls on the rheological properties of peridotite at a palaeosubduction interface: A transect across the base of the Oman–UAE ophiolite. *Earth and Planetary Science Letters* 491, 193–206.
- Anczkiewicz, R., Platt, J.P., Thirlwall, M.F., Wakabayashi, J., 2004. Franciscan subduction off to a slow start: evidence from high-resolution Lu-Hf garnet ages on high grade-blocks. *Earth Planet. Sci. Lett.* 225, 147–161. <https://doi.org/10.1016/j.epsl.2004.06.003>
- Angiboust, S., Glodny, J., Oncken, O., Chopin, C., 2014a. In search of transient subduction interfaces in the Dent Blanche-Sesia Tectonic System (W. Alps). *Lithos* 205, 298–321. <https://doi.org/10.1016/j.lithos.2014.07.001>
- Angiboust, S., Kirsch, J., Oncken, O., Glodny, J., Monie, P., Rybacki, E., 2015. Probing the transition between seismically coupled and decoupled segments along an ancient subduction interface. *Geochem. Geophys. Geosyst.* 16, 1905–1922. <https://doi.org/10.1002/2015GC005776>
- Angiboust, S., Pettke, T., De Hoog, J.C.M., Caron, B., Oncken, O., 2014b. Channelized Fluid Flow and Eclogite-facies Metasomatism along the Subduction Shear Zone. *J. Petrol.* 55, 883–916. <https://doi.org/10.1093/petrology/egu010>
- Angiboust, S., Wolf, S., Burov, E., Agard, P., Yamato, P., 2012. Effect of fluid circulation on subduction interface tectonic processes: Insights from thermo-mechanical numerical modelling. *Earth Planet. Sci. Lett.* 357, 238–248. <https://doi.org/10.1016/j.epsl.2012.09.012>
- Arcay, D., 2017. Modelling the interplate domain in thermo-mechanical simulations of subduction: Critical effects of resolution and rheology, and consequences on wet mantle melting. *Physics of the Earth and Planetary Interiors* 269, 112–132.
- Arcay, D., Tric, E., Doin, M.-P., 2005. Numerical simulations of subduction zones: effect of slab dehydration on the mantle wedge dynamics. *Physics of the Earth and Planetary Interiors* 149, 133–153.
- Audet, P., Bostock, M.G., Christensen, N.I., Peacock, S.M., 2009. Seismic evidence for overpressured subducted oceanic crust and megathrust fault sealing. *Nature* 457, 76.
- Audet, P., Bürgmann, R., 2014. Possible control of subduction zone slow-earthquake periodicity by silica enrichment. *Nature* 510, 389.
- Bayet, L., John, T., Agard, P., Gao, J., Li, J.-L., 2018. Massive sediment accretion at ~80 km depth along the subduction interface: Evidence from the southern Chinese Tianshan. *Geology* 46, 495–498. <https://doi.org/10.1130/G40201.1>

- Bebout, G.E., 2007. Metamorphic chemical geodynamics of subduction zones. *Earth and Planetary Science Letters* 260, 373–393. <https://doi.org/10.1016/j.epsl.2007.05.050>
- Bebout, G.E., Ryan, J.G., Leeman, W.P., Bebout, A.E., 1999. Fractionation of trace elements by subduction-zone metamorphism—effect of convergent-margin thermal evolution. *Earth and Planetary Science Letters* 171, 63–81.
- Bedford, J., Moreno, M., Baez, J.C., Lange, D., Tilmann, F., Rosenau, M., Heidbach, O., Oncken, O., Bartsch, M., Rietbrock, A., 2013. A high-resolution, time-variable afterslip model for the 2010 Maule Mw= 8.8, Chile megathrust earthquake. *Earth and Planetary Science Letters* 383, 26–36.
- Behn, M.D., Kelemen, P.B., Hirth, G., Hacker, B.R., Massonne, H.-J., 2011. Diapirs as the source of the sediment signature in arc lavas. *Nature Geoscience* 4, 641.
- Benoit, M., Ceuleneer, G., Polvé, M., 1999. The remelting of hydrothermally altered peridotite at mid-ocean ridges by intruding mantle diapirs. *Nature* 402, 514–518.
- Bercovici, D., 2003. The generation of plate tectonics from mantle convection. *Earth and Planetary Science Letters* 205, 107–121.
- Bercovici, D., Ricard, Y., 2014. Plate tectonics, damage and inheritance. *Nature* 508, 513.
- Bercovici, D., Ricard, Y., 2012. Mechanisms for the generation of plate tectonics by two-phase grain-damage and pinning. *Physics of the Earth and Planetary Interiors* 202, 27–55.
- Bickle, M.J., McKenzie, D., 1987. The transport of heat and matter by fluids during metamorphism. *Contributions to Mineralogy and Petrology* 95, 384–392.
- Billen, M.I., Arredondo, K.M., 2018. Decoupling of plate-asthenosphere motion caused by non-linear viscosity during slab folding in the transition zone. *Physics of the Earth and Planetary Interiors* 281, 17–30.
- Billen, M.I., Hirth, G., 2007. Rheologic controls on slab dynamics. *Geochemistry, Geophysics, Geosystems* 8.
- Bonnet, G., Agard, P., Angiboust, S., Monie, P., Jentzer, M., Omrani, J., Whitechurch, H., Fournier, M., 2018. Tectonic slicing and mixing processes along the subduction interface: The Sistan example (Eastern Iran). *Lithos* 310, 269–287.
- Bonnet, G., Agard, P., Angiboust, S., Fournier, M., Omrani, J., 2019. No large earthquakes in fully exposed subducted seamount. *Geology* 47, 407–410.
- Bonnet, G., Agard, P., Whitechurch, H., Fournier, M., Angiboust, S., Caron, B., Omrani, J., 2020. Fossil seamount in southeast Zagros records intraoceanic arc to back-arc transition: New constraints for the evolution of the Neotethys. *Gondwana Research* 81, 423–444.
- Boudier, F., Ceuleneer, G., Nicolas, A., 1992. Shear zones, thrusts and related magmatism in the Oman ophiolite: initiation of thrusting on an oceanic ridge. *Tectonophysics* 151, 275–296.
- Boudier, F., Nicolas, A., Ildefonse, B., 1996. Magma chambers in the Oman ophiolite: fed from the top and the bottom. *Earth and Planetary Science Letters* 144, 239–250.
- Bouilhol, P., Magni, V., van Hunen, J., Kaislaniemi, L., 2015. A numerical approach to melting in warm subduction zones. *Earth and Planetary Science Letters* 411, 37–44.
- Bürgmann, R., Dresen, G., 2008. Rheology of the lower crust and upper mantle: Evidence from rock mechanics, geodesy, and field observations. *Annu. Rev. Earth Planet. Sci.* 36, 531–567.
- Cao, Y., Jung, H., Song, S., Park, M., Jung, S., Lee, J., 2015. Plastic deformation and seismic properties in fore-arc mantles: a petrofabric analysis of the Yushigou Harzburgites, North Qilian Suture Zone, NW China. *Journal of Petrology* 56, 1897–1944.
- Casey, J.F., Dewey, J.F., 1984. Initiation of subduction zones along transform and accreting plate boundaries, triple-junction evolution, and forearc spreading centres—implications for ophiolitic geology and obduction. *Geological Society, London, Special Publications* 13, 269–290. <https://doi.org/10.1144/GSL.SP.1984.013.01.22>
- Çelik, Ö.F., Marzoli, A., Marschik, R., Chiaradia, M., Neubauer, F., Öz, İ., 2011. Early–middle Jurassic intra-oceanic subduction in the İzmir-Ankara-Erzincan Ocean, northern Turkey. *Tectonophysics* 509, 120–134.
- Ceuleneer, G., Nicolas, A., Boudier, F., 1988. Mantle flow patterns at an oceanic spreading centre: the Oman peridotites record. *Tectonophysics* 151, 1–26.
- Church, W.R., 1972. Ophiolite: its definition, origin as oceanic crust, and mode of emplacement in orogenic belts, with special reference to the Appalachians, in: *The Ancient Oceanic Lithosphere*. Dept. of Energy, Mines and Resources Ottawa, Canada, p. 71.
- Coleman, R.G., 1981. Tectonic setting for ophiolite obduction in Oman. *Journal of Geophysical Research: Solid Earth* 86, 2497–2508.
- Coleman, R.G., 1971. Plate tectonic emplacement of upper mantle peridotites along continental edges. *Journal of Geophysical Research* 76, 1212–1222.
- Coltice, N., Gérard, M., Ulvrová, M., 2017. A mantle convection perspective on global tectonics. *Earth-science reviews* 165, 120–150.

- Coltice, N., Husson, L., Faccenna, C., Arnould, M., 2019. What drives tectonic plates? *Science advances* 5, eaax4295.
- Conrad, C.P., Lithgow-Bertelloni, C., 2002. How mantle slabs drive plate tectonics. *Science* 298, 207–209.
- Cowan, R.J., Searle, M.P., Waters, D.J., 2014. Structure of the metamorphic sole to the Oman Ophiolite, Sumeini Window and Wadi Tayyin: implications for ophiolite obduction processes, in: Rollinson, H.R., Searle, M.P., Abbasi, I.A., AlLazki, A.I., AlKindi, M.H. (Eds.), *Tectonic Evolution of the Oman Mountains*. Geological Soc Publishing House, Bath, pp. 155–175.
- Cramer, F., Tackley, P.J., Meilick, I., Gerya, T.V., Kaus, B.J.P., 2012. A free plate surface and weak oceanic crust produce single-sided subduction on Earth. *Geophysical Research Letters* 39.
- Davies, G.F., 1977. Viscous mantle flow under moving lithospheric plates and under subduction zones. *Geophysical Journal International* 49, 557–563.
- DePaolo, D.J., 2006. Isotopic effects in fracture-dominated reactive fluid–rock systems. *Geochimica et Cosmochimica Acta* 70, 1077–1096. <https://doi.org/10.1016/j.gca.2005.11.022>
- Deschamps, F., Godard, M., Guillot, S., Hattori, K., 2013. Geochemistry of subduction zone serpentinites: A review. *Lithos* 178, 96–127.
- Dewey, J.F., 1976. Ophiolite obduction. *Tectonophysics* 31, 93–120.
- Dewey, J.F., Casey, J.F., 2013. The sole of an ophiolite: the Ordovician Bay of Islands Complex, Newfoundland. *Journal of the Geological Society* 170, 715–722.
- Dijkstra, A.H., Drury, M.R., Vissers, R.L., Newman, J., 2002. On the role of melt-rock reaction in mantle shear zone formation in the Othris Peridotite Massif (Greece). *Journal of Structural Geology* 24, 1431–1450.
- Dilek, Y., Furnes, H., 2014. Ophiolites and their origins. *Elements* 10, 93–100.
- Dilek, Y., Furnes, H., Shallo, M., 2007. Suprasubduction zone ophiolite formation along the periphery of Mesozoic Gondwana. *Gondwana Research* 11, 433–475.
- Dilek, Y., Polat, A., 2008. Suprasubduction zone ophiolites and Archean tectonics. *Geology* 36, 431–432.
- Dubacq, B., Soret, M., Jewison, E., Agard, P., 2019. Early subduction dynamics recorded by the metamorphic sole of the Mt. Albert ophiolitic complex (Gaspé, Quebec). *Lithos* 334, 161–179.
- Duretz, T., Agard, P., Yamato, P., Ducassou, C., Brov, E.B., Gerya, T.V., 2016. Thermo-mechanical modeling of the obduction process based on the Oman ophiolite case. *Gondwana Research* 32, 1–10.
- Dymkova, D., Gerya, T., 2013. Porous fluid flow enables oceanic subduction initiation on Earth. *Geophysical Research Letters* 40, 5671–5676.
- England, P., Wilkins, C., 2004. A simple analytical approximation to the temperature structure in subduction zones. *Geophysical Journal International* 159, 1138–1154.
- England, P.C., Katz, R.F., 2010. Melting above the anhydrous solidus controls the location of volcanic arcs. *Nature* 467, 700.
- Ernst, W.G., 2001. Subduction, ultrahigh-pressure metamorphism, and regurgitation of buoyant crustal slices—implications for arcs and continental growth. *Physics of the Earth and Planetary Interiors* 127, 253–275.
- Ernst, W.G., Liu, J., 1998. Experimental phase-equilibrium study of Al- and Ti-contents of calcic amphibole in MORB—A semiquantitative thermobarometer. *American mineralogist* 83, 952–969.
- Faccenna, M., 2014. Water in the slab: A trilogy. *Tectonophysics* 614, 1–30. <https://doi.org/10.1016/j.tecto.2013.12.020>
- Faccenna, C., Giardini, D., Davy, P., Argentieri, A., 1999. Initiation of subduction at Atlantic-type margins: Insights from laboratory experiments. *Journal of Geophysical Research: Solid Earth* 104, 2749–2766.
- Fagereng, A., 2011. Geology of the seismogenic subduction thrust interface, in: Fagereng, A., Toy, V.G., Rowland, J.V. (Eds.), *Geology of the Earthquake Source: A Volume in Honour of Rick Sibson*. Geological Soc Publishing House, Bath, pp. 55–76.
- Fagereng, Å., den Hartog, S.A., 2017. Subduction megathrust creep governed by pressure solution and frictional-viscous flow. *Nature Geoscience* 10, 51–57.
- Fagereng, A., Sibson, R.H., 2010. Melange rheology and seismic style. *Geology* 38, 751–754. <https://doi.org/10.1130/G30868.1>
- Ferrand, T.P., Hilairet, N., Incel, S., Deldicque, D., Labrousse, L., Gasc, J., Renner, J., Wang, Y., Green II, H.W., Schubnel, A., 2017. Dehydration-driven stress transfer triggers intermediate-depth earthquakes. *Nature communications* 8, 1–11.
- Gao, X., Wang, K., 2017. Rheological separation of the megathrust seismogenic zone and episodic tremor and slip. *Nature* 543, 416.

- Gerya, T., Stern, R.J., Baes, M., Sobolev, S., Whattam, S., 2015. Plume-induced subduction initiation triggered Plate Tectonics on Earth. *Nature* 527, 221–225.
- Gerya, T.V., Stöckhert, B., Perchuk, A.L., 2018. Exhumation of high-pressure metamorphic rocks in a subduction channel: A numerical simulation. *Tectonics* 21, 6-1-6–19. <https://doi.org/10.1029/2002TC001406>
- Gnos, E., 1998. Peak metamorphic conditions of garnet amphibolites beneath the Semail Ophiolite: Implications for an inverted pressure gradient. *Int. Geol. Rev.* 40, 281–304. <https://doi.org/10.1080/00206819809465210>
- Goffé, B., Michard, A., Kienast, J.R., Le Mer, O., 1988. A case of obduction-related high-pressure, low-temperature metamorphism in upper crustal nappes, Arabian continental margin, Oman: PT paths and kinematic interpretation. *Tectonophysics* 151, 363–386.
- Gratier, J.-P., Dysthe, D.K., Renard, F., 2013. Chapter 2 - The Role of Pressure Solution Creep in the Ductility of the Earth's Upper Crust, in: Dmowska, R. (Ed.), *Advances in Geophysics, Advances in Geophysics*. Elsevier, pp. 47–179. <https://doi.org/10.1016/B978-0-12-380940-7.00002-0>
- Guillot, S., Hattori, K., Agard, P., Schwartz, S., Vidal, O., 2009. Exhumation Processes in Oceanic and Continental Subduction Contexts: A Review, in: Lallemand, S., Funicello, F. (Eds.), *Subduction Zone Geodynamics*. Springer-Verlag Berlin, Berlin, pp. 175–+.
- Guillot, S., Schwartz, S., Reynard, B., Agard, P., Prigent, C., 2015. Tectonic significance of serpentinites. *Tectonophysics* 646, 1–19. <https://doi.org/10.1016/j.tecto.2015.01.020>
- Guilmette, C., Hébert, R., Wang, C., Villeneuve, M., 2009. Geochemistry and geochronology of the metamorphic sole underlying the Xigaze ophiolite, Yarlung Zangbo Suture Zone, south Tibet. *Lithos* 112, 149–162.
- Guilmette, C., Hébert, R., Dostal, J., Indares, A., Ullrich, T., Bernard, E., Wang, C., 2012. Discovery of a dismembered metamorphic sole in the Saga ophiolite melange, South Tibet: Assessing an Early Cretaceous disruption of the Neo-Tethyan supra-subduction zone and consequences on basin closing. *Gondwana Res.* 22, 398–414. <http://dx.doi.org/10.1016/j.gr.2011.10.012>
- Guilmette, C., Smit, M.A., van Hinsbergen, D.J., Gürer, D., Corfu, F., Charette, B., Maffione, M., Rabeau, O., Savard, D., 2018. Forced subduction initiation recorded in the sole and crust of the Semail Ophiolite of Oman. *Nature Geoscience* 11, 688–695.
- Gurnis, M., Hall, C., Lavier, L., 2004. Evolving force balance during incipient subduction. *Geochemistry, Geophysics, Geosystems* 5.
- Gurnis, M., Van Avendonk, H., Gulick, S.P., Stock, J., Sutherland, R., Hightower, E., Shuck, B., Patel, J., Williams, E., Kardell, D., 2019. Incipient subduction at the contact with stretched continental crust: The Puysegur trench. *Earth and Planetary Science Letters* 520, 212–219.
- Haase, K.M., Freund, S., Koepke, J., Hauff, F., Erdmann, M., 2015. Melts of sediments in the mantle wedge of the Oman ophiolite. *Geology* 43, 275–278.
- Hacker, B.R., Mosenfelder, J.L., 1990. Metamorphism and deformation along the emplacement thrust of the Semail ophiolite, Oman. *Earth and Planetary Science Letters* 144, 435–451.
- Hacker, B.R., Mosenfelder, J.L., Ghos, E., 1996. Rapid emplacement of the Oman ophiolite: Thermal and geochronologic constraints. *Tectonics* 15, 1230–1247.
- Hacker, B.R., Peacock, S.M., Ehlers, G.A., Holloway, S.D., 2003. Subduction factory 2. Are intermediate-depth earthquakes in subducting slabs linked to metamorphic dehydration reactions? *Journal of Geophysical Research: Solid Earth* 108.
- Harper, G.D., Saleeby, J.B., Heizler, M., 1994. Formation and emplacement of the Josephine ophiolite and the Nevadan orogeny in the Klamath Mountains, California- Oregon: U/Pb zircon and ⁴⁰Ar/³⁹Ar geochronology. *Journal of Geophysical Research: Solid Earth* 99, 4293–4321.
- Harris, R.A., 1998. Origin and tectonic evolution of the metamorphic sole beneath the Brooks Range ophiolite, Alaska. *Special Papers-Geological Society Of America* 293–312.
- Hébert, R., Bezard, R., Guilmette, C., Dostal, J., Wang, C., Liu, Z., 2012. The Indus–Yarlung Zangbo ophiolites from Nanga Parbat to Namche Barwa syntaxes, southern Tibet: First synthesis of petrology, geochemistry, and geochronology with incidences on geodynamic reconstructions of Neo-Tethys. *Gondwana Research* 22, 377–397.
- Herwegh, M., Linckens, J., Ebert, A., Berger, A., Brodhag, S.H., 2011. The role of second phases for controlling microstructural evolution in polymineralic rocks: A review. *Journal of Structural Geology* 33, 1728–1750.
- Hidas, K., Tommasi, A., Garrido, C.J., Padrón-Navarta, J.A., Mainprice, D., Vauchez, A., Barou, F., Marchesi, C., 2016. Fluid-assisted strain localization in the shallow subcontinental lithospheric mantle. *Lithos* 262, 636–650.
- Hilaret, N., Reynard, B., Wang, Y., Daniel, I., Merkel, S., Nishiyama, N., Petitgirard, S., 2007. High-Pressure Creep of Serpentine, Interseismic Deformation, and Initiation of Subduction. *Science* 318, 1910–1913. <https://doi.org/10.1126/science.1148494>

- Hyndman, R.D., Peacock, S.M., 2003. Serpentinization of the forearc mantle. *Earth and Planetary Science Letters* 212, 417–432. [https://doi.org/10.1016/S0012-821X\(03\)00263-2](https://doi.org/10.1016/S0012-821X(03)00263-2)
- Ishikawa, T., Fujisawa, S., Nagaishi, K., Masuda, T., 2005. Trace element characteristics of the fluid liberated from amphibolite-facies slab: Inference from the metamorphic sole beneath the Oman ophiolite and implication for boninite genesis. *Earth and Planetary Science Letters* 240, 355–377.
- Ishizuka, O., Tani, K., Reagan, M.K., Kanayama, K., Umino, S., Harigane, Y., Sakamoto, I., Miyajima, Y., Yuasa, M., Dunkley, D.J., 2011. The timescales of subduction initiation and subsequent evolution of an oceanic island arc. *Earth and Planetary Science Letters* 306, 229–240.
- Ishizuka, O., Tani, K., Reagan, M.K., 2014. Izu-Bonin-Mariana forearc crust as a modern ophiolite analogue. *Elements* 10, 115–120.
- Ishizuka, O., Taylor, R.N., Umino, S., Kanayama, K., 2020. Geochemical evolution of arc and slab following subduction initiation: a record from the Bonin Islands, Japan. *Journal of Petrology*.
- Jamieson, R., 1986. P-T Paths from High-Temperature Shear Zones Beneath Ophiolites. *J. Metamorph. Geol.* 4, 3–22. <https://doi.org/10.1111/j.1525-1314.1986.tb00335.x>
- Jamieson, R., 1981. Metamorphism During Ophiolite Emplacement - the Petrology of the St-Anthony Complex. *J. Petrol.* 22, 397–449. <https://doi.org/10.1093/petrology/22.3.397>
- Jamieson, R.A., 1986. P- T paths from high temperature shear zone beneath ophiolites. *Journal of Metamorphic Geology* 4, 3–22.
- Jamieson, R.A., 1981. Metamorphism during ophiolite emplacement and petrology of the St. Anthony Complex. *Journal of Petrology* 22, 397–449.
- Jamieson, R.A., 1980. Formation of metamorphic aureoles beneath ophiolites—evidence from the St. Anthony Complex, Newfoundland. *Geology* 8, 150–154.
- Jamieson, R.A., Strong, D.F., 1981. A metasomatic mylonite zone within the ophiolite aureole, St. Anthony Complex, Newfoundland. *American Journal of Science* 281, 264–281.
- John, T., Medvedev, S., Rüpke, L.H., Andersen, T.B., Poddubnikov, Y.Y., Austrheim, H., 2009. Generation of intermediate-depth earthquakes by self-localizing thermal runaway. *Nature Geoscience* 2, 137–140.
- Jolivet, L., Faccenna, C., Agard, P., Frizon de Lamotte, D., Menant, A., Sternai, P., Guillocheau, F., 2016. Neo-Tethys geodynamics and mantle convection: from extension to compression in Africa and a conceptual model for obduction. *Canadian journal of earth sciences* 53, 1190–1204.
- Jones, G., Robertson, A.H.F., Cann, J.R., 1991. Genesis and emplacement of the supra-subduction zone Pindos ophiolite, northwestern Greece, in: *Ophiolite Genesis and Evolution of the Oceanic Lithosphere*. Springer, pp. 771–799.
- Jung, H., Katayama, I., Jiang, Z., Hiraga, T., Karato, S.-I., 2006. Effect of water and stress on the lattice-preferred orientation of olivine. *Tectonophysics* 421, 1–22.
- Kelemen, P.B., Manning, C.E., 2015. Reevaluating carbon fluxes in subduction zones, what goes down, mostly comes up. *Proceedings of the National Academy of Sciences* 112, E3997–E4006.
- Kelemen, P.B., Rilling, J.L., Palmerier, E.M., Mehl, L., Hacker, B.R., 2003. Thermal structure due to solid-state flow in the mantle wedge beneath arcs. *Geophysical Monograph-American Geophysical Union* 138, 293–311.
- Kelemen, P.B., Shimizu, N., Salters, V.J., 1995. Extraction of mid-ocean-ridge basalt from the upwelling mantle by focused flow of melt in dunite channels. *Nature* 375, 747–753.
- Khedr, M.Z., Arai, S., Python, M., 2013. Petrology and chemistry of basal lherzolites above the metamorphic sole from Wadi Sarami central Oman ophiolite. *Journal of Mineralogical and Petrological Sciences* 121026.
- Lallemand, S., Heuret, A., Boutelier, D., 2005. On the relationships between slab dip, back-arc stress, upper plate absolute motion, and crustal nature in subduction zones. *Geochemistry, Geophysics, Geosystems* 6.
- Le Mée, L., Girardeau, J., Monnier, C., 2004. Mantle segmentation along the Oman ophiolite fossil mid-ocean ridge. *Nature* 432, 167–172.
- Linckens, J., Bruijn, R.H., Skemer, P., 2014. Dynamic recrystallization and phase mixing in experimentally deformed peridotite. *Earth and Planetary Science Letters* 388, 134–142.
- Linckens, J., Herwegh, M., Müntener, O., 2011. Linking temperature estimates and microstructures in deformed polymineralic mantle rocks. *Geochemistry, geophysics, geosystems* 12.
- Locatelli, M., Verlaquet, A., Agard, P., Federico, L., Angiboust, S., 2018. Intermediate-depth brecciation along the subduction plate interface (Monviso eclogite, W. Alps). *Lithos* 320, 378–402.
- MacGregor, I.D., Basu, A.R., 1979. Petrogenesis of the Mount Albert ultramafic massif, Quebec. *Geological Society of America Bulletin* 90, 1529–1627.

- MacLeod, C.J., Johan Lissenberg, C., Bibby, L.E., 2013. "Moist MORB" axial magmatism in the Oman ophiolite: The evidence against a mid-ocean ridge origin. *Geology* 41, 459–462.
- Maffione, M., Thieulot, C., Van Hinsbergen, D.J., Morris, A., Plümpner, O., Spakman, W., 2015. Dynamics of intraoceanic subduction initiation: 1. Oceanic detachment fault inversion and the formation of supra- subduction zone ophiolites. *Geochemistry, Geophysics, Geosystems* 16, 1753–1770.
- Malpas, J., 1979. The dynamothermal aureole of the Bay of Islands ophiolite suite. *Canadian Journal of Earth Sciences* 16, 2086–2101.
- Mansard, N., Stünitz, H., Raimbourg, H., Précigout, J., 2020. The role of deformation-reaction interactions to localize strain in polymineralic rocks: Insights from experimentally deformed plagioclase-pyroxene assemblages. *Journal of Structural Geology* 134, 104008.
- Marschall, H.R., Schumacher, J.C., 2012. Arc magmas sourced from melange diapirs in subduction zones. *Nat. Geosci.* 5, 862–867. <https://doi.org/10.1038/NGEO1634>
- Marschall, H.R., Wanless, V.D., Shimizu, N., von Strandmann, P.A.P., Elliott, T., Monteleone, B.D., 2017. The boron and lithium isotopic composition of mid-ocean ridge basalts and the mantle. *Geochimica et Cosmochimica Acta* 207, 102–138.
- Marti, S., Stünitz, H., Heilbronner, R., Plümpner, O., Drury, M., 2017. Experimental investigation of the brittle-viscous transition in mafic rocks—Interplay between fracturing, reaction, and viscous deformation. *Journal of Structural Geology* 105, 62–79.
- Marti, S., Stünitz, H., Heilbronner, R., Plümpner, O., Kilian, R., 2018. Syn-kinematic hydration reactions, grain size reduction, and dissolution–precipitation creep in experimentally deformed plagioclase–pyroxene mixtures. *Solid Earth* 9, 985–1009. <https://doi.org/10.5194/se-9-985-2018>
- Martinez, F., Stern, R.J., Kelley, K.A., Ohara, Y., Sleeper, J.D., Ribeiro, J.M., Brounce, M., 2018. Diffuse extension of the southern Mariana margin. *Journal of Geophysical Research: Solid Earth* 123, 892–916.
- Massonne, H.-J., Opitz, J., Theye, T., Nasir, S., 2013. Evolution of a very deeply subducted metasediment from As Sifah, northeastern coast of Oman. *Lithos* 156, 171–185.
- Matthews, K.J., Seton, M., Müller, R.D., 2012. A global-scale plate reorganization event at 105–100 Ma. *Earth and Planetary Science Letters* 335, 283–298.
- McCaig, A., 1983. P-T Conditions During Emplacement of the Bay-of-Islands Ophiolite Complex. *Earth Planet. Sci. Lett.* 63, 459–473. [https://doi.org/10.1016/0012-821X\(83\)90118-8](https://doi.org/10.1016/0012-821X(83)90118-8)
- McCaig, A.M., 1983. P–T conditions during emplacement of the Bay of Islands ophiolite complex. *Earth and Planetary Science Letters* 63, 459–473.
- McDonough, W.F., Sun, S.-S., 1995. The composition of the Earth. *Chemical geology* 120, 223–253.
- Mehl, L., Hacker, B.R., Hirth, G., Kelemar, F.B., 2003. Arc-parallel flow within the mantle wedge: Evidence from the accreted Fairweather arc, south central Alaska. *Journal of Geophysical Research: Solid Earth* 108.
- Métois, M., Vigny, C., Socquet, A., 2016. Interseismic coupling, megathrust earthquakes and seismic swarms along the Chilean subduction zone (38–18 S). *Pure and Applied Geophysics* 173, 1431–1449.
- Michibayashi, K., Ohara, Y., Stern, R.J., Fryer, P., Kimura, J.-I., Tasaka, M., Harigane, Y., Ishii, T., 2009. Peridotites from a ductile shear zone within back-arc lithospheric mantle, southern Mariana Trench: Results of a Shinkai 6500 dive. *Geochemistry, Geophysics, Geosystems* 10.
- Moghadam, H.S., Stern, R.J., 2015. Ophiolites of Iran: Keys to understanding the tectonic evolution of SW Asia (II) Mesozoic ophiolites. *Journal of Asian Earth Sciences* 100, 31–59.
- Monie, P., Agard, P., 2009. Coeval blueschist exhumation along thousands of kilometers: Implications for subduction channel processes. *Geochemistry, Geophysics, Geosystems* 10.
- Moore, E.M., 2002. Pre-1 Ga (pre-Rodinian) ophiolites: Their tectonic and environmental implications. *Geological Society of America Bulletin* 114, 80–95.
- Moore, E.M., 1982. Origin and emplacement of ophiolites. *Reviews of Geophysics* 20, 735–760.
- Moreno, M., Melnick, D., Rosenau, M., Bolte, J., Klotz, J., Echtler, H., Baez, J., Bataille, K., Chen, J., Bevis, M., Hase, H., Oncken, O., 2011. Heterogeneous plate locking in the South-Central Chile subduction zone: Building up the next great earthquake. *Earth Planet. Sci. Lett.* 305, 413–424. <https://doi.org/10.1016/j.epsl.2011.03.025>
- Nicolas, A., 1989. Structures of ophiolites and dynamics of oceanic lithosphere. *Structures of ophiolites and dynamics of oceanic lithosphere*.
- Nicolas, A., Boudier, F., Ildefonse, B., Ball, E., 2000. Accretion of Oman and United Arab Emirates ophiolite—discussion of a new structural map. *Marine Geophysical Researches* 21, 147–180.
- Nicolas, A., Le Pichon, X., 1980. Thrusting of young lithosphere in subduction zones with special reference to structures in ophiolitic peridotites. *Earth and Planetary Science Letters* 46, 397–406.

- Nielsen, S.G., Marschall, H.R., 2017. Geochemical evidence for melange melting in global arcs. *Sci. Adv.* 3, UNSP e1602402. <https://doi.org/10.1126/sciadv.1602402>
- Oleskevich, D.A., Hyndman, R.D., Wang, K., 1999. The updip and downdip limits to great subduction earthquakes: Thermal and structural models of Cascadia, south Alaska, SW Japan, and Chile. *Journal of Geophysical Research: Solid Earth* 104, 14965–14991.
- Osei Tutu, A., Steinberger, B., Sobolev, S.V., Rogozhina, I., Popov, A.A., 2018. Effects of upper mantle heterogeneities on the lithospheric stress field and dynamic topography. *Solid Earth* 9, 649–668.
- Panet, I., Bonvalot, S., Narteau, C., Remy, D., Lemoine, J.-M., 2018. Migrating pattern of deformation prior to the Tohoku-Oki earthquake revealed by GRACE data. *Nature Geoscience* 11, 367.
- Parlak, O., Dunkl, I., Karaođlan, F., Kusky, T.M., Zhang, C., Wang, L., Koepke, J., Billor, Z., Hames, W.E., Őimőek, E., 2019. Rapid cooling history of a Neotethyan ophiolite: Evidence for contemporaneous subduction initiation and metamorphic sole formation. *Bulletin* 131, 2011–2038.
- Patriat, M., Falloon, T., Danyushevsky, L., Collot, J., Jean, M.M., Hoernle, K., Hauff, F., Maas, R., Woodhead, J.D., Feig, S.T., 2019. Subduction initiation terranes exposed at the front of a 2 Ma volcanically-active subduction zone. *Earth and Planetary Science Letters* 508, 30–40.
- Paulatto, M., Laigle, M., Galve, A., Charvis, P., Sapin, M., Bayrakci, G., Evain, M., Kopp, H., 2017. Dehydration of subducting slow-spread oceanic lithosphere in the Lesser Antilles. *Nature Communications* 8, 15980. <https://doi.org/10.1038/ncomms15980>
- Peacock, S.M., 1996. Thermal and petrologic structure of subduction zones. *Subduction: top to bottom* 96, 119–133.
- Peacock, S.M., Hyndman, R.D., 1999. Hydrous minerals in the mantle wedge and the maximum depth of subduction thrust earthquakes. *Geophysical Research Letters* 26, 2517–2520.
- Pearce, J.A., Alabaster, T., Shelton, A.W., Searle, M.P., 1981. The Oman ophiolite as a Cretaceous arc-basin complex: evidence and implications. *Philosophical Transactions of the Royal Society of London. Series A, Mathematical and Physical Sciences* 300, 299–317.
- Platt, J.P., 2015. Rheology of two-phase systems: A microphysical and observational approach. *Journal of Structural Geology* 77, 213–227. <https://doi.org/10.1016/j.jsg.2015.05.003>
- Plunder, A., Agard, P., Chopin, C., Pourceau, A., Cay, A.I., 2015. Accretion, underplating and exhumation along a subduction interface: from subduction initiation to continental subduction (Taőanlı zone, W. Turkey). *Lithos* 220, 233–254.
- Plunder, A., Agard, P., Chopin, C., Soret, M., Okay, A.I., Whitechurch, H., 2016. Metamorphic sole formation, emplacement and blueschist facies overprint: early subduction dynamics witnessed by western Turkey ophiolites. *Trans. Nova* 28, 329–339. <https://doi.org/10.1111/ter.12225>
- Poli, S., Schmidt, M.W., 2002. Petrology of subducted slabs. *Annual Review of Earth and Planetary Sciences* 30, 207–235.
- Pourceau, A., Scherer, E.E., Schorn, S., Bast, R., Schmidt, A., Ebert, L., 2019. Thermal evolution of an ancient subduction interface revealed by Lu–Hf garnet geochronology, Halilbađı Complex (Anatolia). *Geoscience Frontiers* 10, 127–148.
- Précigout, J., Prigent, C., Palacas, L., Pochon, A., 2017. Water pumping in mantle shear zones. *Nature communications* 8, 1–10.
- Précigout, J., Stünitz, H., 2016. Evidence of phase nucleation during olivine diffusion creep: A new perspective for mantle strain localisation. *Earth and Planetary Science Letters* 455, 94–105.
- Prigent, Cécile, Agard, P., Guillot, S., Godard, M., Dubacq, B., 2018a. Mantle Wedge (De) formation During Subduction Infancy: Evidence from the Base of the Semail Ophiolitic Mantle. *Journal of Petrology* 59, 2061–2092.
- Prigent, C., Guillot, S., Agard, P., Lemarchand, D., Soret, M., Ulrich, M., 2018b. Transfer of subduction fluids into the deforming mantle wedge during nascent subduction: Evidence from trace elements and boron isotopes (Semail ophiolite, Oman). *Earth and Planetary Science Letters* 484, 213–228. <https://doi.org/10.1016/j.epsl.2017.12.008>
- Prigent, C., Guillot, S., Agard, P., Ildefonse, B., 2018c. Fluid-Assisted Deformation and Strain Localization in the Cooling Mantle Wedge of a Young Subduction Zone (Semail Ophiolite). *Journal of Geophysical Research: Solid Earth* 123, 7529–7549. <https://doi.org/10.1029/2018JB015492>
- Qian, Q., Hermann, J., Dong, F., Lin, L., Sun, B., 2020. Episodic formation of Neotethyan ophiolites (Tibetan plateau): Snapshots of abrupt global plate reorganizations during major episodes of supercontinent breakup? *Earth-science reviews* 103144.
- Reagan, M.K., Ishizuka, O., Stern, R.J., Kelley, K.A., Ohara, Y., Blichert-Toft, J., Bloomer, S.H., Cash, J., Fryer, P., Hanan, B.B., 2010. Fore-arc basalts and subduction initiation in the Izu-Bonin-Mariana system. *Geochemistry, Geophysics, Geosystems* 11.

- Reagan, M.K., Heaton, D.E., Schmitz, M.D., Pearce, J.A., Shervais, J.W., Koppers, A.A., 2019. Forearc ages reveal extensive short-lived and rapid seafloor spreading following subduction initiation. *Earth and Planetary Science Letters* 506, 520–529.
- Regenauer-Lieb, K., Yuen, D.A., Branlund, J., 2001. The initiation of subduction: criticality by addition of water? *Science* 294, 578–580.
- Reynard, B., 2013. Serpentine in active subduction zones. *Lithos, Serpentinites from mid-oceanic ridges to subduction* 178, 171–185. <https://doi.org/10.1016/j.lithos.2012.10.012>
- Rioux, M., Bowring, S., Kelemen, P., Gordon, S., Dudás, F., Miller, R., 2012. Rapid crustal accretion and magma assimilation in the Oman- UAE ophiolite: High precision U- Pb zircon geochronology of the gabbroic crust. *Journal of Geophysical Research: Solid Earth* 117.
- Rioux, M., Garber, J., Bauer, A., Bowring, S., Searle, M., Kelemen, P., Hacker, B., 2016. Synchronous formation of the metamorphic sole and igneous crust of the Semail ophiolite: New constraints on the tectonic evolution during ophiolite formation from high-precision U–Pb zircon geochronology. *Earth and Planetary Science Letters* 451, 185–195.
- Roberts, N.M., Thomas, R.J., Jacobs, J., 2016. Geochronological constraints on the metamorphic sole of the Semail ophiolite in the United Arab Emirates. *Geoscience Frontiers* 7, 609–619.
- Rogers, G., Dragert, H., 2003. Episodic tremor and slip on the Cascadia subduction zone: The chatter of silent slip. *Science* 300, 1942–1943.
- Rowe, C.D., Moore, J.C., Remitti, F., 2013. The thickness of subduction plate boundary faults from the seafloor into the seismogenic zone. *Geology* 41, 991–994. <https://doi.org/10.1130/G34556.1>
- Sandiford, D., Moresi, L., 2019. Improving subduction interface implementation in dynamic numerical models. *Solid Earth* 10, 969–985.
- Schaeffer, A.J., Lebedev, S., 2013. Global shear speed structure of the upper mantle and transition zone. *Geophysical Journal International* 194, 417–448.
- Searle, M., Cox, J., 1999. Tectonic setting, origin, and obduction of the Oman ophiolite. *Geological Society of America Bulletin* 111, 104–122.
- Searle, M.P., Cox, J.O.N., 2002. Subduction zone metamorphism during formation and emplacement of the Semail ophiolite in the Oman Mountains. *Geological Magazine* 139, 241–255.
- Searle, M.P., Malpas, J., 1980. Structure and metamorphism of rocks beneath the Semail ophiolite of Oman and their significance in ophiolite obduction. *Earth and Environmental Science Transactions of the Royal Society of Edinburgh* 71, 247–262.
- Searle, M.P., Warren, C.J., Waters, D.J., Parrish, R.R., 2004. Structural evolution, metamorphism and restoration of the Arabian continental margin, Saih Hatat region, Oman Mountains. *Journal of Structural Geology* 26, 451–473.
- Seyler, C., Getsinger, A., Hirth, G., Robertson, K., 2015. Relating Amphibole Abundance to the Rheology of the Lower Crust, in: *AGU Fall Meeting Abstracts*.
- Shervais, J.W., 2001. Birth, death, and resurrection: The life cycle of suprasubduction zone ophiolites. *Geochemistry, Geophysics, Geosystems* 2.
- Shillington, D.J., Bécel, A., Nedimović, M.R., Kuehn, H., Webb, S.C., Abers, G.A., Keranen, K.M., Li, J., Delescluse, M., Matter Saucrup, G.A., 2015. Link between plate fabric, hydration and subduction zone seismicity in Alaska. *Nature Geoscience* 8, 961–964.
- Sizova, E., Gerya, T., Brown, M., Perchuk, L.L., 2010. Subduction styles in the Precambrian: Insight from numerical experiments. *Lithos* 116, 209–229.
- Smart, C.M., Wakabayashi, I., 2009. Hot and deep: Rock record of subduction initiation and exhumation of high-temperature, high-pressure metamorphic rocks, Feather River ultramafic belt, California. *Lithos* 113, 292–305.
- Soret, M., Agard, P., Dubacq, B., Plunder, A., Yamato, P., 2017. Petrological evidence for stepwise accretion of metamorphic soles during subduction infancy (Semail ophiolite, Oman and UAE). *Journal of Metamorphic Geology* 35, 1051–1080. <https://doi.org/10.1111/jmg.12267>
- Soret, M., Agard, P., Dubacq, B., Vitale-Brovarone, A., Monie, P., Chauvet, A., Whitechurch, H., Villemant, B., 2016. Strain localization and fluid infiltration in the mantle wedge during subduction initiation: Evidence from the base of the New Caledonia ophiolite. *Lithos* 244, 1–19.
- Soret, M., Agard, P., Ildefonse, B., Dubacq, B., Prigent, C., Rosenberg, C., 2019. Deformation mechanisms in mafic amphibolites and granulites: record from the Semail metamorphic sole during subduction infancy. *Solid Earth Discussions* 2019, 1–36. <https://doi.org/10.5194/se-2019-28>
- Spandler, C., Pirard, C., 2013. Element recycling from subducting slabs to arc crust: A review. *Lithos* 170, 208–223.
- Spencer, C.J., Cavosie, A.J., Raub, T.D., Rollinson, H., Jeon, H., Searle, M.P., Miller, J.A., McDonald, B.J., Evans, N.J., 2017. Evidence for melting mud in Earth's mantle from extreme oxygen isotope signatures in zircon. *Geology* 45, 975–978.

- Spray, J.G., 1984. Possible causes and consequences of upper mantle decoupling and ophiolite displacement. Geological Society, London, Special Publications 13, 255–268.
- Stern, R.J., Bloomer, S.H., 1992. Subduction zone infancy: examples from the Eocene Izu-Bonin-Mariana and Jurassic California arcs. Geological Society of America Bulletin 104, 1621–1636.
- Stern, R.J., Gerya, T., 2018. Subduction initiation in nature and models: A review. Tectonophysics 746, 173–198.
- Suhr, G., 1993. Evaluation of upper mantle microstructures in the Table Mountain massif (Bay of Islands ophiolite). Journal of Structural Geology 15, 1273–1292.
- Suhr, G., Batanova, V., 1998. Basal iherzolites in the Bay of Islands Ophiolite: Origin by detachment-related telescoping of a ridge-parallel melting gradient. TERRA NOVA-OXFORD- 10, 1–5.
- Suhr, G., Cawood, P.A., 1993. Structural history of ophiolite obduction, Bay of Islands, Newfoundland. Geological Society of America Bulletin 105, 399–410.
- Syracuse, E.M., van Keken, P.E., Abers, G.A., 2010. The global range of subduction zone thermal models. Physics of the Earth and Planetary Interiors, Special Issue on Deep Slab and Mantle Dynamics 183, 73–90. <https://doi.org/10.1016/j.pepi.2010.02.004>
- Takazawa, E., Okayasu, T., Satoh, K., 2003. Geochemistry and origin of the basal Iherzolites from the northern Oman ophiolite (northern Fizh block). Geochemistry, Geophysics, Geosystems 4.
- Tamblyn, R., Zack, T., Schmitt, A.K., Hand, M., Kelsey, D., Morrissey, L., Pabst, S., Savov, I.P., 2019. Blueschist from the Mariana forearc records long-lived residence of material in the subduction channel. Earth and Planetary Science Letters 519, 171–181.
- Tommasi, A., Vauchez, A., Godard, M., Belley, F., 2006. Deformation and melt transport in a highly depleted peridotite massif from the Canadian Cordillera: implications to seismic anisotropy above subduction zones. Earth and Planetary Science Letters 252, 245–259.
- Toth, J., Gurnis, M., 1998. Dynamics of subduction initiation at preexisting fault zones. Journal of Geophysical Research: Solid Earth 103, 18053–18067.
- van Hinsbergen, D.J., Maffione, M., Koornneef, L.M., Guilmette, C., 2019. Kinematic and paleomagnetic restoration of the Semail ophiolite (Oman) reveals subduction initiation along an ancient Neotethyan fracture zone. Earth and Planetary Science Letters 518, 183–196.
- van Hinsbergen, D.J.J., Peters, K., Maffione, M., Spakman, W., Guilmette, C., Thieulot, C., Plumper, O., Gurer, D., Brouwer, F.M., Aldanmaz, E., Kaymakci, N., 2015. Dynamics of intraoceanic subduction initiation: 2. Suprasubduction zone ophiolite formation and metamorphic sole exhumation in context of absolute plate motions. Geochem. Geophys. Geosyst. 16, 1771–1785. <https://doi.org/10.1002/2015GC005745>
- Van Hunen, J., Moyen, J.-F., 2012. Archean subduction: fact or fiction? Annual Review of Earth and Planetary Sciences 40, 195–219.
- van Keken, P.E., Hacker, B.R., Syracuse E.M., Abers, G.A., 2011. Subduction factory: 4. Depth-dependent flux of H₂O from subducting slabs worldwide. Journal of Geophysical Research: Solid Earth 116.
- Vaughan, A.P., Scarrow, J.H., 2002. Ophiolite obduction pulses as a proxy indicator of superplume events? Earth and Planetary Science Letters 213, 407–416.
- Wada, I., Behn, M.D., 2015. Focusing of upward fluid migration beneath volcanic arcs: Effect of mineral grain size variation in the mantle wedge. Geochemistry, Geophysics, Geosystems 16, 3905–3923.
- Wada, I., Wang, K., 2009. Common depth of slab-mantle decoupling: Reconciling diversity and uniformity of subduction zones. Geochemistry, Geophysics, Geosystems 10.
- Wada, I., Wang, K., He, J., Hyndman, R.D., 2008. Weakening of the subduction interface and its effects on surface heat flow, slab dehydration, and mantle wedge serpentinization. Journal of Geophysical Research: Solid Earth 113.
- Wakabayashi, J., 1990. Counterclockwise P-T-T Paths from Amphibolites, Franciscan Complex, California - Relics from the Early Stages of Subduction Zone Metamorphism. J. Geol. 98, 657–680. <https://doi.org/10.1086/629432>
- Wakabayashi, J., Dilek, Y., 2003. Ophiolites in Earth history, Geological Society of London Special Publication 218.
- Wakabayashi, J., Dilek, Y., 2000. Spatial and temporal relationships between ophiolites and their metamorphic soles: A test of models of forearc ophiolite genesis, in: Dilek, Y., Moores, E.M., Elthon, D., Nicolas, A. (Eds.), Ophiolites and Oceanic Crust: New Insights from Field Studies and Ocean Drilling Program. Geological Soc Amer Inc, Boulder, pp. 53–64.
- Wang, K., Hu, Y., He, J., 2012. Deformation cycles of subduction earthquakes in a viscoelastic Earth. Nature 484, 327.
- Warren, C.J., Parrish, R.R., Waters, D.J., Searle, M.P., 2005. Dating the geologic history of Oman's Semail ophiolite: Insights from U-Pb geochronology. Contributions to Mineralogy and Petrology 150, 403–422.

- Warren, C.J., Sherlock, S.C., Kelley, S.P., 2011. Interpreting high-pressure phengite $40\text{ Ar}/39\text{ Ar}$ laserprobe ages: an example from Saih Hatat, NE Oman. *Contributions to Mineralogy and Petrology* 161, 991–1009.
- Wassmann, S., Stoeckhert, B., 2013. Rheology of the plate interface - Dissolution precipitation creep in high pressure metamorphic rocks. *Tectonophysics* 608, 1–29.
<https://doi.org/10.1016/j.tecto.2013.09.030>
- Whattam, S.A., Stern, R.J., 2011. The 'subduction initiation rule': a key for linking ophiolites, intraoceanic forearcs, and subduction initiation. *Contributions to Mineralogy and Petrology* 162, 1031–1045.
- Williams, H., Smyth, W.R., 1973. Metamorphic aureoles beneath ophiolite suites and alpine peridotites; tectonic implications with west Newfoundland examples. *American Journal of Science* 273, 594–621.
- Yamato, P., Agard, P., Burov, E., Le Pourhiet, L., Jolivet, L., Tiberi, C., 2007a. Burial and exhumation in a subduction wedge: Mutual constraints from thermomechanical modeling and natural P-T-t data (Schistes Lustrés, western Alps). *J. Geophys. Res.-Solid Earth* 112, B07410.
<https://doi.org/10.1029/2006JB004441>
- Yamato, P., Agard, P., Goffé, B., De Andrade, V., Vidal, O., Jolivet, L., 2007b. New, high- precision P-T estimates for Oman blueschists: implications for obduction, nappe stacking and exhumation processes. *Journal of Metamorphic Geology* 25, 657–682.
- Yoshikawa, M., Python, M., Tamura, A., Arai, S., Takazawa, E., Shibata, T., Ueda, A., Sato, T., 2015. Melt extraction and metasomatism recorded in basal peridotites above the metamorphic sole of the northern Fijh massif, Oman ophiolite. *Tectonophysics* 650, 53–64.
- Zhong, S., Gurnis, M., 1995. Mantle convection with plates and mobile, faulted plate margins. *Science* 267, 838–843.
- Zhou, X., Li, Z.-H., Gerya, T.V., Stern, R.J., Xu, Z., Zhang, J., 2018. Subduction initiation dynamics along a transform fault control trench curvature and ophiolite ages. *Geology* 46, 607–610.

Figure and Table captions

Fig. 1 a) Idealized view of early subduction (after Duretz et al., 2016; compare with figure 2a): snapshot of a thermomechanical numerical experiment shortly after initiation of intraoceanic subduction (<1.5 Ma). The black dot corresponds to a tracer located in the oceanic crust, whose P–T evolution is represented by the red dashed line, and fossil equivalent is a 'metamorphic sole'. Main lithologies: mafic oceanic crust is green (dark: basalts; light: gabbros); lithospheric and asthenospheric mantle: blue and purple, respectively; continental crust is grey. For details see Duretz et al., 2016).

b) 'Analog'/cartoonish view of subduction initiation, highlighting mantle resistance to slab entrance; every ophiolite is underlain by fragments of metamorphosed oceanic crust named metamorphic soles, showing that each subduction starts by stripping some material from the downgoing nascent slab (as if the nail, here).

c) Idealized view of mature subduction (after Abers et al., 2017; see references therein). Numerical models impose decoupling down to a given coupling depth, in order to enable strain localization and slab penetration (see introduction). Shallow decoupling and deep coupling (CDVC: common depth of viscous coupling, Wada and Wang, 2009; D80: Syracuse et al., 2010) control subduction wedge temperature and dynamics, hence mineral reactions, fluid release and element transfer. The subducting slab crust, particularly along the plate interface, is expected to partly dehydrate as it progressively heats up. Note colors here and throughout most figures: blue (oceanic crust), olive green (mantle), faded dark green (partly serpentinized mantle).

d) Estimates of the potential amount of water released as a function of depth by lithology near the plate interface (Hacker, 2008). Unfortunately, water transfer cannot be verified or assessed by natural samples recovered from fossil subduction zones (i.e., dots here): samples cannot reliably be set back with respect to the plate interface, since the two sides were tectonically offset by later deformation. Environments where metamorphic soles are found are the only ones where both sides are still welded to each other.

e) Schematic mineralogical evolution of oceanic crust as it transforms during subduction (see Poli and Schmidt, 1996; van Keken et al., 2011; Soret et al., 2017; Hernandez-Urbe et al., 2019). Both early subduction (forming metamorphic soles) and mature subduction (forming eclogites, along warm or cold subduction) lead to the formation of relatively dry, garnet and clinopyroxene dominated assemblages. Abbreviations: Amph: amphibole; Chl: chlorite; Cpx: clinopyroxene; Ep: epidote; Grt: garnet; Lws: lawsonite; Plag: plagioclase.

Fig. 2 (De)formation of the base of ophiolites during subduction infancy. a) Simplified natural setting of intraoceanic subduction shortly after initiation (the exact locus and type of discontinuity where subduction nucleates is not specified here; see § 2.1.2 and Fig. 3a). The

close-up illustrates how, near ~30 km depth (P-T conditions of ~1 GPa and 850°C, on average), some fragments of oceanic crust resist travel to greater depths: the initial location of the plate interface (thrust 1) steps down into a weaker horizon in the slab (e.g., to thrust 2), thereby stripping a km-scale piece of crustal material.

b) Tectonic organization of the early subduction frozen-in plate interface exposed below ophiolites: at the base of the upper plate, a zone of strongly deformed mantle overlies pervasively deformed metamorphic soles.

c) Tectonic layering (banding) and P-T conditions of deformation of lowermost peridotites is concordant with that of the HT metamorphic soles.

d) A systematic organization, both in terms of P-T conditions and lithologies, is found across the former plate contact, such as a T decrease from granulite to greenschist facies downwards manifested by the presence of discrete slices (e.g., HTa, HTb), and a sedimentary-dominated section at the base for the LT sole (see text and Agard et al., 2016 for details).

Fig. 3

a) Two major types of ophiolites are commonly recognized (Wakabayashi and Dilek, 2003) based on their relationship to continental lithosphere: Tethyan ophiolites are emplaced after intraoceanic subduction by underthrusting of a nearby continental margin (e.g., Oman or Turkey), whereas Cordilleran ophiolites are accreted to the subduction forearc, be it continental (e.g., Western USA) or oceanic (e.g., Philippines sea plate for the Izu-Bonin, which may ultimately turn into an ophiolite; Stern et al., 2012). Whether subduction is induced (I) or spontaneous (S) is debated and likely depends on the exact geodynamic configuration. However, regardless of the initial setting, ophiolite emplacement onto a continental margin (i.e., 'subduction' in a strict sense) always requires a first stage of intraoceanic subduction either followed by short-lived continental subduction or only underthrusting below the future ophiolite. The dashed vertical line recalls uncertainties regarding the nature of the geological discontinuity onto which subduction nucleates, i.e. transform fault, ridge, back-arc basin or former oceanic detachment (see text for references).

f) Two end-member cases may exist for the timing of subduction initiation with respect to ophiolite formation: either subduction initiates (1) and triggers the formation of the ophiolite lithosphere (2) by mantle upwelling (case A; e.g., Guilmette et al., 2018); or subduction initiates (1) near a preexisting but buoyant, young or rejuvenated ophiolite lithosphere (0) guiding strain localization but without new ophiolite generation (case B; Hassig et al., 2016)

Fig. 4

a) Overview of the metamorphic sole \ banded peridotite pair (Sumeini, N. Oman).
 b) Typical facies of banded peridotites and massive granulite facies soles in the first few meters away from the contact. c) Granulite facies, garnet-clinopyroxene bearing amphibolite from the warmer and best preserved portion of HTa (termed peak HTa for the sake of convenience). d) Small melt veinlets in HTa. e-g) typical cm-dm-scale outcrop features of LT, HTb, and HTa, metamorphic soles for comparison. h-j) Peridotites from the base of the mantle section: (h) porphyroclastic tectonite, (i) protomylonite and (j) foliated ultramylonite. See text for details. Note grain size reduction and onset of banding, from left to right, as deformation increases.

Fig. 5 Large-scale structure and conditions of deformation.

a) General organization of the metamorphic sole \ banded peridotite juxtaposition (Fig. 2d), as seen in Sumeini (Fig. 4a). Below peridotites affected by intense mylonitic deformation, three distinct sole subunits were stacked successively, at decreasing temperatures (from top to bottom: HTa, HTb then LT). Geothermometry reveals that cumulative deformation in the adjacent peridotite, from (proto)mylonitic to ultramylonitic, occurred during cooling across the same temperature range (~900-850°C to 650°C).

b) Accretion of metamorphic soles and consequent deformation of the mantle base peridotites constrain progressive deformation along and across the early subduction interface (from stage 1a to 3). 1a: Welding of HTa to the mantle base is manifested through a >500-1000m thick zone of distributed deformation. 1b: HTb is accreted at shallower depths to the pair of partly exhumed HTa and mantle peridotites, in which more focused proto- to mylonitic deformation demonstrates that deformation is distributed across a narrower zone; 2: underthrusting of HT soles and mantle by LT metasediments, advocating for shallower downstepping of the subduction interface into the slab occurs, at ~0.5 GPa; 3: no accretion takes place any longer at the subduction interface, demonstrating effective strain localization across a narrow lubricated plate boundary.

Fig. 6 Schematic snapshots of deformation and accretion stages along the subduction interface.

a) Juxtaposition of HTa to the protomylonitic peridotites provides the first record of viscous coupling during early subduction (i.e., when mantle resistance prevents further slab progress). Mineral transformations and deformation patterns during descent and peak burial of HTa were partly erased by later deformation. Abbreviations: s: sediments, b: basalts, g: gabbros, m: mantle. Isotherms after Agard et al. (2016).

b) Accretion of HTb to the partly exhuming HTa-banded peridotite pair. Note that prograde mineral transformations and deformation mechanisms witnessed in HTb may also inform on the partly erased prograde evolution of HTa.

Fig. 7 Viscous coupling at the plate interface. a) Situation when the nascent slab first encounters resistance of the (upper plate) mantle, near 1 GPa and 850°C. Same colors as in Fig. 1c for comparison. b) Viscous coupling is dictated by the contrasting mechanical behaviour (and fluid content) of incoming materials. Experimental data and natural observations show that the slab crust is initially stronger than the shallow serpentinized mantle wedge (evolution of the slab tip until point 1). It weakens with increasing temperature (thick blue line) until it reaches a value similar to that of the drier mantle wedge (evolution 1 to 1"). Transient mechanical coupling clogs the plate interface, forcing down-stepping of the plate boundary (red thrust) and peeling off slab fragments as a result (i.e., the metamorphic soles, here HTa). For the compilation of flow laws see Agard et al. (2016). Dotted curves in a) indicate the qualitative evolution of the mantle and crust resistance along dip (Soret et al., 2019).

Fig. 8 Overview of the mineralogical, petrological and P-T evolution of HT metamorphic soles (see also Soret et al., 2017). Same abbreviations as in text (§ 2.2).

a) Summary of P-T paths followed by the different units (Soret et al., 2017; for HTa, k, s and wt: Khubakhib, Sumeini and Wadi Tayin; see also Gnos, 1998). Estimates for HTa are consistent with subordinate amount of melting (see also Fig. 5a).

b) Range of amphibole compositions in HTa and HTb. The Ti content can be regarded as a proxy for temperature (Ernst and Liu, 1998). This shows the higher T reached by HTa, and illustrates its partial retrogression in conditions experienced by HTb.

c) Thermodynamic modelling of the evolution of HTa in Sumeini places further constraints on T and P conditions (see Figs. 2 and 5a; Soret et al., 2017 for details).

d) Grt-Cpx-Amph-bearing amphibolite preserved near the contact (peak HTa), with incipient retrogression. Note the granular texture, particularly the interlocking of garnet and clinopyroxene (and compare with figures 8g and 13a).

e) More strongly retrogressed HTa, with incipient sub-horizontal secondary schistosity marked by the alignment of amphibole (and plagioclase) crystals.

f) Example of HTb (clinopyroxene-bearing, here) amphibolite with interspersed amphibole and plagioclase along a weak sub-horizontal schistosity.

g-h) Close-up views on the HTa Grt-Cpx-Amph assemblage.

i) Compositional map (Al) of the area shown in h). Note the undulose extinction of clinopyroxene (advocating for some dislocation creep) and later fracturing, dismembering edges of the large crystal. Yellow cores indicate higher P-T conditions of formation. Smaller satellite grains show evidence for mineral reequilibration during retrogression, more pronounced for the smaller grains, and further dismembering of the texture. This advocates for diffusion-enhanced, grain size sensitive dissolution-precipitation creep.

Fig. 9 Overview of the mineralogical, petrological and compositional evolution of banded peridotites (see also Prigent et al., 2018a,c). a-c) Evolution of textures as deformation, at low T for the mantle (i.e., in the range between 900-650°C), increases along with cooling. Compare with figures 4j,i,h, respectively. Note the appearance of polymineralic domains, progressive isolation of porphyroclasts and the considerable grain size reduction. d) Crystallization of a few percents of amphibole is observed, particularly in strained zones: note the modal increase of amphibole in the fine-grained schistosity located in and near the orthopyroxene porphyroclast pressure shadow (after Prigent et al., 2018c). e) Mineral dissolution of primary phases, as shown here for clinopyroxene, replaced by polymineralic domains comprising secondary olivine, spinel, clinopyroxene and amphibole (\pm orthopyroxene). f) Grain size reduction for all mineral phases as a function of increasing deformation intensity, color coded from red to yellow and white. g) Evolution of orthopyroxene compositions: new grains from polymineralic domains in mylonites contrast with porphyroclasts for major and trace elements. Note that this is observed at the base of the Semail ophiolite in all massifs, keyed by the different symbols. h) Amphibole content as a function of deformation intensity (same color coding as in f). Modal amounts of amphibole predicted for a saturated, hydrated ultramafic peridotite composition (Iherz.) are shown for 850 and 750°C (after Précigout et al., 2017).

Fig. 10 Deformation mechanisms at \sim 850°C (peak burial of HTa, coupling and detachment) in metamorphic soles (a-d) and banded peridotites (e). a) Electron back-scattered diffraction (EBSD) phase map of a relatively well preserved Grt-Cpx-bearing amphibolite sampled \sim 2.5m away from the contact with banded peridotites (after Soret et al., 2019, Fig. 4d). Note the almost equant distribution of garnet and clinopyroxene (compare with Fig. 8d). b-d) Comparison of optical, EBSD and compositional data for a representative amphibole-rich domain in HTa. b) Microphotograph of the representative texture of the domain. Note fractures and incipient strain localization marked by tiny shear bands. c) $[2-10^\circ]$ intracrystalline misorientation, with respect to the mean grain orientation, from EBSD data. Compare with the electron probe compositional map of the same area showing the Ti content of amphibole. Amphibole cores attest to HT conditions, while systematic lower Ti contents are observed in cracks and for the small later crystallized amphibole grains. Partial reequilibration of the larger grains is also conspicuous. e) EBSD phase map showing the microstructure and grain texture of a (proto)mylonite. Color coding consistent with that of a). Note the contrast in grain size between the orthopyroxene (and olivine) porphyroclasts and the polymineralic domains, outlined in part by the crystallization of secondary clinopyroxene (yellow). Incipient strain localization is marked by the development of a secondary schistosity

and small scale shear bands (left part of the image). Very small amounts of amphibole are present (indicated by blue arrows).

Fig. 11 Deformation mechanisms at $\sim 750^\circ\text{C}$ (peak burial of HTb, early exhumation for the HTa-peridotite pair) in metamorphic soles (a-d) and banded peridotites (e-g). In part after Soret et al., 2019 and Prigent et al., 2018a,c. a) EBSD phase map of HTb. b-d) Phase maps of significantly retrogressed HTa for comparison with a). Note the extensive development of the amphibole-plagioclase mineral assemblage, particularly along strain domains forming incipient shear bands (d). e) EBSD phase map of a mylonitic banded peridotite showing ultramylonitic bands. Note the extreme grain size reduction. f) Phase map of a mylonite cut across by later serpentinite veins (white). g) Amphibole-rich pressure shadows around an orthopyroxene porphyroclast.

Fig. 12 Element transfer through the interface during deformation. a) Primitive mantle-normalized (after McDonough and Sun, 1995) trace element patterns for orthopyroxene (Opx) and clinopyroxene (Cpx). Symbols are keyed to massifs along the Semail, as for figure 9f (see Prigent et al., 2018a). Filled and empty symbols refer to average compositions of porphyroclasts (Opx1, Cpx1) and matrix minerals (Opx2, Cpx2), respectively. Light grey to black fields outline compositions from other basal peridotite localities (Takazawa et al., 2003; Khedr et al., 2014; Yoshikawa et al., 2015). Vertical shaded bands refer to elements enriched in amphibolite-derived fluids (Ishikawa et al., 2005). Hz: harzburgite; Lz: lherzolite. b-c) $\delta^{11}\text{B}$ vs boron concentration in whole rock samples, as a function of the distance to the basal contact with HTa and of increasing deformation (b) or modal proportion of metasomatic amphibole (c; in % area). DM: Depleted MORB Mantle; MS: metamorphic soles (HTa). $\delta^{11}\text{B}$ value after Marschall et al. (2017). d) Modelled $\delta^{11}\text{B}$ of peridotites with increasing distance to the basal contact as a function of v/K (fluid velocity/reaction rate ratio) and for a fluid/peridotite ratio of 0.01. Grey boxes correspond to data for basal peridotites. See text (§ 3.4 for details).

Fig. 13 The metamorphic sole \ banded peridotite pair from other ophiolites. a-c) Microphotographs of HT metamorphic soles from Gapésie, Canada (see Dubacq et al., 2019). Grt-Cpx-Amp-bearing amphibolite near the contact (peak HTa), with only minimal retrogression (sub-horizontal schistosity dominantly from peak burial). Note again the granular texture and interlocking of garnet, clinopyroxene and HT amphibole (compare with figures 8d,g). b-c) Close-up views showing some amoebial garnet crystals intergrown with clinopyroxene and amphibole. Complex Grt-Cpx-omenite intergrowths are observed on garnet edges (see text and Dubacq et al., 2019). Note the extensive fracturing of all minerals, mostly perpendicular to the schistosity. d) Garnet with inclusion-rich core from a cm-scale

metapelitic horizon in HTa. Inclusions comprise ilmenite (Ilm), sillimanite (Sil) and nanogranites (inset). e) Sequence of fluid infiltration events at the mantle base of the New Caledonia ophiolite. Former mafic dikes are fluxed by aqueous, metamorphic sole derived fluids, first Ca-Al- then K-Ba-rich (compare with Fig. 12a). See Soret et al. (2016) for details.

Fig. 14 Deformation, fluid flow and coupling of the plate interface during subduction infancy, across scales. a-c) Representative textural evolution of banded peridotites and metamorphic soles, at similar temperatures, accompanying strain localization during early subduction (M: mylonite; PM: protomylonite; UM: ultramylonite). From left to right, increasing deformation and progressive cooling across the ~900-650°C range can be compared with figures 8 through 11; same colors, approximately, as for EBSD maps).

d) Reconstruction of mineralogical transformations, deformation mechanisms and fluid transfer during the major steps of subduction infancy, including down-stepping of the plate interface into the slab (i.e., successive accretion of metamorphic sole HTa, HTb and LT; see Figs. 5b, 6). Note the extreme thinning of HTa and adjacent peridotites during their joint early exhumation, predating or coincident with accretion of HTb. Complementary observations (e.g., Fig. 13a-c) suggest that transformations opposite to those documented for the retrogression of the HTa sole \ peridotite pair (i.e. fluid ingress, dissolution-precipitation processes, retrograde reactions, grain size reduction; thick, right-directed arrow in d) take place during the prograde evolution, when amphibolites reach conditions of HTb and transform into peak HTa. The increase in temperature (left-directed arrow) favors the crystallization of strong and dry minerals (garnet, clinopyroxene), grain coarsening, shortage of fluids, and therefore a large decrease in the efficiency or disappearance of dissolution-precipitation creep (DPC) on both sides of the interface. The slab crust transforms at 900-850°C into a dominantly dry Grt-Cpx-bearing granulite with similar effective viscosity to the dry porphyroclastic tectonite of the mantle, so that the plates become fully coupled. Along with the temperature increase, deformation mechanisms evolve from dominant fluid-mediated, grain-size sensitive, dissolution-precipitation creep to dislocation creep (DC).

Fig. 15 Evolution and driving mechanism of deep coupling of the subduction interface. a) Idealized view of mature subduction (modified after Audet and Burgmann, 2014 and Agard et al., 2018; see also Fig. 1c) emphasizing the role of deep coupling on the thermal structure and dynamics of the subduction wedge, and therefore on heat fluxes (above the 'cold corner'), mantle viscosity (e.g., post-seismic rebound) and mantle dynamics (as imaged by SKS patterns). b) In the coupling zone, plates become coupled over some distance along dip (grey curves, thick or dashed); deformation becomes distributed and the notion of plate interface disappears (i.e. only remains as a chemical contrast between the slab crust and the mantle) as velocities of the upper and lower plate become similar (arrows). Indicative

evolution of mantle wedge and slab crust mineralogy: assemblages turn to essentially dry minerals in a fluid-starved environment. Same abbreviations as in text except Atg: antigorite; Ol^d: dry olivine; Ol^w: wet olivine. c) Close-up view on processes inferred to cause deep viscous coupling (marked decrease in DPC; breakdown of hydrous phases to a large extent; grain size coarsening) and progressive strain delocalization. Compare with figure 5b and see text for details (§ 4.2). Plate interface thickness, i.e. across which deformation is distributed, evolves along dip from cm- to km-scale. The local, restricted melting (in peak HTa; see 3.1.1) further enhances reduction of DPC and grain growth. Melts and mélange diapirs, if any (see Behn et al., 2011; Marschall and Schumacher, 2012; Bayet et al., 2018) must form below the coupling zone.

Fig. 16 a) Deepening of the coupling zone, from early to mature subduction, expressed as a function of the cooling subduction zone thermal gradient. Constraints on this evolution are given by the fossil rock record, i.e. successively soles, HT and LT eclogites (see § 4.2 and panel b). The approximate duration of the transition from early to mature subduction, until reaching full strain localization along the plate interface and stabilizing the coupling zone at ~80-100 km depth, is indicated in red (~5-10 Ma). Time constraints partly come from recent age constraints on the Semail example (see discussion in § 4.3).

b) Diagram showing the natural P-T conditions sampled by metamorphic rocks recovered from fossil subduction zones (blue area) and the evolution of subduction geotherms (from the compilation of Agard et al., 2018). The thermal regimes of the Japan and Cascadia subduction zones are indicated for comparison. Major transitions for the oceanic crust are shown in blue (amphibole out and wet solidus) and red (when melts become >~5 wt%). Major reactions for the mantle are shown in green (Amp: amphibole; Atg: antigorite; Chl: chlorite). The fossil metamorphic record constrains possible depths of coupling: these samples were exhumed so escaped full coupling, which must be somewhat deeper. This fossil record is compared to the T-depth range across which mafic slab crust is predicted to dehydrate for cold, intermediate or warm subduction geotherms (white dots labelled c, i, w, respectively; Hernandez-Uribe and Palin, 2019). The good match between these estimates and the envelope supports the idea that fluid availability has a key role on coupling. Besides, no single reaction can explain the location (and evolution) of the coupling 'depth' in P-T space, pointing to a more general mechanism such as the reduction of DPC (see Fig. 15c).

Fig. 17 Slabification, from subduction nucleation to stable subduction. This tectonic scenario relies on observations from sole/peridotite pairs across the world, and uses observations from subduction initiation across the Izu-Bonin/Marianas forearc (e.g., Stern et al., 2012 and references in text). This model emphasizes the links between early slab dynamics, the onset and progressive migration of deep viscous coupling with time as the

subduction zone cools, and the onset of mantle upwelling (which may result in forearc lithosphere and supra-subduction ophiolite formation). General dynamics should be considered more robust than timescales, which heavily rely on time constraints from the Semail and Izu-Bonin examples (indications in orange and blue, respectively in this figure). Intraoceanic subduction initiation, whose dead-end can be ophiolite emplacement (e.g., for Tethyan ophiolites), appears to be a rather sluggish process, on the order of 10 Ma at least. See § 4.3 for more details.

(a) Subduction nucleates on some geological heterogeneity (underlined here by a contrast in lithosphere thickness/age, such as a long a transform fault) after regional-scale plate reorganization (at 110 ± 5 Ma for the Semail example).

(b) Beyond serpentinite stability (600°C dotted line), the gradual onset of mechanical coupling and resistance to slab penetration make subduction infancy sluggish. For Semail, prograde garnet growth in HTa occurs at 104-103 Ma, and this early stage ends with peak burial and accretion of HTa to the peridotites, probably before 97-93 Ma.

(c) Once progressive unlocking of mechanical coupling happens, the slab starts progressing down, the locus of viscous coupling migrates downwards and slab penetration initiates local mantle upwelling. Melting of undepleted upwelling dry asthenosphere, and then of depleted but fluid-fluxed asthenosphere may give birth to the short-lived succession of MORB-type forearc basalts (FAB) then boninite products, as observed in Izu-Bonin ($\sim 51 \pm 1$ Ma) and in the Semail ophiolite (96 ± 0.5 Ma). Ophiolite formation impinges on older lithosphere (NT for Neotethyan examples), either not preserved or limited to unrecognizable mantle fragments (e.g., to the SW of the Semail ophiolite). This stage coincides with the early exhumation and thinning of HTa metamorphic soles and adjacent peridotites, through buoyancy and/or shearing by the base of the upwelling dry mantle. This stage also corresponds to the accretion of the HTb sole.

(d) Slab stabilization ends with stabilization of deep viscous coupling near 80-100 km depth in a mature (and cold) subduction zone. Slab pull is then fully coupled to mantle convection, early asthenospheric upwelling is reversed to mature mantle counterflow (contrary to stage c), and the subduction zone has been extensively decoupled and refrigerated, leading to the formation of LT eclogites (or HT eclogites in a mature warm subduction zone). The last metamorphic sole accreted before final lubrication is the metasedimentary LT sole. During this period, when viscous coupling reaches depths >50 - 60 km, P-T conditions along the subduction interface are those of HT eclogites (or high-grade blueschists) occasionally exhumed as mafic blocks embedded in serpentinitized mantle (Agard et al., 2018).

(e) From stage d onwards, subduction is mature/steady, with stable viscous coupling, continuous formation of LT eclogites (rarely exhumed; see figure 16b), and melting of the hydrated mantle wedge at sub-arc depths marked by calc-alkaline magmatism.

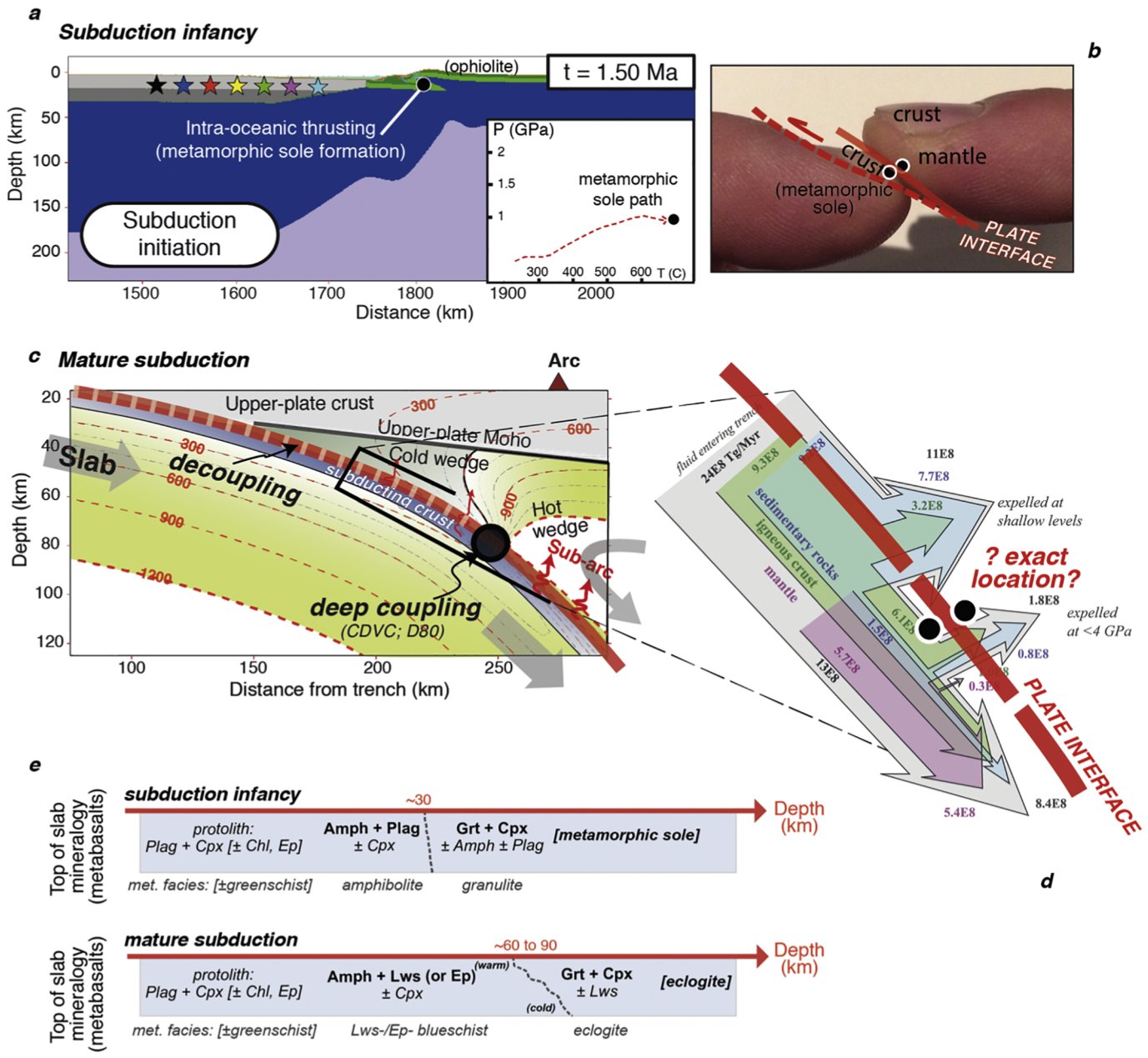


Figure 1

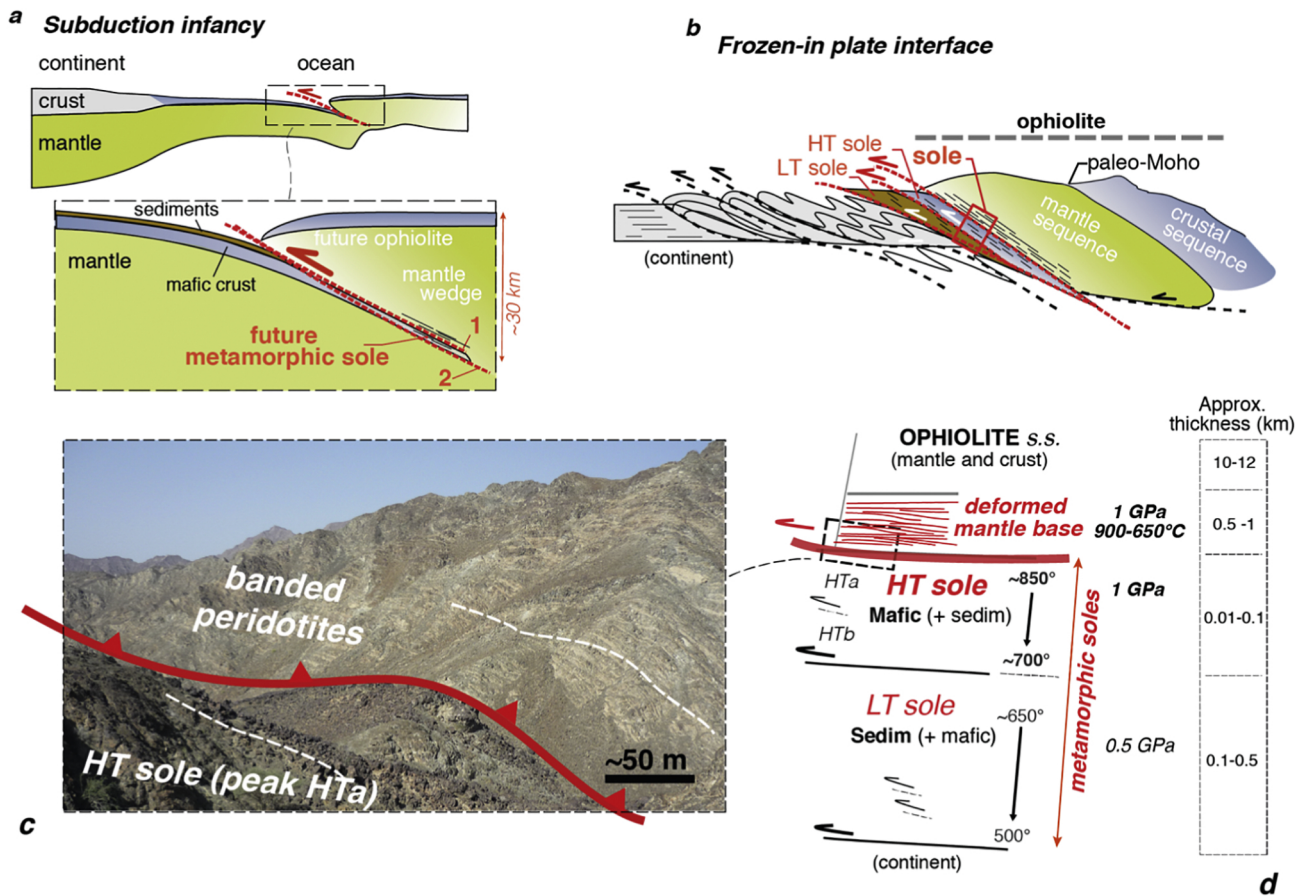


Figure 2

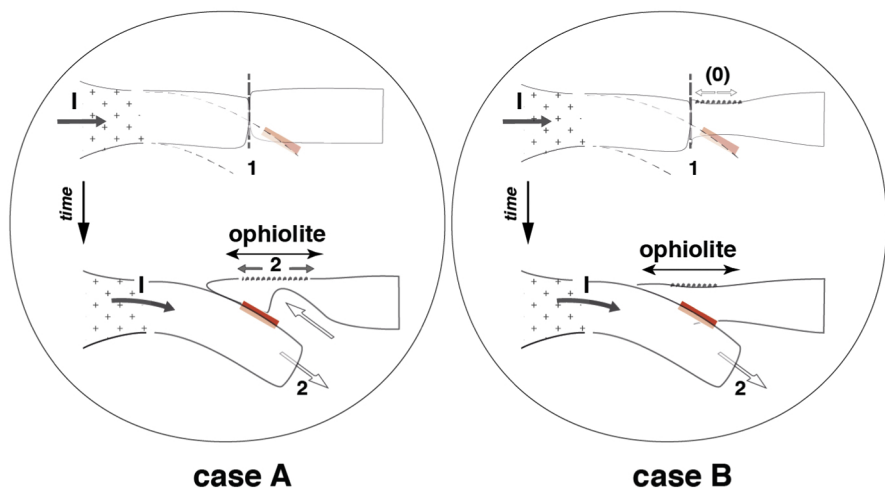
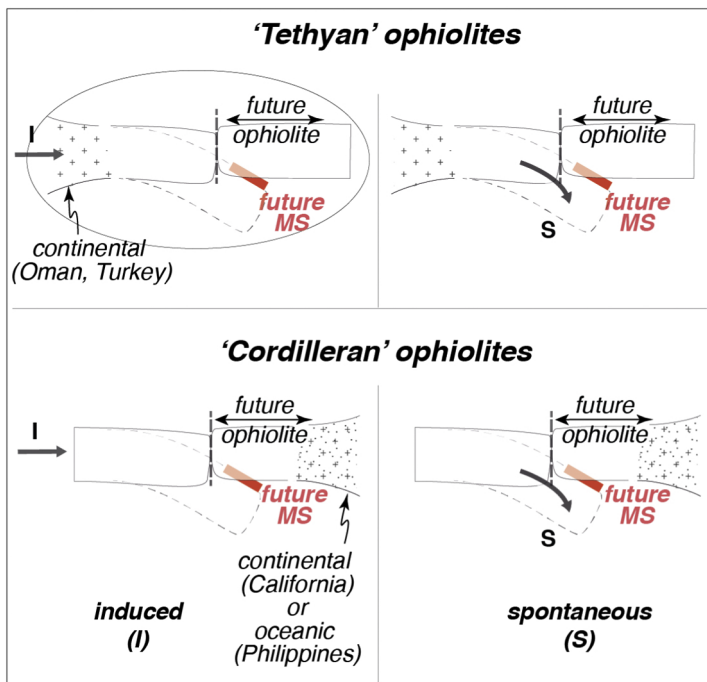
a

Figure 3

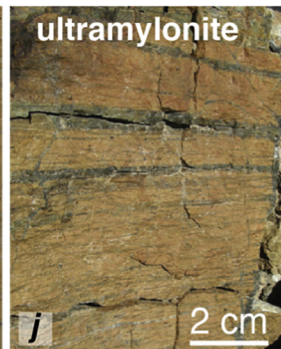
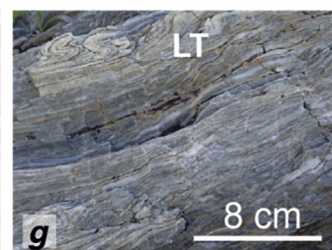
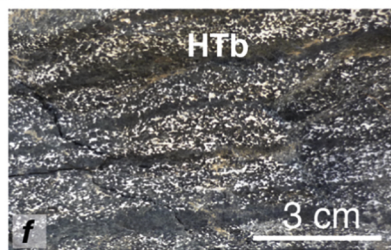
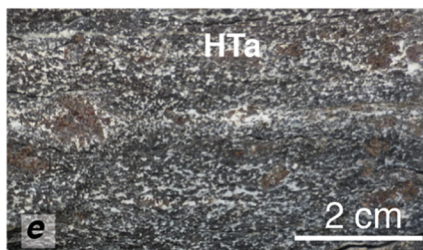
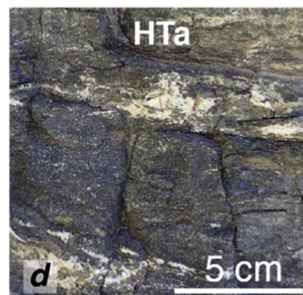
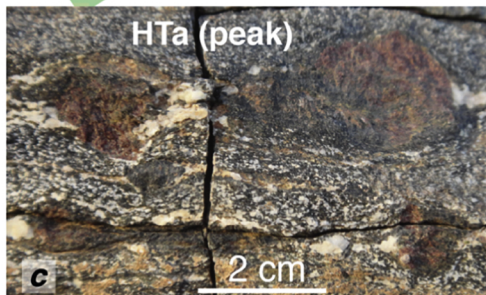
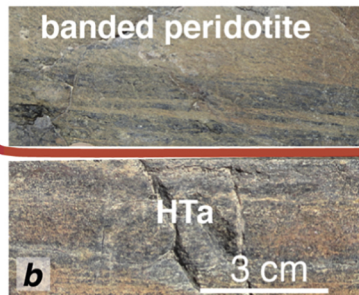
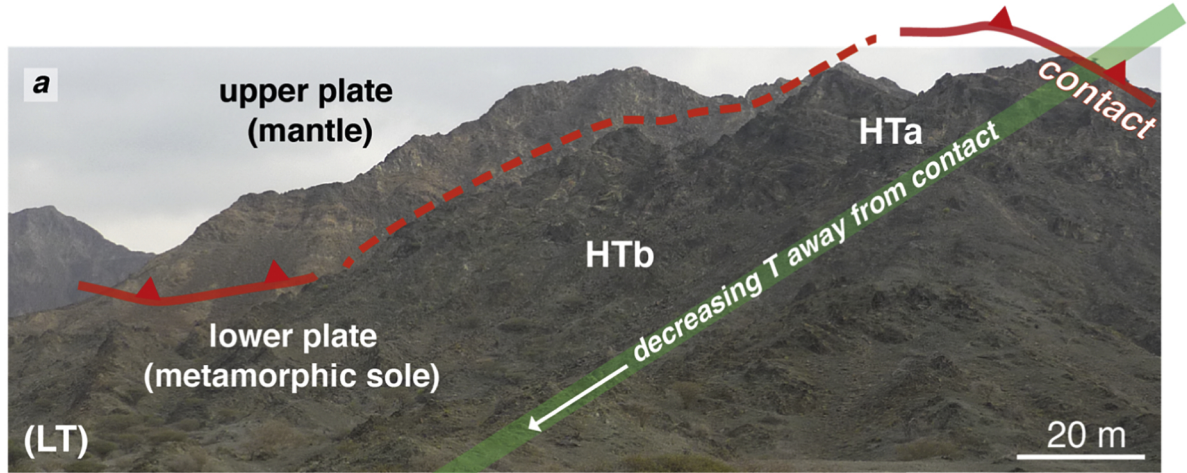


Figure 4

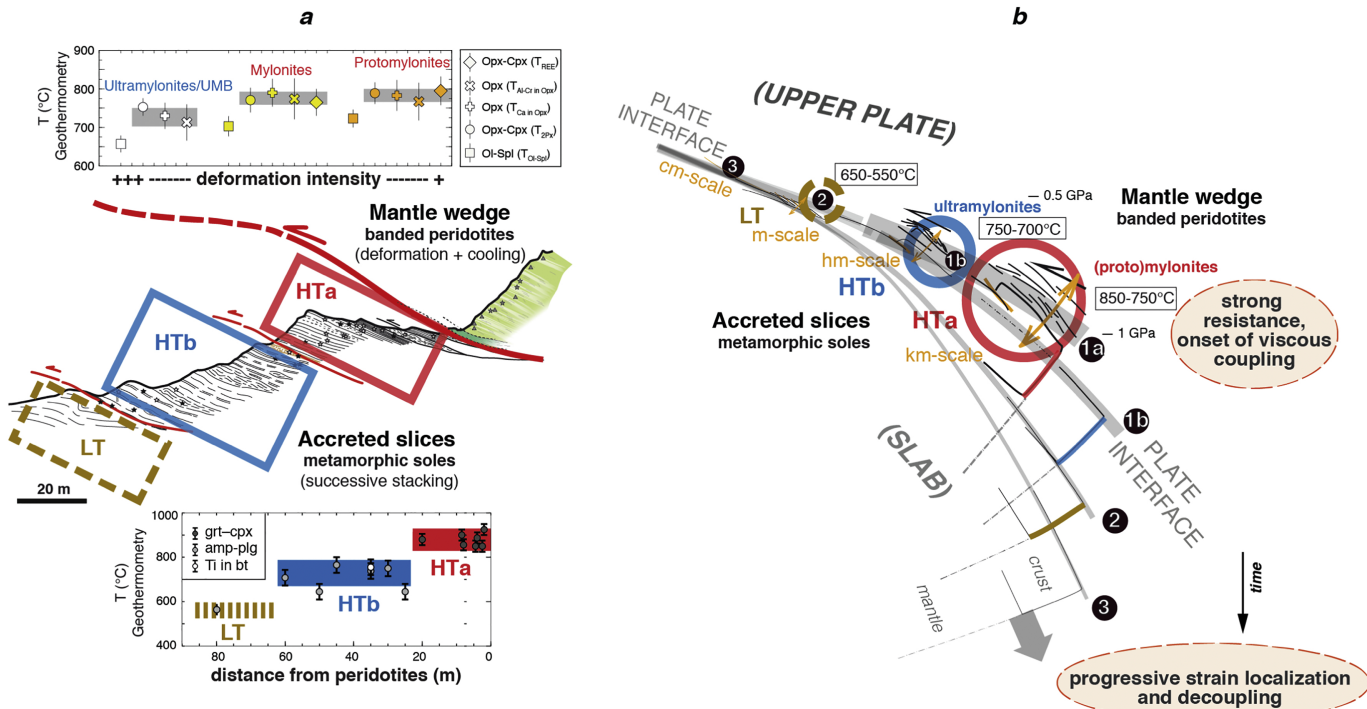


Figure 5

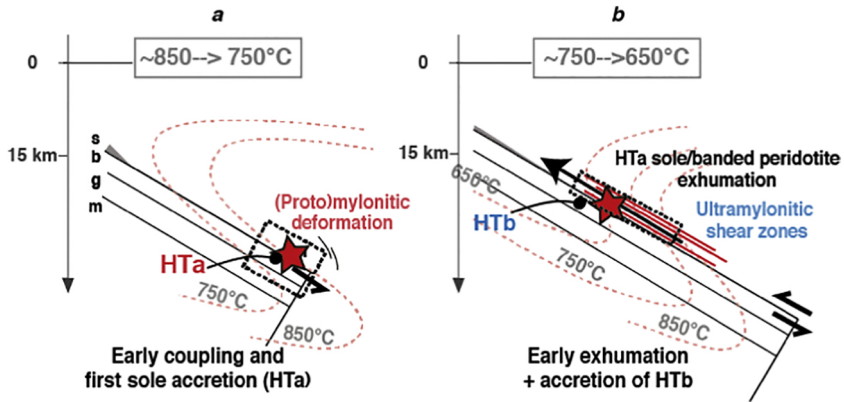
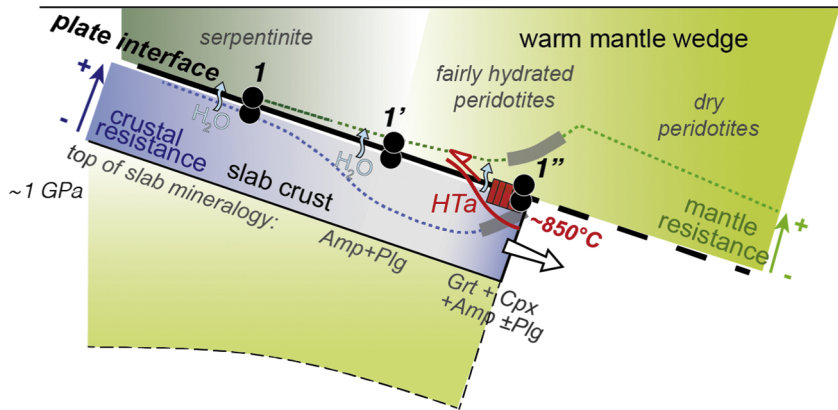


Figure 6

a Onset of viscous coupling (accretion of HTa)



b Effective viscosity

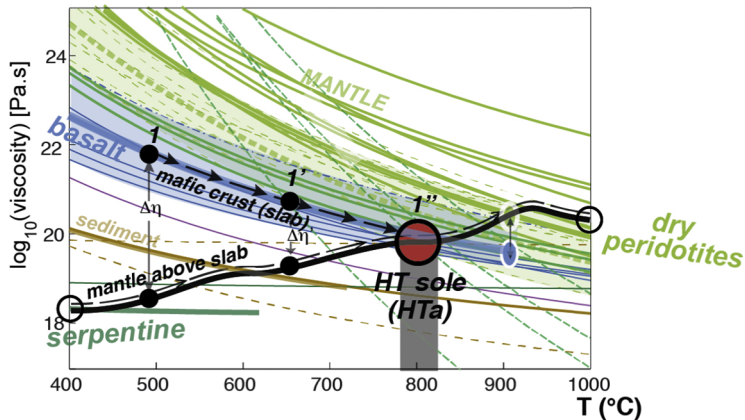


Figure 7

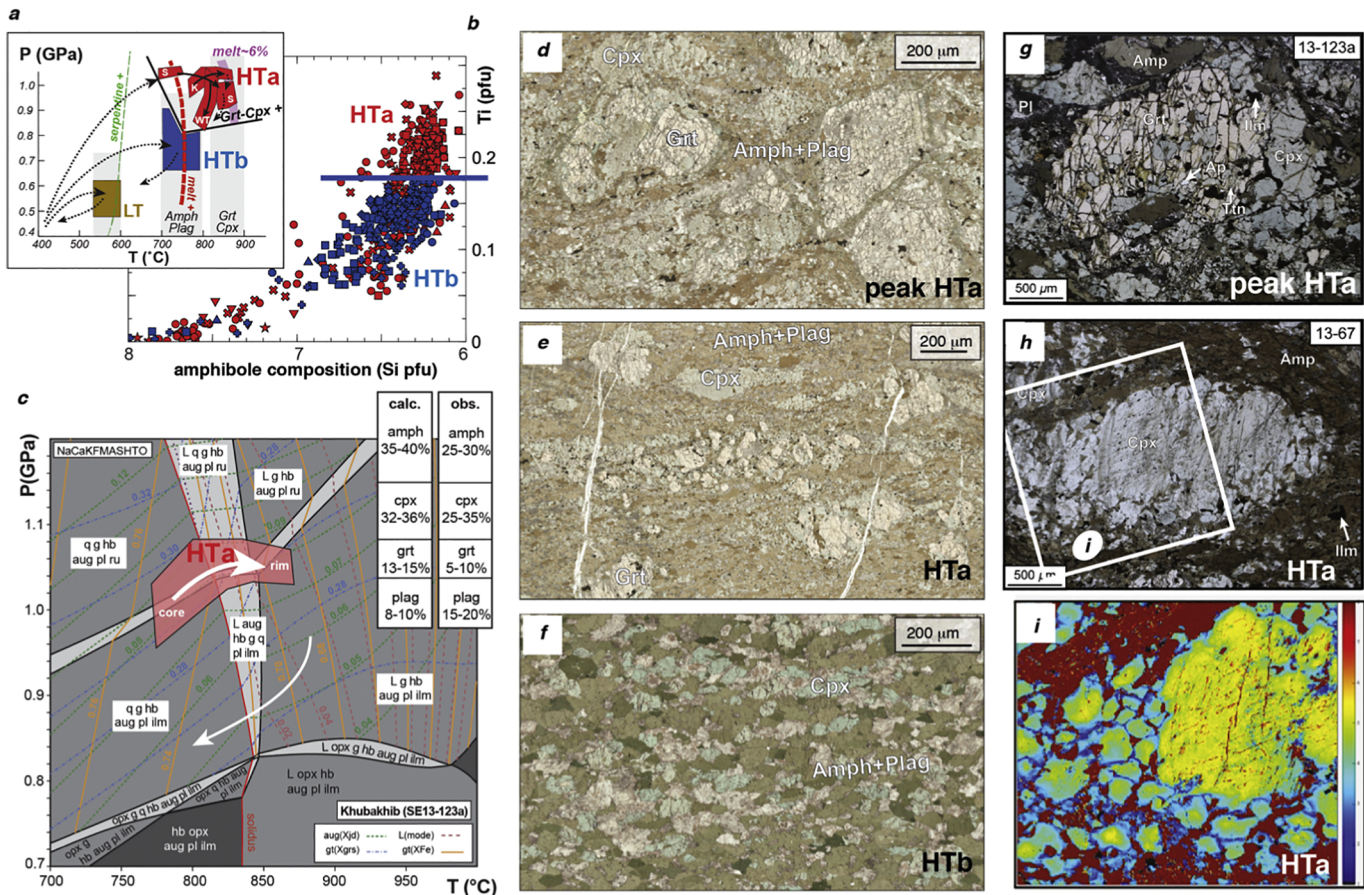


Figure 8

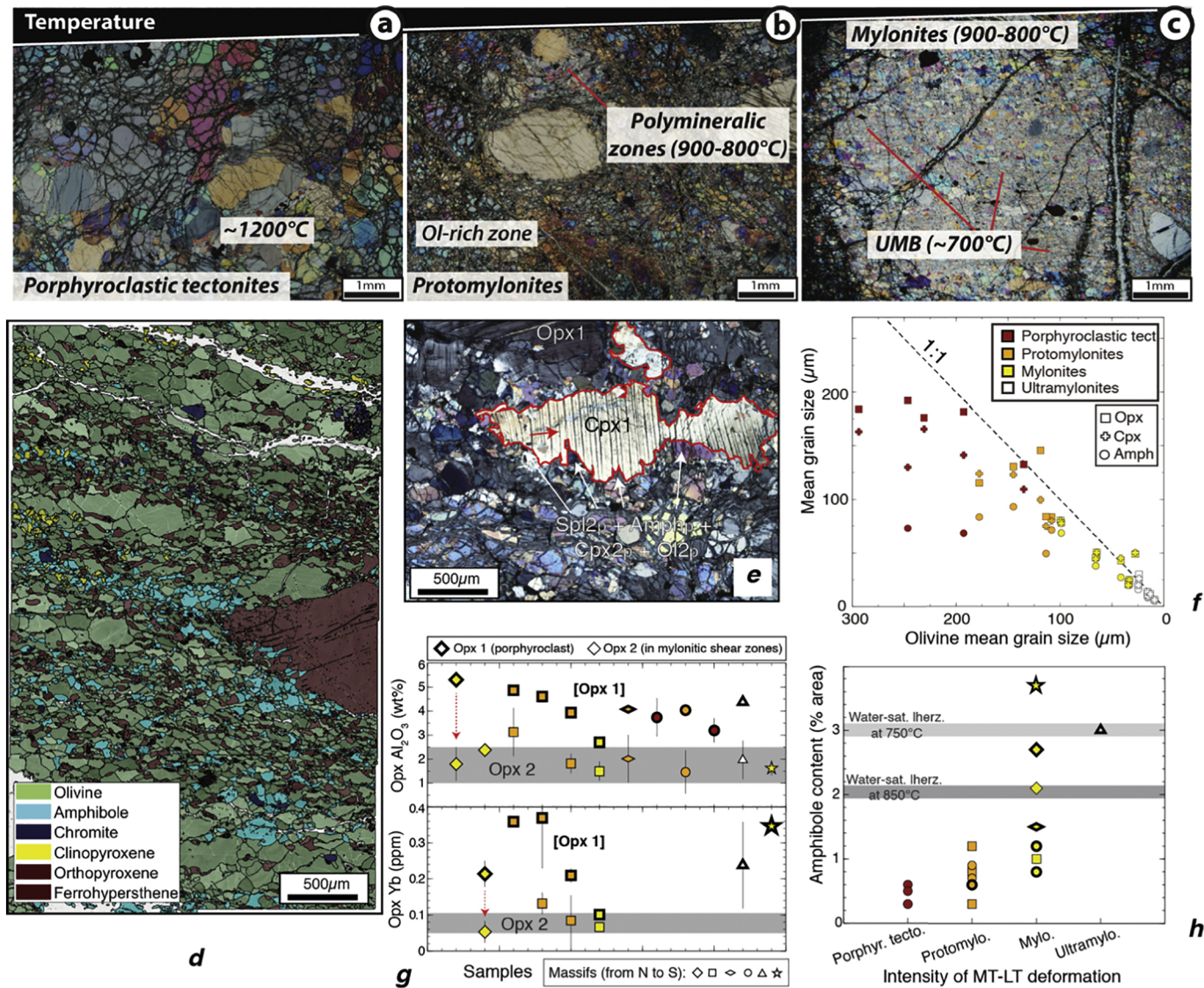


Figure 9

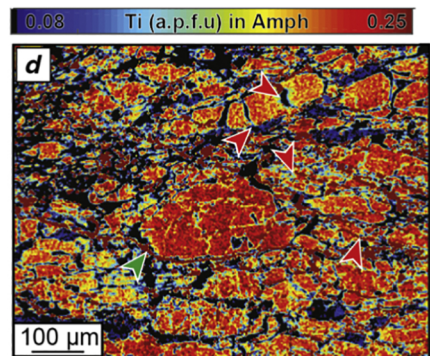
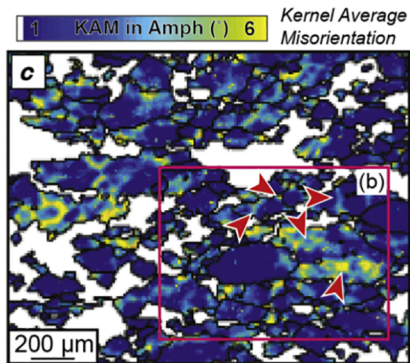
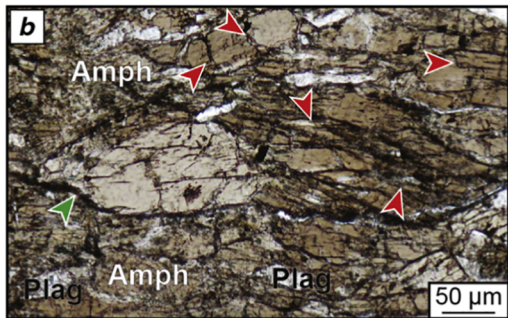
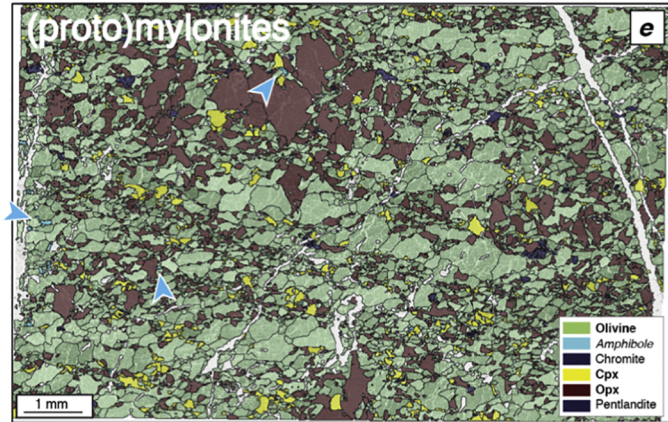
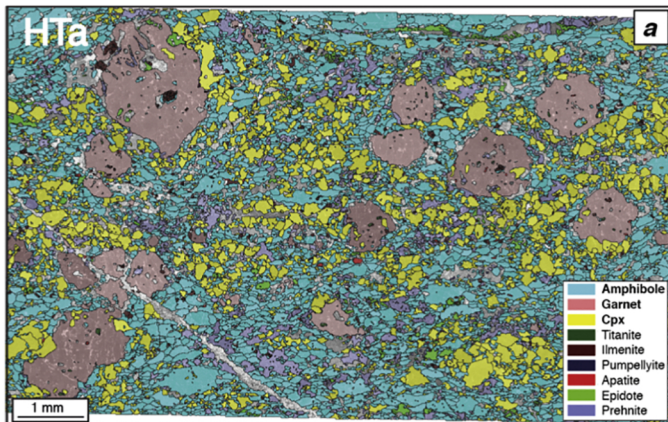


Figure 10

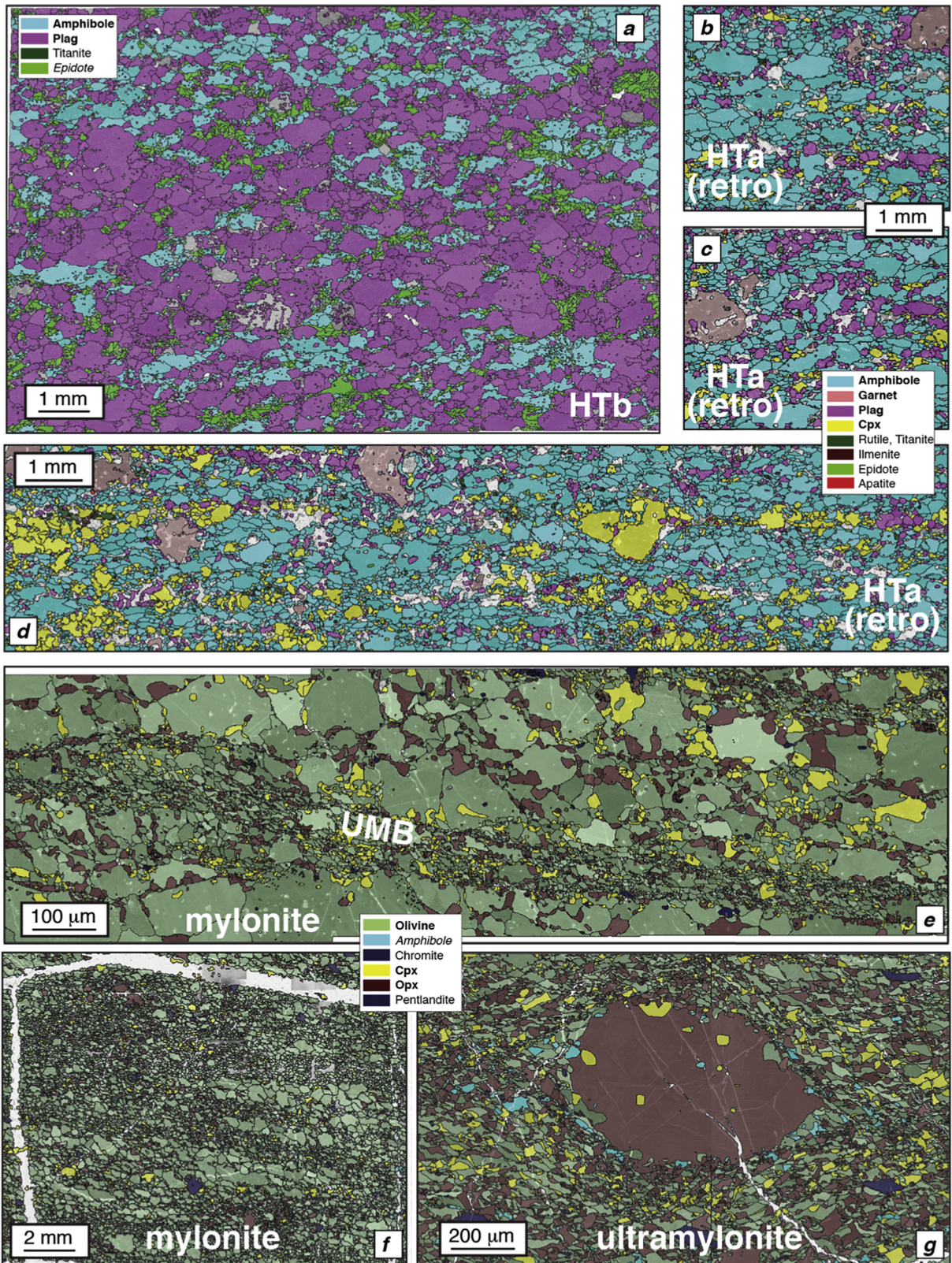


Figure 11

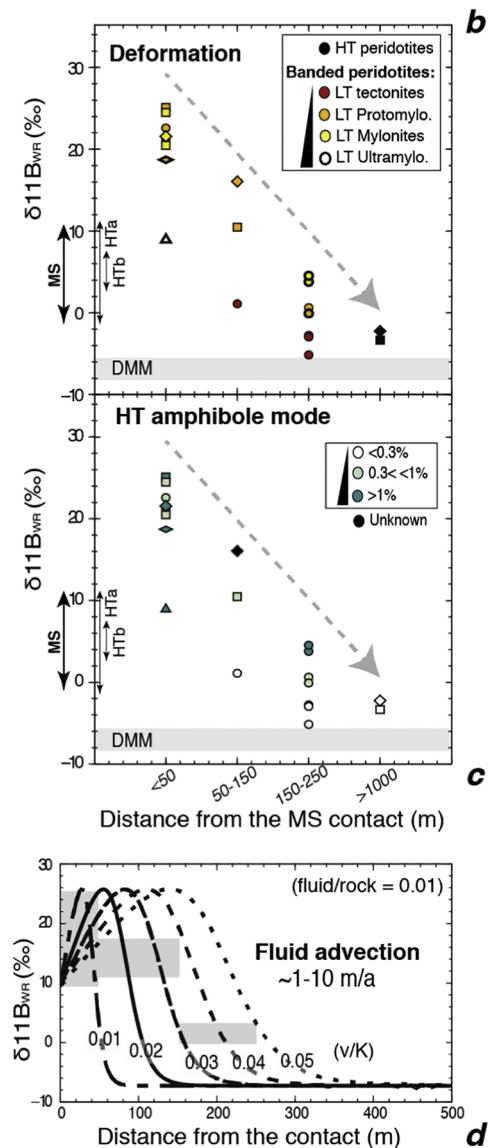
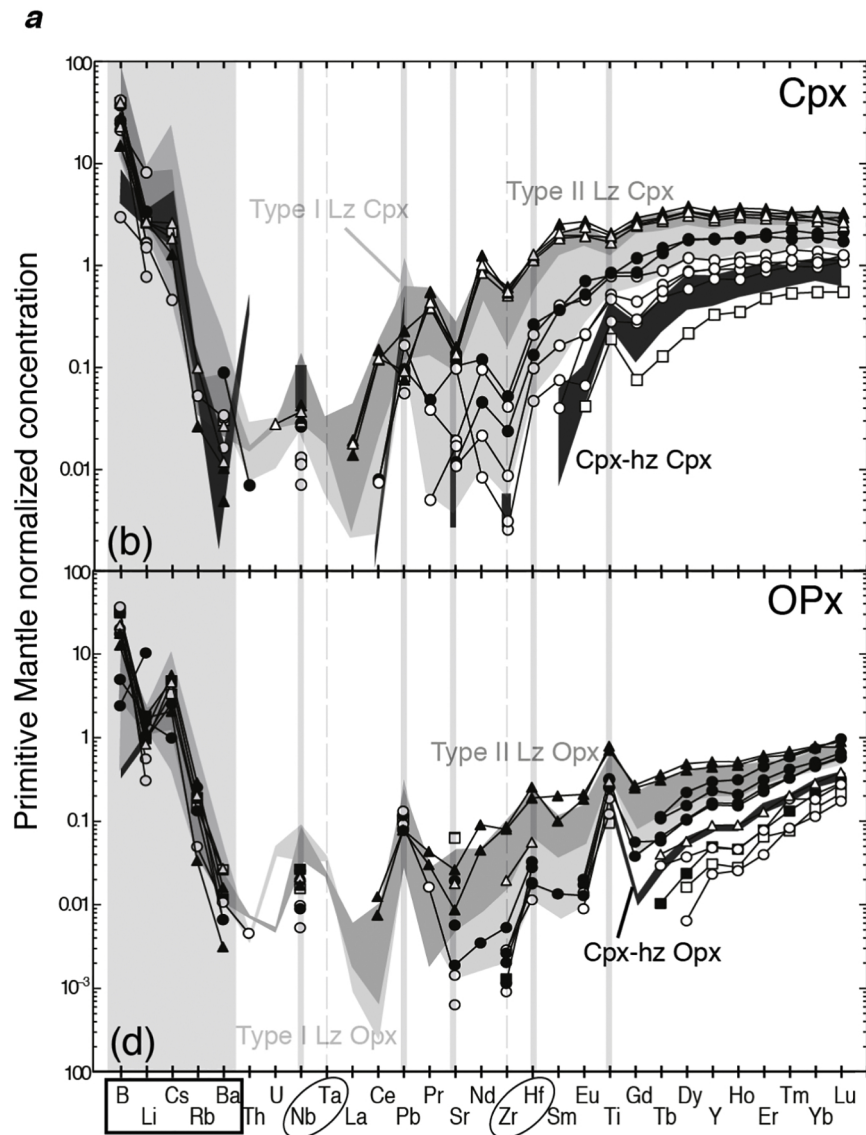


Figure 12

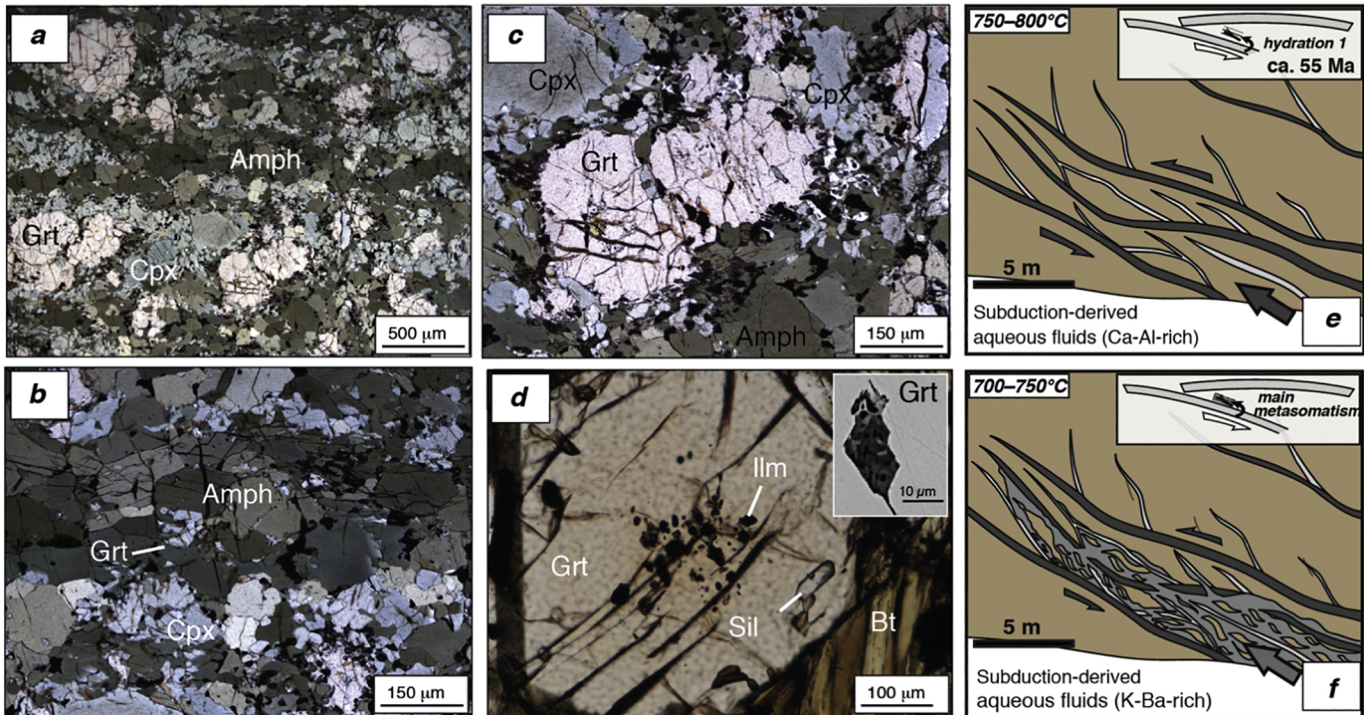
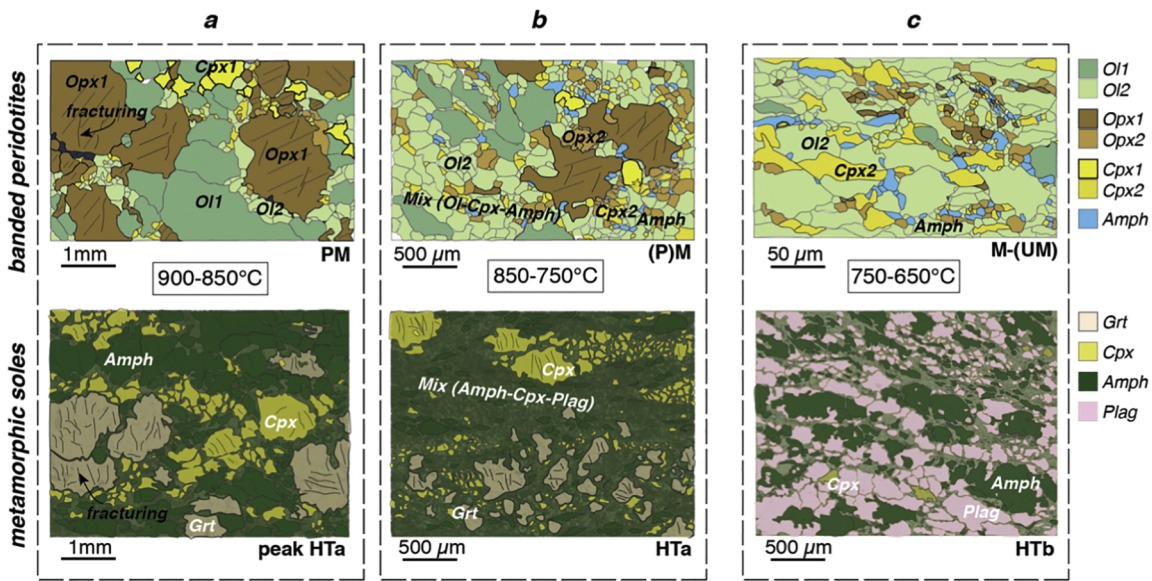


Figure 13



Time evolution during subduction infancy (at ~constant depth)

Progressive strain localization by fracturing, fluid ingression, DPC, grain size reduction, phase mixing...

Time evolution during subduction infancy (at ~constant depth)

Progressive strain localization and decoupling

Towards viscous coupling: Depth evolution along the interface, for infant and mature subduction zones

Progressive strain distribution and viscous coupling

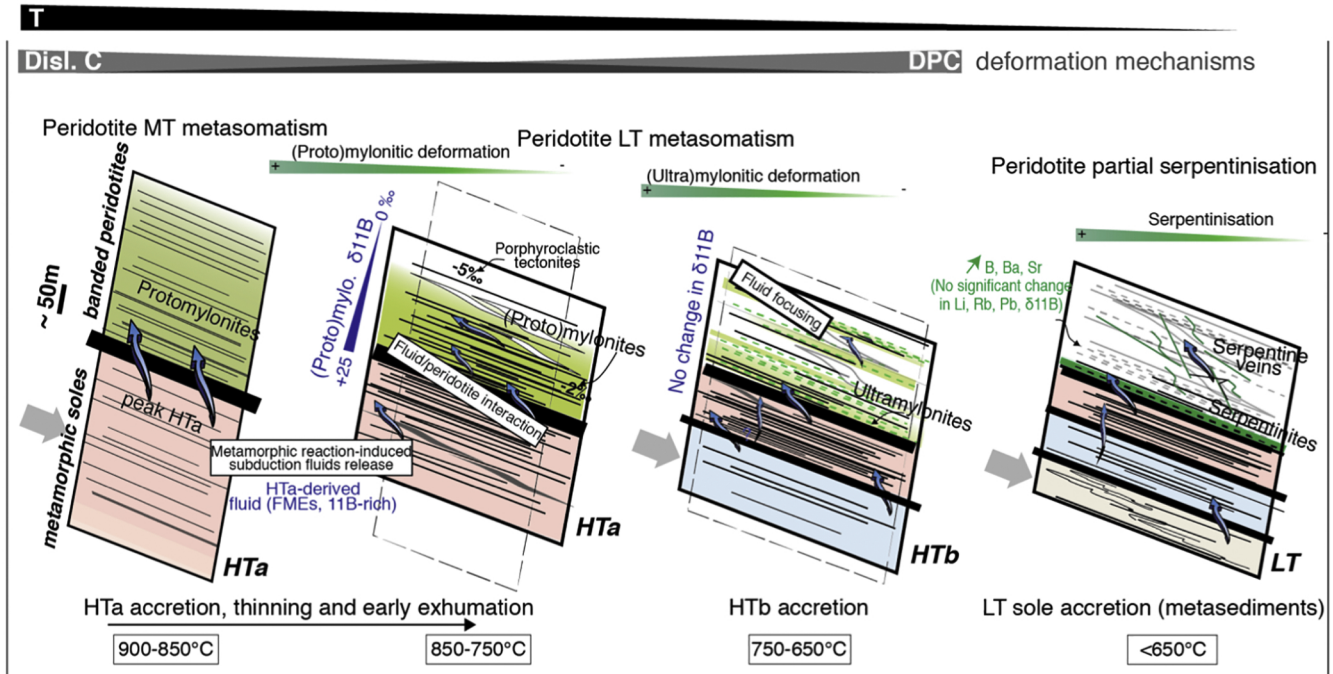
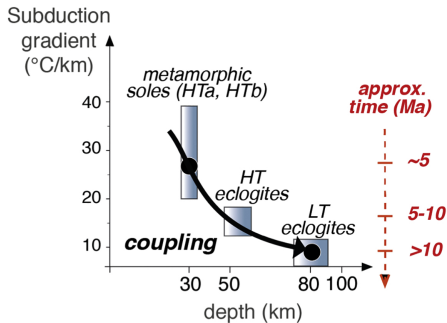
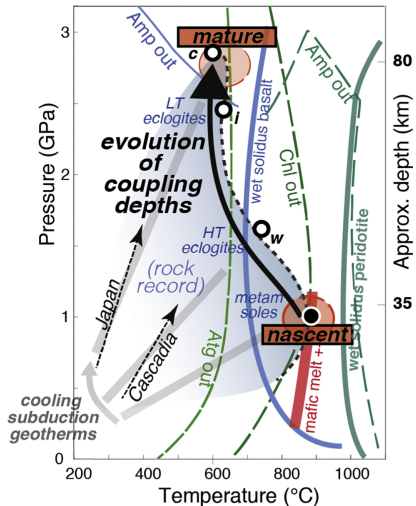


Figure 14



a



b

Figure 16

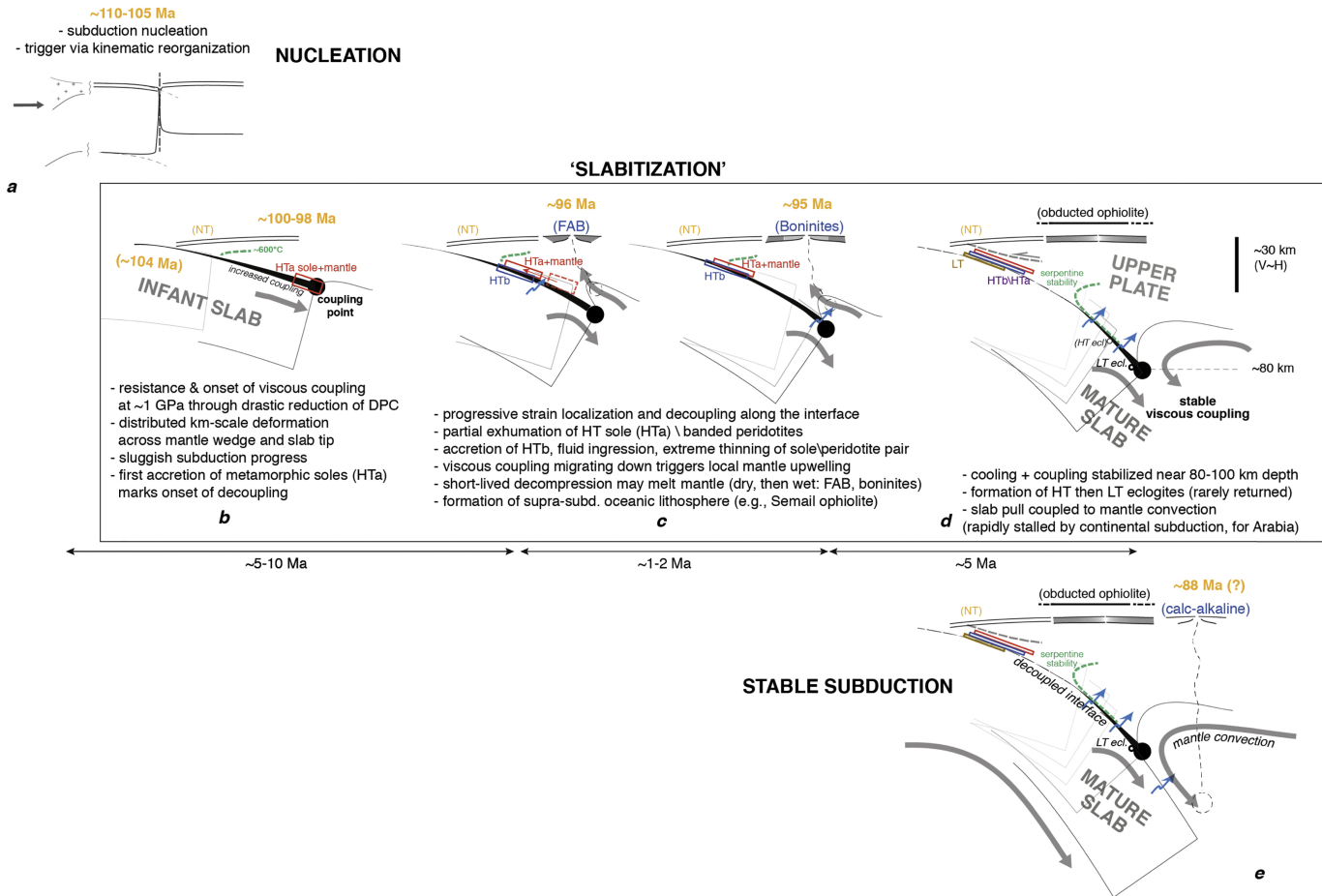


Figure 17